LATERAL-TORSIONAL STABILITY FOR CURVED 6061-T6 STRUCTURAL ALUMINIUM ALLOYS

A dissertation submitted in fulfilment of the requirements

by

E-P T Tebo

Student No: 212059475

for the degree

Master of Engineering in Mechanical Engineering

in the

Faculty of Engineering & Technology

Vaal University of Technology

Supervisor: Prof LM Masu

Co-supervisor: Dr PK Nziu

Date: 02/12/2020

Abstract

Though aluminium (Al) is justifiably described as a green metal with an increasing rate of application in structures, designers still restrain themselves from its applications as a load-bearing skeleton in structure due to insufficient design guidelines. This insufficient information is more with channel sections that might experience lateral-torsional buckling (LTB) when used as a load-bearing skeleton in structures. This study investigates the effects on imperfections on LTB load-carrying stability for 6061-T6 Al alloy channel section arches and proposed design guidelines. The case study focused on freestanding circular fixed end arches subjected to a transverse point load at the shear centre.

The software package Abaqus was used to study a total of 110 arch models from three separate channel sections with an additional 16 arch models for validation. Sixty-six channel arches were developed at a constant length, while the remaining 44 arches were formed at constant slender ratios using 11 discrete included angles. The FE analyses methods used for the investigation were validated with existing analytical methods and showed good agreement, despite the assumptions of the bilinear curve used for material nonlinearity, initial geometric imperfections and residual stresses that presented the imperfections of the models. The different investigated factors include slender ratios, change in cross-section area, imperfections, and angles. These factors were found to have substantial impacts on the prebuckling state, which turns to impact LTB behaviour and load-carrying capacity.

From arches developed at constant span length, the arches with moderately included angles ($50° \leq 2\alpha \leq 90°$) were found suitable for the designs against LTB, followed by the shallow ($2\alpha < 50°$) and deep arches ($90° < 2\alpha \leq 180°$) respectively. For arches developed at constant slender ratios, the deep arches were found to be more suitable in the design against LTB, followed by the moderate and shallow arches, respectively. In addition, it was realised that the change in web-flange thickness, section depth and slender ratios, had significant effects on the LTB loads magnitudes and very insignificant effects on the general behaviour across the included angles. The same occurrence was also observed on the prebuckling analyses.

All the investigated channel section arches showed the imperfections to have significant impacts on the LTB loads. Arches developed at constant span length showed the maximum elastic LTB loads to have overestimated the expected real LTB loads by approximately 48 percent. While the maximum elastic LTB loads of arches developed at $S/r_x = 60$ and 90 showed that the real LTB loads were overestimated by about 39 and 14 percent, respectively. That said, the elastic LTB loads on average overestimated the real LTB loads by over 50 percent for the arches developed at the constant span length and by only 18 percent for arches developed at the constant slender ratios.

Declaration of dissertation

I Mr. Emmanuel-Peters Teke Tebo, declare that this dissertation is my original work and that it has not been presented to any other university or institution for similar or any other degree award.

……………………… 02/12/2020

Signature Date

Publications

The following published articles were extracted from this dissertation:

Articles that have been published

1. Tebo, E-PT., Masu, L. & Nziu, P. (2020). Effects of factors that influence out-of-plane lateral-torsional buckling on freestanding circular arches. *Journal of Engineering, 2020*.
2. Tebo, E-P.T., Masu, L. & Nziu, P. (2020). Comparison between elastic and inelastic lateral torsional buckling load on circular fixed channel section arches under transverse point load. *International Journal of Engineering Research and Technology,* 13, 9 (2020), pp. 2239-2254
3. Tebo, E-P.T., Masu, L. & Nziu, P. (2020). Inelastic lateral-torsional buckling load on fixed circular channels arches under transverse point load. *International Journal of Engineering Research and Technology,* 13, 10 (2020), pp. 2851-2863
4. Tebo, E-P.T., Masu, L. & Nziu, P. (2020). Inelastic lateral-torsional buckling load on fixed circular channels arches under transverse point load. *International Journal of Engineering Research and Technology,* 13, 10 (2020), pp. 2870-2883

Acknowledgements

Not only is it the gift of life that has made it possible for me to achieve this level in my academics, but also due to the relentless effort of some fantastic people for which I am glad to acknowledge. Glory to God Almighty for giving me the strength, wisdom and good health throughout this research.

First, I would like to thank my family for supporting me this far in my academic path by their constant encouragement. For this, I am also thankful to Mr. Gordon Nwanjang Tebo and Dr Zodwa Mbambo for their spiritual and financial help.

Next, I wish to express my sincere appreciation to my supervisor, Prof. Leonard Masu and co-supervisor, Dr Patrick Nziu, who has the substance of a genius. They convincingly guided and encouraged me to be professional and do the right thing even when the road got tough. Without their persistent help, the goal of this project would not have been realised.

I am indebted to the Vaal University of Technology, Vanderbijlpark, South Africa and the Faculty of Engineering and Technology, for I am truly fortunate to be one of your graduates. Thank you for the knowledge you have shared without any form of disfavour. For that I am genuinely grateful.

I wish to express my deepest gratitude to the National Research Foundation (NRF) through the Vaal University of Technology. Without your support and funding, this project could not have reached its end goal.

To conclude, I am ever grateful for the life of my father, Mr Tebo Shadrad (R.I.P) and my mother, Mrs Tebo Elizabeth and everyone around that supported me. May God almighty bless them all.

Dedication

I dedicate this work to my family and friends for their continued love and support.

Table of contents

List of tables

List of figures

Abbreviations and Nomenclature

Abbreviations

Al	Aluminium
BS EN	British Standard European Norm
BSI	British Standard Institute
CAE	Computer-aided engineering
°	Degree
FE	Finite element
FEA	Finite element analysis
FEM	Finite element method
FTB	Flexural-torsional buckling
GMNIA	Geometrical material non-linear imperfect analysis
GMNIA-1	Geometrical material non-linear imperfection at e_0
K	Kilo
LTB	Lateral-torsional buckling
LBA	Linear buckling analysis
LEA	Linear elastic analysis
MNA	Material non-linear analysis
Max	Maximum
GMNIA-1 Max	Maximum geometrical material non-linear imperfection at e_0
GMNIA-Max	Maximum geometrical material non-linear imperfection at e
m	Meter
mm	Millimetre
N	Newtons
N/A	Non-applicable
sec	Seconds
3D	Three dimensional

Subscripts

cr	Critical
imp	Imperfection
pl	plastic
ult	Ultimate

Nomenclature

C_y	$[mm]$	Position of the centre of gravity
F_{cr}	$[N]$	Maximum elastic buckling / critical load
F_{ult}	$[N]$	Ultimate buckling load
I_x	$[mm^4]$	Major moment of inertia
I_y	$[mm^4]$	Minor moment of inertia
M_C	$[N.mm]$	Elastic bending moment at the crown
M_d	$[N.mm]$	Elastic bending moment at the support
M_M	$[N.mm]$	Bending moment
M_P	$[N.mm]$	Plastic moment of the cross-section
M_m	$[N.mm]$	Inelastic bending moment at the crown
M_D	$[N.mm]$	Inelastic bending moment at the support
N_C	$[N]$	Elastic axial compressive force at the crown
N_Y	$[N]$	Squash/crash load
N_m	$[N]$	Inelastic axial compressive force at the crown
Z_M	$[mm^3]$	Plastic section modulus
e_0	$[mm]$	Imperfection bow from European design code EN BS, (2011) for steel
e_1	$[mm]$	Position of the shear centre
f_{ult}	$[MPa]$	Ultimate tensile strength
f_y	$[MPa]$	Tensile yield strength
r_x	$[mm]$	Radius of gyration about the major axis
t_f	$[mm]$	Flange thickness
t_w	$[mm]$	Web thickness
u_{imp}, v_{imp}	$[mm]$	Lateral and radial imperfections respectively
w_{imp}	$[degree]$	Twist imperfection
y_p	$[mm]$	Point of transverse applied load from the shear centre
N_N	$[N]$	Axial compressive force

α_R	$[MPa]$	Residual stress
α_y	$[MPa]$	Yield stress
β_{cr}	[ ]	Critical load coefficient / elastic critical resistance of the
β_{pl}	[ ]	In-plane plastic load coefficients/plastic resistance of
β_{ult}	[ ]	Ultimate load coefficient / ultimate resistance of the arch
λ_x	[ ]	Slenderness of the arch
2α	$[degree]$	Included angle
h	$[mm]$	Height of the arch at the twist
A	$[mm^2]$	Area of the cross-section
b	$[mm]$	Width of the section
d	$[mm]$	Depth of the section
E	$[GPa]$	Young's modulus of elasticity
F	$[N]$	Applied transverse point load
G	$[GPa]$	Shear modulus of elasticity
H	$[N]$	Horizontal reaction at the support
$H(\theta)$	[ ]	Step function
L	$[mm]$	Span length
R	$[mm]$	Mean radius
S	$[mm]$	Arc length
X, Y, Z, x, y, z	[ ]	Global and local coordinate systems
e	$[mm]$	Maximum initial imperfection from Spoorenberg, (2011)
k	[ ]	Initial bow imperfection coefficient for second-order analysis for LTB (BSI, 2007)
r	$[mm]$	Inner radius of the web and flange
v	$[mm]$	Out-of-plane deflection at ultimate load
Θ	$[degree]$	Half included angle
β	[ ]	Load proportionality factor/load multiplier
θ	$[degree]$	Angular coordinate / position
ϕ	$[degree]$	Variable angle

Chapter 1: Introduction

1.1 Background of study

Aluminium metal (Al) is known as the most abundant metal on earth (Davis 2001). The metal is said to be the next most used structural metal after steel. It has a growing rate of application in the refurbishment and construction of new buildings, bridges, seismic protection and building of large-span roof systems (Poinern, Ali & Fawcett 2010b; Dokšanović, Džeba & Markulak 2017).

Similar to steel, Al alloys have recommended areas of application. Alloy 6061-T6, belonging to the 6-series of Al alloys generally denoted as 6xxx, is used widely as a load-bearing skeleton in structures (Hulamin Extrusions 2016:25). This application in structures is influenced by the alloys' high yield strength, which can be boosted during the solution heat-treatment process. Thus, the T6 represents the artificial ageing condition. However, it is advisable to use the alloy in areas with temperatures below 100℃ (Efthymiou, Cöcen & Ermolli 2010). Nonetheless, the alloy's unique valuable properties such as being lightweight, corrosion resistance, having strong durability and being recyclable make it sustainable and justifiably defined as green metal (Efthymiou, Cöcen & Ermolli 2010). Thus, more application of such metals is needed.

There still exists insufficient information when it comes to the application of thin-walled, open sections structural Al alloys as the load-bearing skeleton in structures, most specifically for curved members such as arches. This limitation can be associated with insufficient design guidelines to address common buckling stability problems such as lateral-torsional buckling (LTB), as reported by Mudenda and Zingoni (2018). According to Steel Construction Institute (SCI), in a publication by Brown and King (2001), thin-walled open section members curved in the plane of the web as is typical with arches, turns out to be more unstable by LTB, compared to straight members. The severity of this instability is due to the presence of additional stresses as a result of out-of-plane bending in the flanges caused by direct stress radial components (Steel Construction.org 2010).

The LTB instability is considered a limit-state failure in structures. It is believed, in some design criteria, to be the ultimate limit-state failure typically found in thin-walled, unrestrained members (Wesley 2017:25), in other words, members whose compression flange is free to displace laterally and rotate (Mary Brettle 2006). For this to occur, the compression flange edge has to yield, causing in-plane bending on members' strong axes to change to lateral displacement and twisting (Ozbasaran, Aydin & Dogan 2015; Bajer, Barnat & Pijak 2017).

Freestanding circular thin-walled arch ends are either pinned, out-of-plane fixed, or fixed. In practice, most arches' end supports are to be out-of-plane fixed. The mode of LTB shape for such arch members is considered more complicated than pinned arches (Liu, Lu, Fu & Pi 2017b). This complexity is even more complicated for arches subjected to transverse loading, compared to those under uniform bending or compression. The complexity comes because of axial compressive actions for such arch members. For fixed end arches, this is extra complex due to the combined axial compressive force and bending moment.

Solutions for open thin-walled members subjected to transverse loading are fundamental in structural engineering. However, the general formulation analysis complexity in the designs of open thin-walled arches has instigated designers to refrain from employing such models, despite the aesthetic appeal of arches that today's modern designs and architectures require (Yoo & Pfeiffer 1983; King & Brown 2001). Meanwhile, others have to find recourse in numerical methods such as finite element analysis (FEA) (Liu *et al*. 2017b).

The severity of the LTB stability of arches has led to numerous research studies over the past years. Most of these studies have focused on pinned arches and fixed end arches subjected to uniform compression and bending (Pi & Bradford 2013a; Dou, Guo, Pi, Zhao & Bradford 2014). Several research studies have been conducted for arches subjected to concentrated point loads, as stated by Lu, Liu, Pi, Bradford and Fu (2019) study. Most of these studies used analytical, numerical and experimental methods to analyse freestanding arches. Meanwhile, for arches with fixed end subjected to central concentrated load (CCL), existing research studies, design manuals and standards show evidence of insufficient information, as reported by Liu *et al*. (2017b). In addition, current studies showed that the few studies utilised more of the numerical methods for their solutions, with little reported on the inelastic analysis that incorporates the imperfections (material nonlinearity, initial geometric imperfection and residual stresses), compared to its elastic counterpart.

Furthermore, the studies aimed at addressing LTB instability in arches have focused on open thin-walled double symmetric i-sections (Lu *et al.* 2019). Similar studies on monosymmetric cross-sections like channel sections are limited, although their structural applications such as dooms, stadiums, bridges, these channel cross-sections offer certain advantages such as high performance with minimum weight (Kim, Min & Su 2000a). The current insufficient design information in such sections is due to the complexity in the analysis; as such, members usually experience eccentric loading when in use, since their centre of gravity and shear centre do not coincide (Dahmani & Drizi 2015).

According to a study by Dahmani and Drizi (2015), no specific design rules were available for LTB of eccentrically loaded channel sections used as beams. Thus, no existing literature clearly outlines design guidelines to address the LTB in arches of Al alloy channel sections subjected to transverse point load. In a study on LTB on Al beams by Wang, Yuan, Shi and Cheng (2012), the authors recommended consistent detail analysis for structural Al alloys in general. In another study, De Louw (2007:81-82) outlines that channel sections, if not loaded at the shear centre, the load capacity of the cross-section is influenced by imperfections mode and the magnitude of the eccentricity. Thus, research studies have also focused on the impact of imperfections on the load-carrying capacity on fixed end arches subjected to point load at the shear centre. Other factors, such as the slender ratios and included angles, were considered.

Generally, investigation on the LTB stability in-term is the load-carrying capacity of freestanding circular fixed end arches of structural Al alloy open thin-walled members is not exhaustive. No existing study has investigated the influence of imperfections on the LTB load-carrying capacity on channel arches developed at constant slender ratios and span length. Although section imperfections are generally affected in the curving process, which influences members' resistance to LTB (Yang & Kuo, 1986; Piloto, Real & Franssen 2000; Spoorenberg 2011). Research by Wang *et al.* (2012) made use of structural Al alloy 6061-T6, to analysed LTB load-carrying stability of thin-walled channel section arches with fixed end subjected to a transverse point load. In addition, the study considered the effects of the imperfections on arches developed at constant slender ratios and span length at different included angles, in other words, shallow, moderate, and deep arches.

Due to the complexity involved in analysing arches under such loading and boundary conditions, the overall analyses will focus on the FEA methods. However, this method would be validated analytically with existing solutions. The geometric and material nonlinear imperfection analysis (GMNIA) approach of Torsten Höglund (2010) and Valeš and Stan (2017) using shell element was adopted to apply imperfections.

1.1.1 Purpose of the study

The purpose of this study is to investigate the imperfections impact on LTB stability in terms of load-carrying capacity for fixed end arches of 6061-T6 Al alloy channel sections subjected to a transverse point load at the shear centre and proposed a design guideline to such an impact. The investigated imperfections include material nonlinearity, initial geometric imperfection and residual stresses.

1.1.2 Significance of the study

Although structural Al application in structures, as a load-bearing skeleton, is becoming more popular, designers are very sceptical about its resistance to LTB. The reason being, loaded structural Al is more likely to be unstable due to low Young's modulus of elasticity, compared to other structural steels (Wang *et al.* 2012). Through this research, the information provided could be used to enhance the designs of curved structural members, more specifically arches of monosymmetric sections such as thin-walled channel of Al alloys. The provided information would reduce the uncertainty in designers and the use of conservative solutions when it comes to addressing the stability problem due to LTB in curved Al channel members; therefore, improving the green-metal application in structures, since Al alloys are sustainable and justifiably described as green metals (Efthymiou, Cöcen and Ermolli 2010).

In addition, the outcome of this research should provide the information needed for the design of curved Al members such as arches. This information, coupled with Al desirable properties, should give Al suppliers such as Hulamin (Pty) Ltd, South Africa, additional details on their Al catalogue. Such an advantage should boost customer consumption through further application of structural Al alloys channel sections in structures.

1.2 Problem statement

Lateral-torsional buckling is a recurring stability problem within curved structural members, particularly in curved structural Al members due to their low Young's modulus. The frequent occurrence of this stability problem can lead to structural failure if left unaddressed. Despite increasing rates of Al application in structures, there still exist insufficient design guidelines to address LTB in curved structural Al members like arches that are used as a load-bearing skeleton in structures. Therefore, design basics to solve this stability problem in structural Al monosymmetric channel section arch members need to be developed.

1.3 Objectives

1.3.1 Main objective

The main objective of this research is to determine the imperfections impact on the LTB load-carrying capacity for fixed end arches of 6061-T6 Al alloy channel sections developed at constant slender ratios and span length subjected to a transverse point load at the shear centre.

1.3.2 Specific objectives

i. To develop the finite element (FE) models of fixed end channel arches at constant slender ratios and span length under transverse point load at shear centre and determine their effects on the elastic and elastic-plastic axial compressive and bending actions
ii. To validate both the elastic and elastic-plastic analyses
iii. To determine as specified in point (i), the elastic LTB loads of the arches at the different included angles
iv. To determine as specified in point (iii), the elastic-plastic LTB loads due to the applied imperfections
v. To examine the prebuckling effects on the LTB loads and behaviours

vi. To evaluate the effects of the imperfections on load-carrying capacity and propose the design necessitation of imperfections during Al channel arches design under such a loading and boundary conditions.

1.4 Limitations and scope of the study

i. Arch models were limited to thin-walled open shape 6061-T6 Al alloy equal flange channel sections. The width-to-thickness ratios of the specimen were selected within limits, according to Mazzolani (2004) and EN (2007), to avoid failure due to local buckling.
ii. All arches were freestanding circular and the boundary conditions considered were out-of-plane and in-plane fixed, while loaded transversely at the shear centre through a welded plate to allow for LTB.
iii. For the imperfections, the material mechanical property was based on those provided by Aerospace Specification Metals Inc (2012) and the plastic behaviour was based on the bi-linear law. The initial geometric imperfection was based on the recommended values, as reported by Spoorenberg (2011) study. Meanwhile, the residual stresses considered are those recommended by Snijder *et al.* (2008a) for channel sections.
iv. The ABAQUS FEA software was used for this study due to its availability at the Vaal University of Technology and that it is highly recommended for academic work. Also, this software is better in nonlinear capabilities and specific algorithms are more robustly accurate.

1.5 Research outline

The overview of this dissertation's purpose and significance, related studies, methodology, results, findings and analysis, proposed solutions, conclusions and recommendations are presented in five chapters.

Chapter 1 gives an overview of the proposed dissertation through thorough problem identification and explains the significance of the study.

Chapter 2 focuses on the different existing methodologies and findings related to the main and sub-objectives of this dissertation.

Chapter 3, which presents the research methodology, is divided into two parts. Part I illustrates the details of finite element analyses (FEA), which include the development of the FE models and the results. Part II illustrates the validation of the FE model with existing analytical solutions.

Chapter 4 presents the discussion of the results and evaluates the impact of imperfections on the LTB load-carrying capacity.

Lastly, Chapter 5 summarises the different findings in the previous chapters, conclusions and proposed recommendations for future studies.

Chapter 2: Literature review

2.1 Introduction

This review study refers to an arch as a beam that is curved in elevation, which supports are prevented from moving together or apart while loaded in its plane (Spoorenberg 2011). Arches are similar to curved beams, with the only difference being in the supports. Curved beams experience displacement at one or both support(s) (La Poutré 2005). Thus, information sources that refer to curved beams as arches and vice versa were redefined to avoid mixed of information in the review study.

The overview of this literature review is confined to instability in circular freestanding arches due to lateral-torsional buckling (LTB). However, other reported studies were referred to for simplicity. Thus, the entire chapter is structured as follows. Section 2.**1** deals with the general structural stability of members. Section 2.**2** deals with the different methods used to measure buckling. Following this, Section 2.**3** covers the literature on freestanding circular arches subjected to in-plane loading and predominantly failing by LTB. The section gives an overview of the theoretical, numerical and experimental studies. In the reported review studies, factors that may influence the out-of-plane LTB stability loads were covered. Some of these factors were the included angles, slender ratios, cross-section and imperfections. The imperfections consist of material nonlinearity, initial geometric imperfection and residual stresses. Lastly, Section 2.**4** provided an overall critique of the different reviewed literature and conclusion.

2.1.1 The basic theory of stability

The theoretical study of buckling in thin-walled curved beams starts with stability equations (Kang & Yoo 1994b). The accurate prediction of the stability limit is of central importance in the design of the thin-walled structures (Kim, Min & Su 2000a). In Wesley's (2017) study, buckling stability problem is an essential stability problem to be considered in structures and structural members. Typically, if stability in a structure or a critical member of the structure is not addressed, a slight change in load may cause a change in displacement. For large displacement, the member or structure may become unstable and collapse (Galambos & Surovek 2008:1). The principle states of stability and, in counterpart instability, in the structural system appear to be in the stable state, unstable state and the indifferent or neutral state (Gambhir 2004:4). These different states are often explained through the principle of the ball's position at differently shaped surfaces, as shown in figure 2.**1** (Ahnlen & Westlund 2013:13).

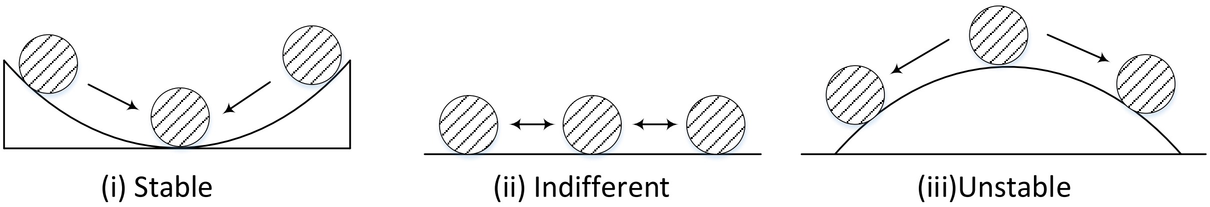

Figure 2.1 The different principle state of stability

Source: Ahnlen and Westlund (2013:13)

From figure 2.**1**, it can be seen that the stable state of the structural system is when the system can return to its initial state of equilibrium after experiencing a small disturbance, the minimum energy of the system. The indifferent state is when the system stays in the initial position caused by the disturbance; that is, the energy of the system is at maximum.

The unstable state is when the disturbance on the system generates forces that will keep moving the system away from the initial condition (Ahnlen & Westlund 2013:13).

2.1.2 Standard buckling modes associated with instability

In simple terms, buckling is instability that leads to structural failure. It is important to note that structural members can fail in different buckling modes. These different modes are usually categorised based on the load applied and the deformed shape of the member. However, a member load resistance is dependent on the stiffness paired with the different deformations. Thus, in the evaluation of a member's resistance to buckling, the flexural torsional and warping stiffness of the cross-section are vital (Ahnlen & Westlund 2013).

Members are not prompt to a single buckling mode of failure; that is, a member's buckling mode can result from one or a combination of either bending, deflection, torsion and warping (Ahnlen & Westlund 2013). The LTB and Torsional-flexural buckling or Flexural-torsional buckling (FTB), among other buckling modes, happen to be more complicated. The complexity is due to the combination of different failure modes present in the LTB and FTB; that is, bending, deflection, torsion and warping (Galambos & Surovek 2008:236; Wesley 2017:24).

Trahair (1993) considers FTB mode to be a structural failure whereby one or more members of a frame suddenly deflect and twist out of the plane of loading. Wesley (2017:25) describes LTB as a phenomenon that occurs in laterally unrestrained or insufficiently restrained beams. In this phenomenon, the member buckles laterally by deflecting and twisting out of its plane; that is, deformation changes from in-plane deformation to a combination of in-plane deformation, twist and lateral deflection. The resistance of the LTB and FTB modes are governed by flexural stiffness/lateral bending stiffness, torsion stiffness and warping stiffness (Trahair 1993:229; Ahnlen and Westlund 2013:15). Figure 2.**2** shows LTB and the transmission between flexural buckling and torsional buckling that give rise to FTB.

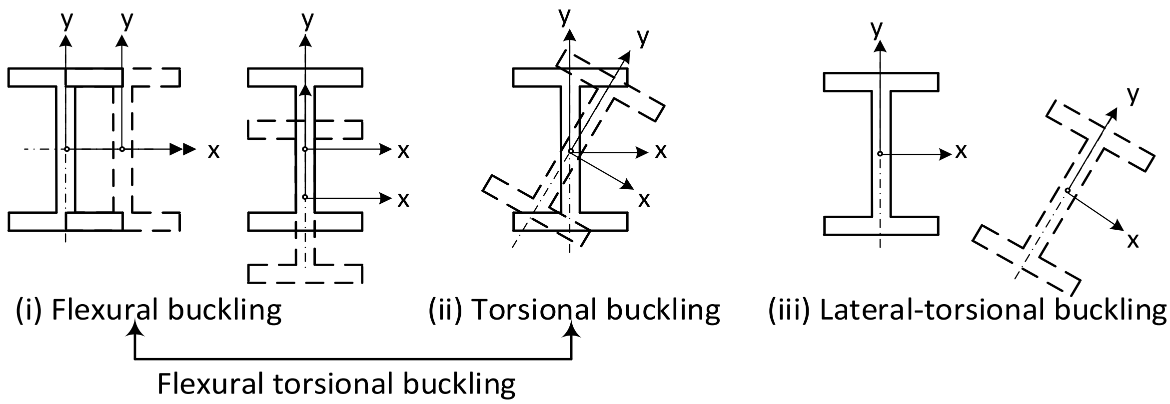

Figure 2.2 I-beam cross-sections deformation by flexural, torsional, and lateral torsional buckling

Source: Ahnlen & Westlund (2013)

From the literature, LTB and FTB happen to have close similarities in the deformation pattern and are carefully used by the researcher. However, it is imperative to understand their differences and similarities to avoid confusion of application as most studies did not distinguish between these two buckling modes.

2.1.2.1 Differences between lateral-torsional buckling and flexural-torsional buckling

First, FTB in an open section is usually associated with the cross-section type, where a cross-section having a single axis of symmetry is considered prone to this instability. This proneness is because both the cross-section centroid and shear centre lie on the axis of symmetry but often do not coincide. In addition, the deformations involved include flexural and torsional deformation (Bernuzzi & Cordova 2016:148). Lateral-torsional buckling, however, in an open section is prone to occur in a lateral unrestrained or insufficiently restrained member. Also, the deformation involves the lateral and torsional deformation (Wesley 2017:25).

Secondly, FTB in compression members is always associated with the axial force that leads to instability. The design against this instability is associated with the critical load (N_{cr}), according to Bernuzzi and Cordova (2016:148), BSI (2007:76). Meanwhile, LTB in compression members is always associated with bending and the design against this instability is associated with appropriate design curve along computation of the critical moment (M_{cr}) (Bernuzzi & Cordova 2016:180; BSI 2007:78; Lam, Ang & Chiew 2013:38; Gambhir 2004:319-476).

Summarily, although in practice both resulting deformation patterns are similar, Wesley (2017:24) considers their differences to be that FTB is caused by axial compression, while LTB is influenced by transverse loading.

2.1.2.2 Similarities between lateral-torsional buckling and flexural-torsional buckling

Based on Spoorenberg's (2011:7) study, FTB is sometimes denoted as out-of-plane stability of arches, whereby the out-of-plane buckling is a combination of the out-of-plane flexural and LTB. In addition, the resistance of LTB is governed by flexural, torsional and warping stiffness (Ahnlen & Westlund 2013). Besides, both LTB and FTB occur as a result of bending co-occurring with a twist in a member (Ziemian 2010:598).

Bernuzzi and Cordova (2016:180) and Ziemian (2010:562) state that LTB is one of the ultimate limit states considered in design standards for a member in bending. Segui

(2012:141) presented FTB as an essential limit state problem that can occur only with unsymmetrical cross-sections.

Summarily, the load at which this instability can occur may be much less than that which will cause full moment or load capacity to develop (Lam, Ang & Chiew 2013:38). Also, both instabilities are affected by imperfections. These imperfections include the initial geometric imperfection, material nonlinearity and residual stress, among other factors, such as cross-section, included angles, slender ratios and end supports (BSI 2007:52; Lam, Ang & Chiew 2013; Bernuzzi & Cordova 2016:148).

2.1.3 Stability of arches

An arch is said to be freestanding when it is only supported at its ends (La Poutré, 2005). Unlike beams whose global instability is denoted by LTB, the stability of freestanding arches is summarily presented in three stability phenomena shown in figure 2. **3** (Spoorenberg 2011:7); that is, for an ideal solid-rigid freestanding arch with no imperfections, having fixed supports and loaded with typical force, F.

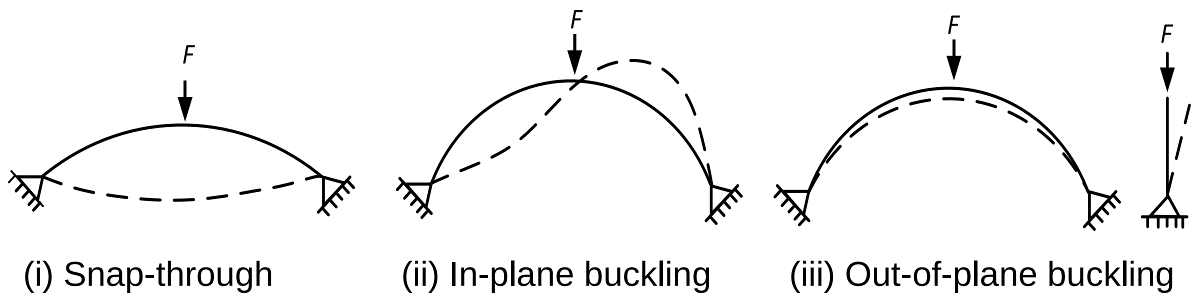

Figure 2.3 Freestanding arches stability phenomena. Source: Spoorenberg (2011:26-30)

For freestanding arches, snap-through instability is typical with shallow arches that are restrained against out-of-plane displacement; whereas, for non-shallow arches that are braced against out-of-plane deformation, the in-plane buckling is dominant. This buckling is associated with combined compression and bending. For slender arches, the out-of-plane buckling may occur before the attainment of the in-plane plastic capacity and the arch has significant freestanding portions. This buckling is associated with compression, biaxial bending and torsion (Ziemian 2010:762; Spoorenberg 2011:7). According to Spoorenberg (2011:7), the out-of-plane instability of arches results from both out-of-plane flexural and lateral-torsional buckling. Thus, FTB is sometimes used to represent the out-of-plane stability for arches.

The assessment of beam or column or arch buckling resistance is usually based on the appropriate beam curve. It requires computational analysis of the critical moment for instability by LTB and critical load for instability by FTB (Bernuzzi & Cordova 2016). For beam-columns, a situation whereby stability is to be accounted for in the design, the buckling conditions are defined by the interaction between the critical axial load and the critical bending moment (Bernuzzi & Cordova 2016:269). However, this should be no different for arches since the axial load and bending cause out-of-plane instability. This research, however, will focus on the critical load and moment, which in the literature is associated with LTB.

For LTB to occur in an unrestrained or insufficiently restrained member, the following conditions need to be fulfilled. First, the stiffness around the minor axes of the member must be significantly low compared to the principal axes. Secondly, the applied load must be around the principal axes of the member. Lastly, the torsional stiffness of the cross-section must be low (Wesley 2017:25). These conditions are attributed to some factors, which affect the LTB of a member. These factors also influence the bending moment and axial load, which are considered essential parameters in arch stability design (Pi & Trahair 1998) and beam-column (Bernuzzi & Cordova 2016:269). Table 2.**1** presents the general factors that influence the LTB of structural members.

Table 2.1 Factors affecting lateral-torsional buckling

Factors that affect lateral-torsional buckling		
1	Material properties	Shear modulus (G) Youngs's modulus (E)
2	Cross-section properties	Torsion constant (I_t) Warping constant (I_w) Second moment of inertia about the weak axis (I_z)
3	Geometric properties	Unrestrained length (L)
4	Boundary conditions (refers to supports)	Bending about the major axis Bending about the minor axis Warping
5	Load	Type of loading (distributed, concentrated, etc.) Point of load application (top flange, in the shear centre, bottom flange, etc.)

Source: Ahnlen and Westlund (2013:17)

These factors influence the lateral-torsional instability differently.

- The shear and Youngs's modulus are parameters that define a member's stiffness and ability to withstand any shear deformation.
- Cross-sections with more excellent lateral bending and torsional stiffness are considered to have a higher resistance to buckling.
- Usually, long members are considered weaker in buckling resistance than the short member. Thus, members with a long unrestrained length of the compression flange are prone to this instability.
- For boundary conditions with end supports, the rotational restraint in the plane helps to prevent buckling.
- The applications of the loads and shape of the bending moment diagram between restraints influence the LTB (Lam, Ang & Chiew 2013:38).

In real applications, some additional factors, which are not usually considered in an ideal case, influence the buckling behaviour of a member (Wesley 2017:17). In a PhD research on the structural properties and out-of-plane stability of roller bent steel arches, Spoorenberg (2011) regarded these factors as imperfections. These imperfections include geometric imperfections, material nonlinearity (non-uniform distributions of mechanical properties) and residual stresses. The author went further to conclude that the consideration by other researchers to use the elastic buckling analysis to determine the elastic buckling load for steel sections, is just a small step to instability check.

Instability analysis that takes to account the imperfections is categorised differently. The geometric imperfection category applies to all second-order analysis, while the material nonlinearity and residual stress apply to second-order, elastic-plastic and plastic analysis. More details on the stability analysis are given in Section 2.**2**.

In general, more research studies on instability due to LTB have focused on straight members distinctively (Yang & Kuo 1987). These studies go as far back as in 1899 when Prandtl and Michell performed the first LTB analysis on high thin-walled rectangular cross-sections. Timoshenko later modified their study in 1905 by including the warping effect (Yang & Kuo 1987; Wesley 2017:25). On the other hand, around the 1960s, few researched studies had concentrated on curved members (Yoo & Pfeiffer 1983). Until recently, more interest has been given to curved members such as arches. However, it is in the interest of this research to review studies related to the out-of-plane stability of freestanding circular arches due to LTB and the methods used for measurement.

2.2 Methods used to determine buckling

For decades, researchers have made use of the theoretical, experimental and numerical methods/techniques to determine the buckling of structural members (Ziemian 2010). These techniques, at large, have a common trend used in engineering practices to analyse material applications (Nziu & Masu 2019). The applications of these techniques can be applied alternatively depending on the need, availability and complexity of the problem. These techniques have different sub-methods of applications based on different assumptions and the level of accuracy needed. In practice, the experimental technique is considered the most expensive because the technique requires prototype specimens, equipment and labour cost. Nevertheless, the technique seems to be more realistic (La Poutré 2005). The findings of the experimental methods are also widely used to test and update theoretical and computational models. The challenge, however, lies in the need to match their state with the analytical and numerical models of interest perfectly. For example, it is extremely difficult to obtain a completely fixed support. The application of point loads is another equally difficult practical problem.

2.2.1 Theoretical techniques

In buckling stability analysis, the theoretical techniques have played a vital role in different structural designs (BSI 2007; Ziemian 2010; Lam, Ang & Chiew 2013). The theoretical technique, which uses instability analysis for frames or single member, is categorised under the first or second-order analysis. The first and second-order analyses are further divided into the first-order elastic analysis, second-order elastic analysis, first-order inelastic analysis and second-order inelastic analysis. In summary, these methods describe the elasticity, elastic-plastic and plasticity theories used in buckling analysis (Ziemian 2010:693). These methods are summarised as follows:

- The first-order elastic analysis method is considered the most basic in which the material behaviour is modelled on a load deflections curve as a straight line (linear-elastic). The equilibrium is assumed to occur in the undeformed configuration of the member. This analysis, generally, is associated with economy design structures when the loss of stability is considered minor.
- The second-order elastic analysis represents the material behaviour as linear elastic but formulates the equilibrium on the deformed geometry of the member. From the rigorous analysis, the load level obtained from this analysis can be considered the elastic stability limit of the member.
- The first-order inelastic analysis considers the member behaviour under yielding as load increases. This analysis is limited to first-order response as equilibrium is satisfied only for the undeformed geometry of the member. For elastic-plastic material, the load achieved at this level can be referred to as the plastic limit load.
- The second-order inelastic analysis accounts for member yielding and large deflections consider the effect of material nonlinearity and geometry. The equilibrium equations are formulated on the deformed geometry of the structure, as such are classified as non-linear. The load obtained at this level from the elastic-plastic analysis is referred to as inelastic stability limit load or elastic-plastic buckling load, or ultimate load. This analysis is considered the most accurate

representation of the real strength of a member as the analysis considers fewer assumptions. Due to the inherent complexity, the analysis is often performed using numerical procedures such as with finite element analysis (Spoorenberg, 2011:9; Ziemian 2010).

Solutions obtained through first and second-order theories are, generally, referred to as closed-form, exact, or analytical solutions (Ziemian 2010).

Based on the first and second-order analyses, researchers have used different mathematical methods or principles to derive out-of-plane stability closed-form solutions. Some of these principles include the principle of virtual work (Rajasekaran & Padmanabhan 1989), stationarity in the total potential, or static equilibrium theory (Bradford, Trahair & Chen 2005) and Euler Lagrange theory (Kang & Yoo 1994b; Ziemian 2010:1033). In designs where complex analysis is required and time-saving is essential, these theoretical methods are usually replaced with numerical methods.

Lately, the traditional pen-paper, calculator, hand calculation methods used in the application of these analytical methods have been replaced with mathematical computer software programs. Some of these software programs include Mathcad, MATLAB and Maple, which are used for solving complex differential and simultaneous equations with little waste of time.

2.2.2 Numerical techniques

Numerical methods are considered as solution approximation techniques (Chapra & Canale 2009). These techniques are established for cases where no exact solution exists, or to solve intractable problems, for example, simultaneous equations with many unknowns. The obtained solutions through these methods are referred to as approximate numerical solutions (Nziu & Masu 2019). These numerical methods, along with experimental methods, are used to develop and validate stability equations (Kim *et al.* 2000b).

Several numerical methods are used to provide accurate elastic buckling solutions for thin-walled members. The most used numerical method is the finite element analysis (FEA) that is classified based on the different finite element method (FEM). Examples of the FEM include differential quadrature method (DQM) (Kang & Bert 1997), C^0-type element (Hu *et al.* 1999), numerical integration method, or Newmark's method, finite strip analysis, finite difference, boundary element, generalised beam theory and others (Ziemian 2010:568). Each of the mentioned FEM is suitable for specific applications. This make the FEA method to be generally used in buckling analysis of beams, curved beams, columns, and arches since the FEA gives a broader range of applications that include inelastic analysis; that is, the ability to model nonlinearities and geometric imperfections (Marwala 2010).

The finite element (FE) model for numerical analysis is usually modelled in 2D or 3D forms. The 2D FEA is known to provide efficient analysis that is less accurate compared to 3D, which best describes real situations. There are numerous FEA software used to model 2D and 3D for stability analysis of beams, columns, curved beams and arches. Some of these include Abaqus/CAE, ANSYS Mechanical, ADINA, Autodesk Simulation Mechanical, and SolidWorks Simulation (Ziemian, 2010; Ahnlen & Westlund 2013; Valeš & Stan 2017). Among other factors, the choice of software for application, generally, depends on availability, the type of stability analysis to be performed, the elements to be analysed and the level of accuracy needed (Ziemian 2010:1033; Nziu & Masu 2019).

2.2.3 Experimental techniques

An experiment is described as observation under controlled conditions. Prior to the availability of finite element methods, the analytical solutions were verified with experiment test results. Also, the experimental methods are used to validate finite element models. To date, experimental tests are still used to clarify discrepancies in theories or to validate FE models (Lu, Liu, Bradford, *et al.* 2019).

The elastic and inelastic stability tests have been widely used by researchers to investigate out-of-plane and in-plane behaviour of arches (La Poutré 2005:23). The flexural test, which is a stability test, provides an understanding of the flexural behaviour of the member. As recognised in limited state design standards, the modes of flexural behaviour include attainment of cross-sectional strength and elastic, or inelastic LTB. Thus, the fundamental purpose of the flexural test in the literature was aimed verifying or developing design equations (La Poutré 2005). In order for the test strength to reflect only the variable relative to the design equations, both the material and geometric properties of the test members must be determined (Ziemian 2010:1013).

In the LTB test, the general test measurements include the loads and reactions using calibrated load cells, displacement and distortion using linear variable displacements transducers (LVDTs) and strains using electrical resistance strain gauges. Examples of some LTB test set-ups used by researchers are shown in figure 2.**4**. Other researchers used similar flexural test set-ups, the difference being on the end supports and loading.

1. Data acquisition
2. Control unit
3. Tension rod
4. 90°arch
5. Load introduction frame
6. Supports
7. Actuator
8. HEB 300 test rig
9. Independent measuring frame

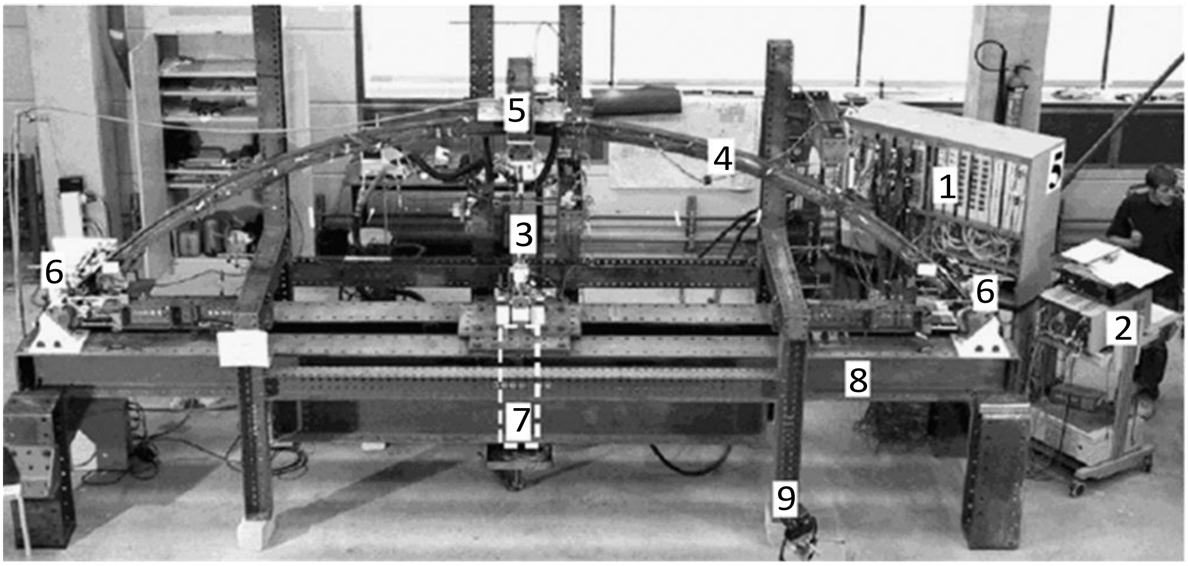

Figure 2.4 Test set-up with 90° arch

Source: (La Poutré, 2005; La Poutré, Spoorenberg, Snijder & Hoenderkamp, 2013)

Despite different experimental set-ups for stability tests due to boundary and loading conditions, Ziemian's (2010:1013) study provided sequential methods, generally, used by researchers. This experimental methodology is summarised as follows:

Firstly, the specimen is acquired. Using different measuring techniques, the geometric properties of the specimen are measured. These include the cross-section geometry, out-of-straightness of the specimen by comparing with manufacturing or rolling tolerances. The material properties such as residual stresses, the tensile and compressive strength are measured using desired standard methods. Once these have been determined, the specimen is then set-up in position with the required boundary conditions. Having the specimen set-up, the different test measurements devices are placed accordingly. These include calibrated load cells used for measuring loads and reactions, followed by linearly variable differential transformers (LVDTs), for measuring displacement and distortions, and finally electrical resistance strain gauges for measuring strains.

The next stage is the cross-check the test procedure that outlines the step-by-step procedure to run those experiments; that is, from the set-up of the specimens and all measuring instruments, to running the experiment. Once this is done, the analysis is carry-out and test report generated. Details of analysis, however, depend on the experiment objectives. Whilst the test report helps to provide detailed information on the test set-up, procedure and specimens to enable other researchers to check the results independently.

In summary, the above techniques, namely theoretical, experimental and numerical techniques, can be and have been used alternatively as per the need and availability. With the experimental technique providing the most realistic behaviour, the technique can be and has been used to validate/ develop numerical and analytical solutions (Papangelis & Trahair 1987). The following sections will provide a literature review on how researchers have made use of these different techniques to address the out-of-plane stability of arches due to lateral-torsional buckling.

2.3 Lateral-torsional buckling

For decades there have been several theoretical, numerical and experimental developments on the elastic LTB behaviour of curved members (Lu *et al.* 2019). Different researchers have presented comprehensive analysis and comparisons of related theories addressing the buckling stability of thin-walled arches. The different theories use different approaches and assumptions (Kang & Bert, 1997). Theoretically, the two conventional methods used by researchers include the direct substitution of the effect of curvature in straight beam equations and derivation from first principle using virtual work. These theoretical methods include assumptions. Assumptions, as set out below, are deemed fundamental in the development of the various proposed curved beam (arches) solutions (Kang & Bert, 1997; Pi and Trahair's 1998).

- The strains are assumed to be small
- The cross-sections do not distort (in-plane rigid cross-sections)
- Vlasov's theory of torsion (Vlasov, 1961) and Euler-Bernoulli theory of bending are used
- The nonlinear strain-displacement relationships contain large displacements and twist rotations and higher-order deformed curvatures
- The effects of in-plane curvature of the arch are included
- The initial crookedness and twist are assumed to vary sinusoidally along the arch axis
- Longitudinal residual stresses are included
- The elastic-plastic incremental stress-strain relationship is derived from von Mises yield criterion, a strain flow rule and a strain-hardening rule.

In view of foregoing assumptions, all theoretical solutions reported in this literature review were based on these underlying assumptions and any exceptional assumption used were mentioned.

As mentioned in Section 2.**1** the LTB behaviour of arches depends on the load and boundary conditions. Several studies have been reported on arches subjected to uniform bending and compression with pinned and fixed support (Papangelis & Trahair 1986a, 1986b, 1987; Lim & Kang 2004; Pi & Bradford 2004a, 2004b, 2004c, 2010, 2012, 2013b; Bradford, Trahair & Chen 2005; Yang, Chen & Fang 2011; Dou *et al.* 2014; Pi, Bradford & Liu 2017). The numerous studies on such arches can be associated with the less complex analysis nature as reported by Liu *et al*. (2017b) study. Also, more research studies have been reported on pinned arches under vertical loading as compared to fixed arches subjected to a similar loading conditions (Papangelis & Trahair 1986, 1988; Pi & Bradford 2003, 2005; Pi, Bradford & Tong 2010; Pi & Bradford 2013a; Dou, Guo, Zhao & Pi 2015; Lu, *et al* 2019). This again is due to the nature of the complex analysis of such arches. The complexity is a result of the acting vertical load inducing a combination of compressive and bending actions in the arch-rib as shown in figure 2.**5** (Liu *et al*. 2017b).

This research, however, is focused on out-of-plane stability due to LTB on fixed ends-arches subjected to vertical loading. Thus, this section summarises the existing literature based on the different measurement techniques to analyse the out-of-plane LTB instability of freestanding circular fixed ends-arches subjected to vertical loading.

2.3.1 Fixed end arches under vertical loading

In this section, fixed end arches refer to arches whose ends are in-plane fixed, out-of-plane fixed, or both. When such as arch is subjected to vertical point load or central concentrated load (CCL), such a load may cause combined bending and axial compressive actions (Pi and Bradford 2003). For example, an arch with pinned or fixed supports subjected to CCL *Q* and fail by LTB may have load reactions, as shown in figure 2.**5**.

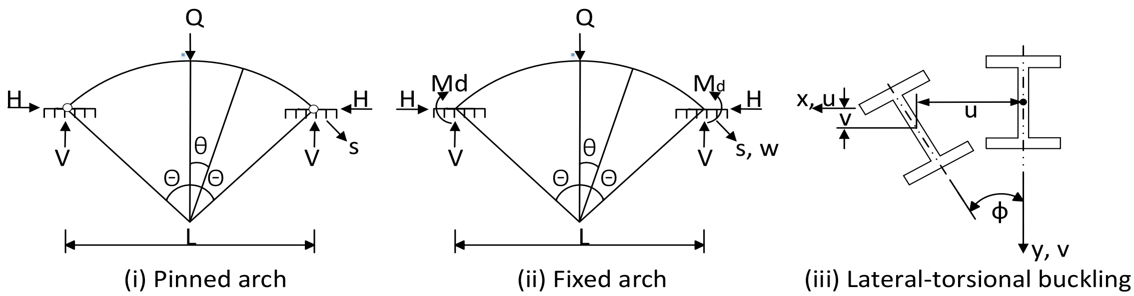

Figure 2.5 Reactions on pinned and fixed arches subjected to central concentrated load

Source: Pi and Bradford (2003)

From figure 2.**5**, *w*, *v* and *u* are the tangential, radial and lateral displacement of the centroid of the cross-section, ϕ is the twist rotation of the cross-section, Θ is half included angle, θ is the angular position of the bending moment, *x* and *y* are the coordinates of a point load in principle axis of the cross-section.

The transverse load applied on an arch may cause no-uniform combined axial compressive and bending actions, as shown in figure 2.**5**. The combined actions make the prebuckling stress state in such arches more complex (Liu *et al*. 2017b). For this, few analytical solutions existed based on the complex nature of the stability analysis. Also, experimental tests have been utilised to study the out-of-plane LTB failure behaviour of such arches. Thus, these sections reviewed the literature on out-of-plane

LTB analysis of fixed circular arches subject to CCL based on the different methods employed by researchers. These include the numerical, analytical and experimental techniques. Also, the summarized literature is divided into studies of elastic and inelastic LTB.

2.3.1.1 Elastic lateral-torsional buckling

Pi and Trahair (1996) proposed a 3D nonlinear finite element model that included the Wagner (warping) and post-buckling effects for analysing elastic arches of double symmetric sections with fixed, pinned and simply supported end conditions. Their proposed solution showed good agreement with existing solutions, as shown in table 2.**2** investigated the effects of the included angles with respect to the load position on the buckling load. These authors observed shallow fixed end arches with included angle $2\Theta \leq 30^o$ with applied load at the crown to developed significant axial compressive actions at the crown. Such an effect was observed to significantly reduce FTB resistance while the negative moment at the ends slightly increases the resistance. At $2\Theta > 60^o$, the negative moments are essential and significantly increase the FTB resistance to about 175 percent compared to pinned end arches. However, the author's study was limited to double symmetric cross-sections. Also, the cross-section was assumed to maintain its shape after deformation and the shear strain, due to bending and warping, is negligible.

Table 2.2 Comparison of results for arches

Included angles in (degrees)	Uniform radial load		Equal moments	
	Solutions by Pi & Trahair, (1996) in (kN)	Analytical solutions in (kN)	Solutions by Pi & Trahair, (1996) in (kNm)	Solutions by Yang, Kuo& Cherng, (1989) in
30	3.6232	3.6502	91.54	91.25
60	2.7496	2.7633	44.76	44.54
90	1.6959	1.6999	26.13	26.07
120	0.7836	0.7836	14.52	14.47
150	0.1962	0.1966	6.37	6.30

Source: (Pi & Trahair 1996; Yang, Kuo & Cherng 1989)

Pi, Bradford and Tong (2010) study proposed analytical solutions for fixed end arches. The authors general LTB load equations remained the same for both pinned and fixed end arches as the authors assumed the out-of-plane boundary conditions to stay the same. However, parameters that represent the prebuckling in-plane axial compressive force N_N of equation 2.1, and bending moment M_M of equation 2.2 were modified as given in equations 2.3 and 2.4. The authors' proposed solution was noticed to have good agreement with results from FEA software ANSYS and other in-house developed FE codes. In addition, they observed that the boundary conditions, slenderness, cross-section and load height significantly affect the LTB load of arches, as shown in figure 2.**6**. Some of these effects have been revealed by Pi and Trahair's (1996) and Papangelis and Trahair's (1986) studies.

Nevertheless, the authors concluded that the load height above the shear centre reduces the LTB load, whereas, below the shear centre, it increases the LTB load. Also, the in-plane fixed conditions increase the LTB load, compared to out-of-plane pinned ends with more considerable significance for shallow arches. Likewise, an increase in slenderness reduces the LTB load with significant effects, depending on the cross-section and included angle.

$N = Qcos\theta\ \Xi_1 + \frac{QH(\theta)sin\theta}{2}$ *and* $M = QR\Xi_2 + NR$ where Ξ_1 and Ξ_2 are given as (2.1)

$$M = QR\Xi_2 + NR \tag{2.2}$$

where the parameters Ξ_1 and Ξ_2 for axial compressive force and bending moment, respectively are given as:

$$\Xi_1 = \frac{(cos\Theta - 1)\left[(R^2 + r_x^2)\Theta(1 + cos\Theta) - 2R^2 sin\Theta\right]}{2\Phi_F} \tag{2.3}$$

$$\Xi_2 = \frac{(R^2 + r_x^2)\Theta(cos\Theta - 1)(sin\Theta - \Theta)}{2\Phi_F} \tag{2.4}$$

with

$$\Phi_F = (R^2 + r_x^2)\Theta(cos\Theta sin\Theta + \Theta) - 2R^2 sin^2\Theta \tag{2.5}$$

where Φ_F is a parameter for in-plane fixed arches, Θ is half the included angle, *R* is the radius of the circular arch, r_x is the radius of gyration of cross-section about its major principle axis, θ is the angular coordinate, *Q* is the central concentrated load and $H(\theta)$ is a step function.

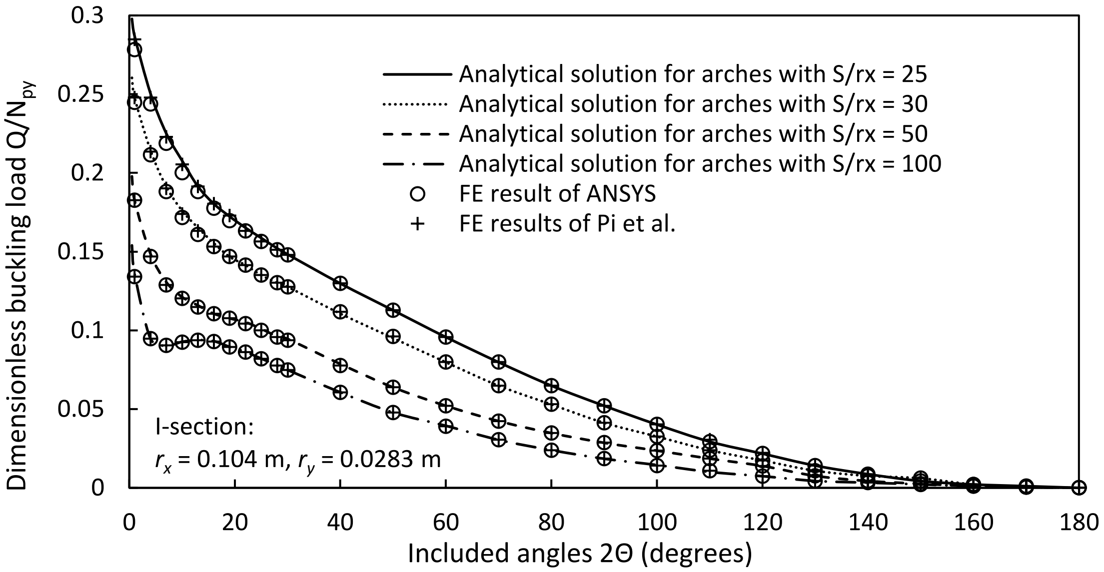

Figure 2.6: Comparison of Lateral-torsional buckling results for I-section arches from different methods

Source: Pi, Bradford and Tong (2010)

Liu *et al*. (2017b) study used the same cross-section as Pi, Bradford and Tong (2010) and investigated the elastic out-of-plane LTB of fixed circular arches subjected to CCL. The authors carried out an accurate prebuckling analysis and the proposed axial compressive force *N* and bending moment *M*, were similar to those of Pi, Bradford and Tong (2010). However, the constants Ξ_1 and Ξ_2 in the latter study was slightly different to that of the former study. The constants that represent the prebuckling in in-plane axial compressive and bending actions that is; E_1 and E_2, respectively in the former study are given in Equation 2.**6**.

$$E_1 = -\frac{\Xi}{2\phi} \text{ and } E_2 = -\frac{B_1}{2\phi} \tag{2.6}$$

with

$$\Xi = (R^2 + r_x^2)\alpha\sin^2\alpha + 2R^2 sin\alpha(cos\alpha - 1) \tag{2.7}$$

and

$$B_1 = (R^2 + r_x^2)(cos\alpha - 1)(sin\alpha - \alpha) \tag{2.8}$$

where

$$\phi = (R^2 + r_x^2)\alpha(\alpha + cos\alpha sin\alpha) - 2R^2 sin^2\alpha \tag{2.9}$$

whereby ϕ is the parameter for in-plane fixed arches, α is half the included angle and the rest are as defined in the latter study. Through the theory of stationary potential energy in conjunction with Rayleigh-Ritz methods, the authors proposed an LTB load solution shown in Equation 2.10.

$$(\mathbf{K}_e - Q_{cr}\mathbf{K}_g)\mathbf{g} = 0. \tag{2.10}$$

where Q_{cr} is the LTB load, $\mathbf{K}_e$ is the lateral-torsional stiffness matrix related to the strain energy, $\mathbf{K}_g$ is the lateral-torsional stability matrix and **g** is the vector quantity representing the lateral displacement and twist. The analytical solutions using steel properties showed good agreement with FEA obtained results using ANSYS software with less than 1 percent deviation. In addition, the authors noticed the slender ratios, load height and end support to influence the LTB load and represented the effects on the LTB load magnitude in graphical form, as shown in figure 2.**7** for an I-section. Since the study was first of its kind, the authors concluded that the study could be used as a base to investigate LTB strength of fixed circular arches in the future.

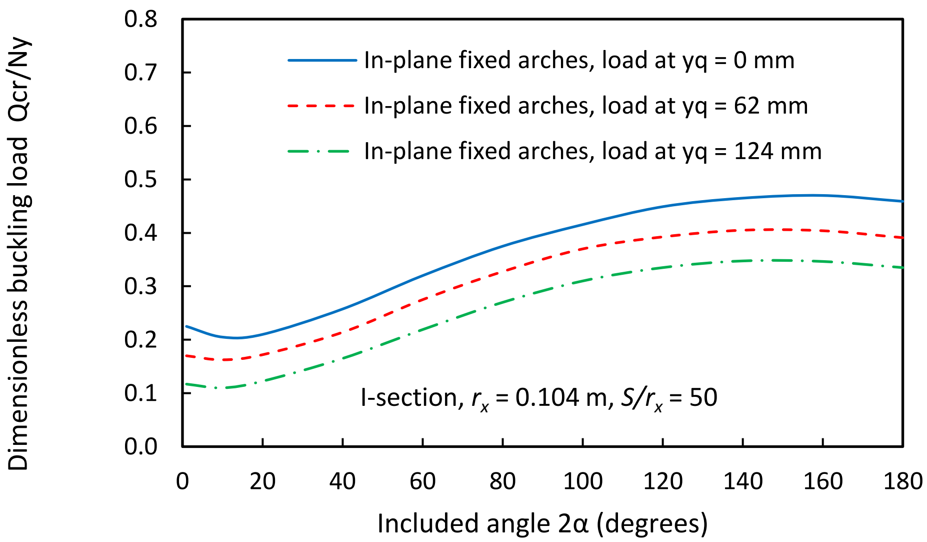

(a)

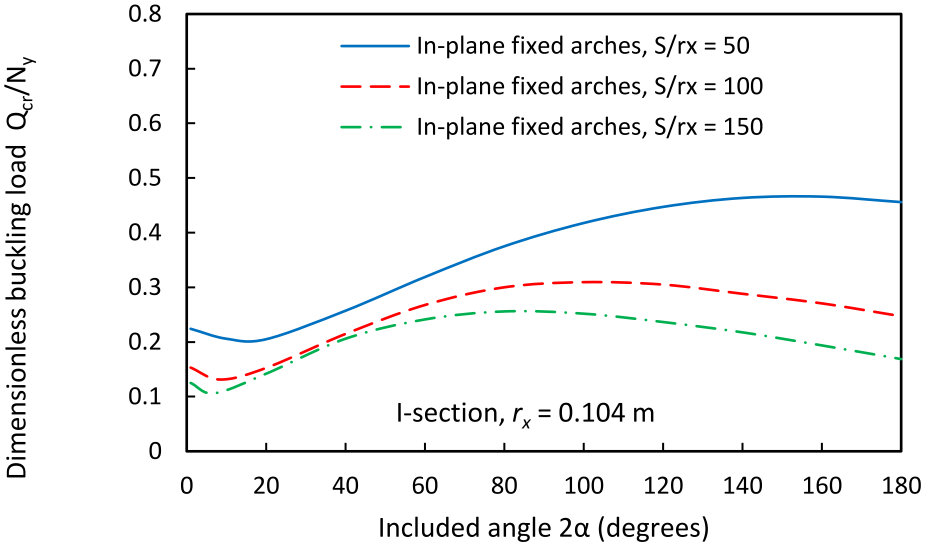

(b)

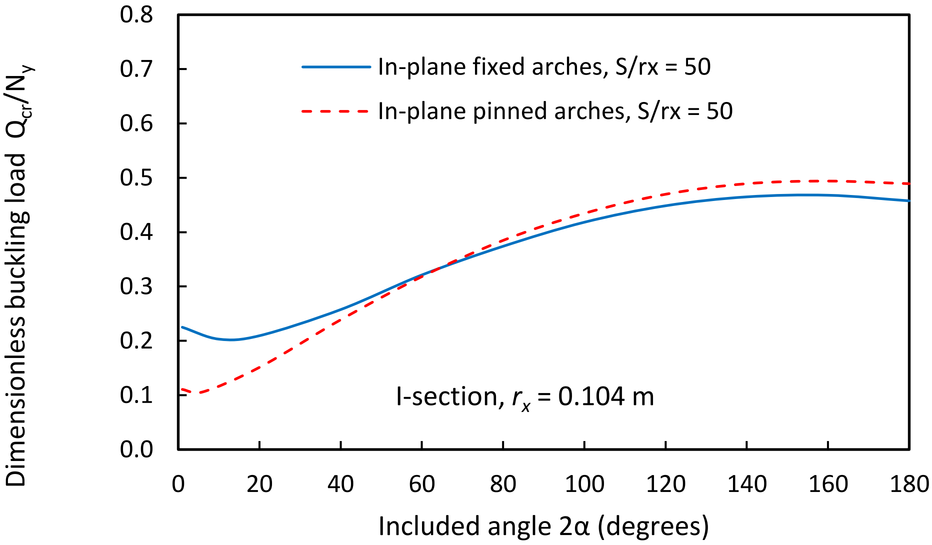

(c)

Figure 2.7: Lateral-torsional buckling loads effects of (a) load height, (b) slenderness and (c) in-plane boundary conditions

Source: Liu *et al.* (2017b)

In another study, Lu *et al*. (2019) used an experimental test to investigated the elastic out-of-plane buckling of circular double symmetric Al I-section arches subjected to central radial point load. The study was an extension of Liu et al. (2017a) and Lu *et al.* (2019) analytical and numerical studies on LTB of arches subjected to arbitrary radial concentrated point loads without and with thermal environment incorporated respectively. The theoretical and experimental results showed good agreement with less than a 5 percent deviation. However, they reported a small difference in the LTB load between arches of in-plane pinned and in-plane fixed end for both experimental and theoretical results. Nevertheless, the authors observed the load height, end supports, slender ratio and included angles to influence the elastic out-of-plane buckling as in the mentioned studies. Besides, their study ignored the effects of imperfection as they focused on elastic out-of-plane buckling on a double symmetric section.

In summary, the above studies related to the LTB of fixed arches subjected to CCL had focused more on double symmetric sections. No studies were reported on the LTB of fixed nor pinned arches of channel sections subjected to CCL. Also, all the reported studies focused on elastic analysis. As a result, the studies ignored the imperfections' effects on the LTB load but only dealt with those of load height, slender ratios, included angles and end supports. Just as the nature of these effects varies in magnitude, as shown in figure 2.**7**, the imperfections may have similar effects on the LTB load and mode shape.

2.3.1.2 Inelastic lateral-torsional buckling

Pi and Bradford's (2003) study developed a rational 3D nonlinear finite curved beam-element model to investigate the elastic, elastic-plastic FTB and post-buckling of double symmetric steel and Al I-sections arches subjected to CCL with fixed and pinned supports. For the prebuckling analyses, the authors proposed Equation 2.11 to obtain the dimensionless elastic axial compressive and bending actions at the crown and Equation 2.13 for elastic-plastic. In another study, Pi and Bradford (2005) used the same FE model. The proposed design equations against out-of-plane failure for fixed steel I-section circular arches that considered the effects of initial out-of-plane crookedness and residual stress. The arches were subjected to different loading inclusive of an in-plane transverse load. The former study compared the results with test results reported by Papangelis and Trahair (1987b) that showed minimal deviation, as revealed in figure 2.**8**. Whereas, the latter study assumed the accuracy of the FE model, as verified by Pi and Trahair (2000), for pin-ended arches. Both studies revealed that the included angle, slenderness and end supports influence the LTB load. Although the studies ignored the effects of material nonlinearity from the curved process, the studies found the initial imperfections and residual stresses to be essential for the strength of the arches; that is, an increase in initial imperfection or residual stress reduces the LTB load. Thus, the elastic LTB load is lower than the inelastic LTB load. Pi and Bradford (2005) provided a general stability design check given in Equation 2.14.

$\frac{N}{Q}$ and $\frac{4M}{QL}$, are the elastic dimensionless axial compressive and bending actions respectively and N and M are given as (2.11)

$$N = Vsin\theta + Hcos\theta \text{ and } M = M_d + VR(sin\Theta - sin\theta) - HR(cos\theta - cos\Theta) \quad (2.12)$$

$\frac{N}{N_Y}$ and $\frac{4M}{Mp}$, are the elastic-plastic dimensionless axial compressive and bending actions, respectively. (2.13)

Where Q, N, M, Θ are as defined by Pi, Bradford and Tong (2010), V is the vertical reaction at fixed support, H is the horizontal reaction at fixed support, θ is the subtended angle, N_Y is the squash or crash load of the cross-section, Mp is the plastic moment of the cross-section.

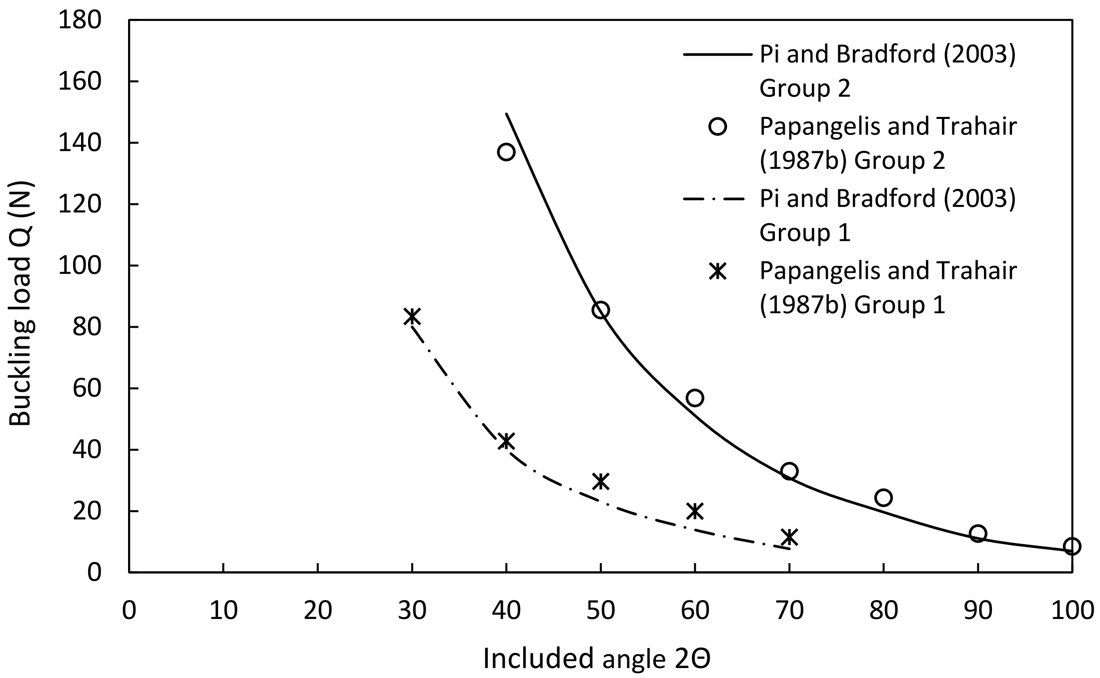

Figure 2.8: Comparison of numerical and test results

Source: Papangelis and Trahair (1987b), Pi and Bradford (2003)

$$\frac{N^*}{\phi\alpha_{any}N_{acys}} + \frac{M^*}{\phi\alpha_{amy}M_{amys}} \leq 1 \quad (2.14)$$

where N_{acys} and M_{amys} are the out-of-plane strength for fixed steel arch in uniform compression and uniform bending respectively, α_{ny} and α_{amy} are the axial compression and moment modification factors, N^* and M^* are the nominal maximum axial compression and maximum moment calculated by first-order in-plane elastic analyses for the arch, ϕ is the capacity reduction factor for uniform compression and bending.

For a better understanding of the buckling behaviour of arches, La Poutré, Spoorenberg, Snijder and Hoenderkamp (2013) conducted several experimental studies. Spoorenberg *et al.* (2012) studied the out-of-plane stability of roller bent freestanding circular arches of steel double symmetric I-sections subjected to single load at the crown using experimental tests and FEA software package ANSYS. The difference in the results was within a 1.18 ratio and the difference among repeated test results being less than 3.2 percent. Based on the FEA results, the authors concluded that the roll bending process impacted the imperfections due to plastic deformation to form an arch, thereby affecting the carrying load capacity of the arch. However, the contrary was observed from the experimental test that showed an insignificant effect. A similar observation was made for the included angle, whereby an increase in the included angle resulted in a slight increase in the failure load.

Guo *et al.* (2015) studied the out-of-plane inelastic buckling strength of fixed steel arches using experimental test and commercial software ANSYS. Both methods yielded results with a small deviation. Based on the obtained results, the authors concluded that the out-of-plane inelastic buckling strength of these arches are also influenced by the initial out-of-plane geometric imperfections, in-plane loading pattern and out-of-plane elastic buckling modes. The obtained results were used to develop lower bound interaction equations for predicting out-of-plane inelastic buckling strength in the design of fixed circular arches against out-of-plane failure. The developed Equation 2.15 took a similar form of Equation 2.14 in which when the moment application factor $\delta_{by} > 1.4$, a second-order in-plane elastic analysis should be carried out to obtain N^* and M^*. A 0.9 safety factor φ was recommended for the proposed design.

$$\frac{N^*}{\alpha_{any} N_{anys}} + \frac{\delta_{by} M^*}{\alpha_{amy} M_{amys}} \leq \varphi \tag{2.15}$$

Likewise, Dou *et al.* (2015) investigated using the experimental test, the flexural-torsional ultimate resistance of pinned circular arches made of double-symmetric I-sections subjected to concentrated loads at different points. The authors observed small disparity between the test results and those obtained from software package ANSYS using BEAM188. Both methods indicated that the geometric imperfections and loading conditions affect the ultimate buckling modes and loads. In addition, the authors concluded that pinned arches buckle in an asymmetric double-wave S-shaped buckling mode. This is different from the one-wave C-shaped buckling mode for fixed arches (Guo *et al.* 2015).

From the above reviewed literature, no theoretical solutions have been reported for inelastic out-of-plane LTB of fixed arches, nor an explicit elastic-plastic analytical solution for prebuckling but from that outlined by Pi and Bradford (2003). Also, no information has been reported for the out-of-plane LTB of Al channel arches with fixed supports subjected to CCL, addressing the effects of included angle, slender ratio, initial geometric imperfections, material nonlinearity and residual stresses. However, one can conclude that the insufficiency is because of the complex nature involved in the analytical method. Also, due to the general complex nature in channel sections as their shear centre and centre of gravity does not coincide.

2.4 Conclusion statement

Numerous research studies have been reported on the out-of-plane LTB of freestanding circular arches. Most of these studies paid attention to double symmetric I-sections, compared to monosymmetric sections like channel. However, such sections may behave differently under LTB due to their shear centre position. The shear centre position makes such sections experience eccentric loading in structures. This factor, among others mentioned in Section 2.**3.1** has been well studied by researchers using one or many of the measure buckling methods mentioned in Section 2.**2**. The numerical methods can be cited as the most preferred method for buckling analysis, since numerical methods are less complex for inelastic analysis, compared to the analytical ones. In addition, numerical methods are less expensive compared to the experimental methods that involve specimens, equipment and labour cost. However, numerical methods may provide results close to experimental results depending on the input variables and limitations mentioned in Section 2.**2.2**. From the literature survey, the following conclusions are made.

From the reviewed literature on buckling stability of thin-walled arches, most researchers always adopted similar assumptions. These assumptions never stopped the discrepancies that existed among theories of freestanding circular arches under uniform bending, uniform compression and vertical loading; that is, for arches at a different included angle, most specifically shallow arches. From the reviewed literature, factors such as end supports, cross-section, included angle and loading are considered general case factors that influence the out-of-plane LTB stability of arches in elastic and inelastic solutions. However, to achieve a more sensible and accurate stability check, imperfections such as residual stresses, geometric imperfections and material nonlinearity should be accounted for in the inelastic analysis. These parameters give a more real state of stability of the arch. For fixed supports, limited analyses exist for central concentrated loads due to their complex nature. This analysis becomes more challenging for channel sections, as it is typically loaded eccentrically, as the shear centre lies out of the plane on the web.

The reviewed literature also showed that studies to address lateral-torsional stability of arches with open thin-walled monosymmetric cross-sections of Al material is limited to monosymmetric I-beams. From the different presented experimental studies, no experimental test data exist for the lateral-torsional buckling behaviour for freestanding fixed arches of channel cross-section from Al alloy subjected to concentrated load. Instead, a variety of experimental studies have been reported on double symmetric steel and Al I-section, monosymmetric I-section and rectangular tube. To which none of these sections shares a similar position of the shear centre (S) and centre of gravity (C) when compared to channel sections. Although De Louw's (2007) study concluded that the general design rule proposed in Eurocode 3 could accurately predict the LTB resistance load for centre loaded channel beams. No such concluded study has been acquired for arches.

In conclusion, from the reviewed literature, no information has been provided for the basic design rule for elastic LTB stability for fixed Al alloy arches of channel cross-sections subjected to central concentrated load. Nor have any inelastic closed-form solutions or approximate solutions from the numerical analysis have been provided for channel cross-section that can be used to designs LTB of fixed arches subjected to central concentrated load. Also, the buckling mode and behaviour of such arches, centrally load, have not been reported.

Chapter 3: Research methodology

3.1 Introduction

This chapter looks at the lateral-torsional buckling (LTB) behaviour of freestanding fixed arches of aluminium (Al) alloy channel subjected to a transverse point load at the shear centre. Fifty-five finite element models were developed from three definite Al channel. The developed finite element models were used to investigate several factors that may influence the LTB stability at different included angles. These factors include cross-sections, slenderness ratios and imperfections due to material nonlinearity, initial geometric imperfection and residual stresses. The finite element models were validated using the analytical method.

3.2 Cases studied

A total of three Al alloy channel sections with definite cross-sections were used in this study. Due to the LTB failure mode investigated in this study, the following guidelines were used to select the different channel cross-sections for analysis.

- First, the members were selected to fall within the Class 1 and 2 categories, as reported by Mazzolani (2004), to avoid local buckling.
- Secondly, the members were selected such that they are highly susceptible to failure by LTB; that is, based on a ratio of the minor moment of inertia I_y to the significant moment of inertia I_x as reported by La Poutré (2005).

From the above guidelines, channel profiles with part numbers 16831, 16825 and 16045, as specified in the Aluminium Standard Profile Catalog by Hulamin Extrusions (2015), were selected for this study. The overview of the channel cross-section is as shown in figure 3.**1**.

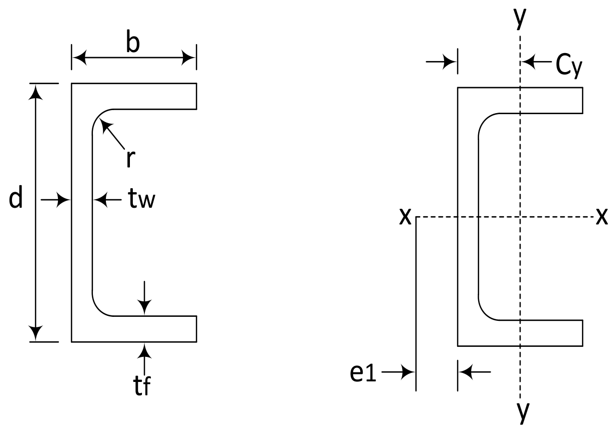

Figure 3.1 General cross-section of the aluminium alloy channel

Whereby *d* is the depth of the section, *b* is the width of the section, t_f is the flange thickness, t_w is web thickness, *r* is the inner radius of the web and flange, e_1 is the position of the shear centre and C_y is the position of the centre of gravity. Based on the defined parameters in figure 3.**1**, table 3.**1** outlines the detailed description of the selected channel cross-sections.

Table 3.1: Detail description of cross-sections studied as per figure 3.1 from Hulamin Extrusions (2015) catalog

Cross-section profiles	**Profile 1**	**Profile 2**	**Profile 3**
Profile number	**16045**	**16825**	**16831**
Cross-section classification	**Class 2**	**Class 1**	**Class 1**
Depth of the section (*d*) in mm	25.4	25.4	38.1
Width of the section (*b*) in mm	12.7	12.7	12.7
Web and flange thickness (t_w & t_f) in mm	1.6	3.18	3.18
r (mm)	0.64	0.4	0.3
e_1 (mm)	3.6	2.5	2
C_y (mm)	3.8	4.3	3.7

The channel profiles listed in table 3.**1** were used to develop freestanding arches models. The models developed from each profile differ from one another with the included angle.

Figure 3.**2** shows a schematic representation of the developed arch model investigated in this study. In figure 3.**2**, *L* is the span length, *S* is the arc length, *R* is the mean radius, *2α* is the included angle, *F* is the applied point load at the shear centre. Based on these parameters, eleven models were developed from each profile using 11 distinct included angles.

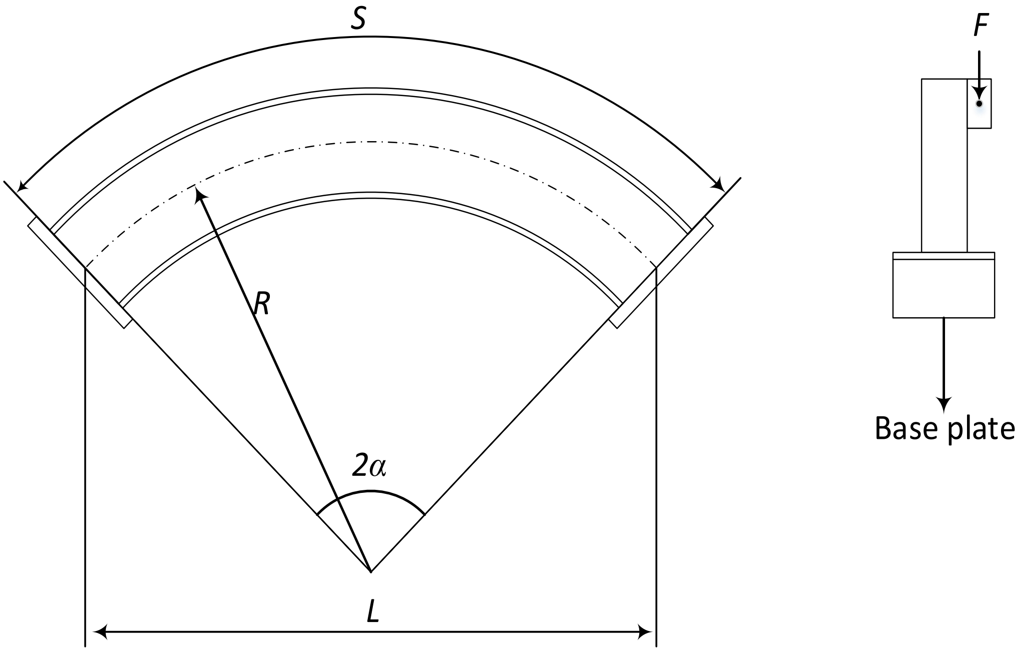

Figure 3.2: Structural representation of the arch model

Thus, the included angle is the primary parameter that distinguishes each model from one another. The secondary parameters are the span length and slender ratio S/r_x (where r_x is the radius of gyration about the major axis). These parameters were used to group the models into group one and group two, as shown in table 3.**2**.

Table 3.2 Structural representation of the different models generated from a profile

Model Number	Group One	Group Two		Included angle 2α [degree]
		$S/r_x = 60$ 500	$S/r_x = 90$ 500	
	Span length L [mm]	Span length L [mm]	Span length L [mm]	
1	500	549.64778	824.47167	5
2	500	549.12464	823.68695	10
3	500	548.25339	822.38009	15
4	500	547.03505	820.55258	20
5	500	543.56301	815.34452	30
6	500	532.54115	798.81173	50
7	500	516.25965	774.38947	70
8	500	495.01392	742.52088	90
9	500	454.69932	682.04898	120
10	500	405.72095	608.58143	150
11	500	350.0277	525.04155	180

The calculations used to determine the variables as presented in table 3.**2** to develop the models used in this study are given in Appendix A. These include radii for arches modelled at $L = 500$ mm and span lengths for arches modelled at $S/r_x = 60$ and 90.

For group one, 33 models were developed; that is, 11 models at equal span length developed from each of the profiles in table 3.**1**. The primary objective of group one was to investigate the influence of the cross-section to LTB stability. On the other hand, group two consisted of 22 arch models developed from profile 2 in table 3.**1**. The group two models were developed at a constant slender ratio S/r_x = 60 and 90. That is, 11 arch models at different included angles developed at each of the constant slender ratios. The primary objective of the group two was to investigate the influence of the slender ratio on the LTB stability of channel profiles. In total, 55 arch models, with an example shown in figure 3.**2**, were developed and used to investigate the factors mentioned above that may influence their LTB stability in terms of the load-carrying capacity.

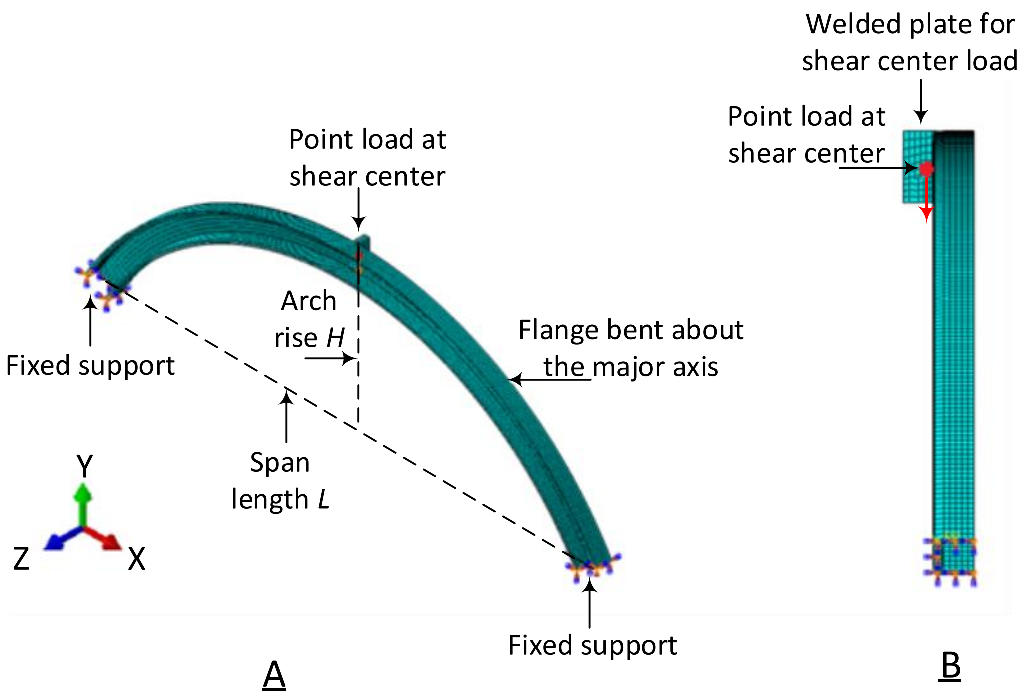

Figure 3.3 Practical representation of the arch model (A) isometric view (B) side view B

Figure 3.**3** shows a practical sample of the analysed freestanding circular fixed arch model of the Al alloy channel section subjected to a concentrated point load at the shear centre.

3.3 Numerical method

Numerical techniques are considered an alternative to experimental and analytical techniques (Ziemian 2010). This technique, when used correctly, can predict real situations. As mentioned in the reviewed literature, several numerical techniques have been used for solving out-of-plane LTB of thin-walled circular arches. However, the numerical technique used in this study is the FEA method. This FEA method was selected because it can conduct elastic and inelastic analyses; that is, the FEA's ability to incorporate material linearity and non-linearities, initial geometrical imperfections and residual stresses, which form the critical parameters being investigated in the study.

The FEA method is considered the primary method in this study since it is cumbersome to quantify the imperfections parameters effects on the out-of-plane LTB through experimental analyses. Also, due to no existing analytical method for analysing the effects of the imperfections on the out-of-plane LTB of fixed end freestanding channel arches subjected to point load at the shear centre. Moreover, for years, the FEA method has acted as a more convenient and reliable tool to investigate the influence of other factors such as included angles, cross-section and in-plane slender ratios on the LTB of arches (Liu *et al*. 2017b).

3.4 Finite element analysis

Different commercial software such as Abaqus, Ansys, Prokon, Adina, LTBeam, Mastan2 can be used for FEA. The commercial finite element software Abaqus/ CAE standard, which was available at the Vaal University of Technology, Vanderbijlpark campus, was used for these analyses. The Abaqus FE method allows different analysis types to obtain distinct response characteristics of a single arch configuration. The software can provide analysis types that cover all the first and second stability analyses, which are linear and nonlinear. This study made use of the following stability analyses in the FEA.

i. *Linear elastic analysis (LEA):* The analysis is the most straightforward in the finite element domain and it is based on the first-order elastic theory (Hooke's Law) and defines equilibrium in the undeformed state of the structure. Nonetheless, the analysis is very vital in LTB analysis of arches as it gives the force distribution in an arch at the onset of loading; that is, it gives information on the axial compressive and bending action in an arch before buckling (at prebuckling).

ii. *Linear Buckling Analysis* (LBA): This analysis uses the second-order elastic theory, which implies the equilibrium is in the deformed state. The analysis determines the elastic buckling load or the elastic critical resistance of an ideal arch and the respective buckling mode or eigenvector. The buckling mode is used to define the shape of geometric imperfections in subsequent analyses. Also, the buckling load obtained in this analysis is used as a parameter to assess the arch's slenderness. In comparison to any other analyses mentioned in this section, the LBA only provides information about the buckling load and mode shape.

iii. *Material Non-linear Analysis* (MNA). This analysis uses the first order elastic-plastic response that ignores the detrimental geometric non-linear effects. As a result, this analysis overestimates the failure load. This form of analysis is a reference study to evaluate the in-plane capacity of the arch, which in turn determines the prebuckling loading effect in an elastic-plastic analysis.

iv. *Geometrical Material Non-linear Imperfect Analysis* (GMNIA): This analysis uses the second-order elastic-plastic theory. The analysis incorporates material non-linearities, geometrical nonlinearities and residual stresses. As a result, this analysis is well-thought-out as the most elaborated type of analysis that provides approximations closer to that of real situations. In this study, the limit load identified in the load-displacement graph is the ultimate failure load.

Table 3.**3** presents a summary of the described stability analyses whereby "N" indicates issues not taken into account and "Y" indicates issues taken into account.

Table 3.3 Overview analysis types and incorporated issues

Issue	LEA	LBA	MNA	GMNIA
Equilibrium defined in the undeformed state	Y	N	Y	N
Equilibrium define in the deformed state	N	Y	N	Y
Significant rotation and large strains	N	N	N	Y
Geometric Imperfections	N	N	N	Y
Residual stresses	N	N	N	Y
Material nonlinearities	N	N	Y	Y
Load multiplier	N/A	β_{cr}	β_{pl}	β_{ult}

Where β_{cr} is the critical load coefficient or the elastic critical resistance of the arch, β_{pl} and β_{ult} are respectively the in-plane plastic load coefficients or in-plane plastic resistance of the arch and the ultimate load coefficient or resistance, after which the arch becomes unstable. Thus, the limit load and the ultimate load in this study are referred to as elastic and inelastic failure loads, respectively. These are the peak loads in the respective analyses that occur before failure.

In summary, this study made use of the LEA and MNA in prebuckling analyses to determine the axial compressive and bending actions. The LBA is used to determine the eigenvalue, also referred to as the elastic buckling load. Lastly, the GMNIA is used to investigate the impact of the material nonlinearity, geometric imperfections and residual stresses.

3.4.1 A general overview of the finite element program Abaqus/CAE

Abaqus/CAE is a software program for FEA and computer-aided engineering. The software application can be used to design and analyse mechanical components and assemblies as well as to simulate the effects of the finite element. In the sections that follow, descriptions of the module steps used in this study are explained. The module phase in Abaqus/CAE summarises the different steps needed to perform an FEA analysis in Abaqus. This study made use of Part, Property, Assembly, Step, Load, Mesh, Job and Visualisation options to carry out the FEA. Although, all the steps were vital in the FEA, the “Step” module was very essential as it determine the analysis type being carry-out, that is; LEA, LBA, MNA, or GMNIA.

3.4.2 Development of the finite element model

This section describes the different module options used in this study to develop the various FE models. A stepwise approach based on the pattern in which the module phases appear in the Abaqus main window was used.

The two major FEAs performed in this research were linear and non-linear analyses. The linear analyses included LEA and LBA, whereas the nonlinear analyses included MNA and GMNIA, also referred to as the collapse analysis in this study. These analyses in Abaqus/CAE are performed in module “Step” using different configuration procedures. In this study, the “Static General” procedure was used for the LEA and MNA, the “Buckle” procedure in “Linear Perturbation” was used for linear Eigenvalue buckling analyses (LBA) and the “Static Riks” procedure was used to carry out the collapse analysis GMNIA. From the analyses, the GMNIA is more complex to carry out in Abaqus as it required additional modification from the general model used for LEA, LBA and MNA. The nonlinear analysis, GMNIA, which works in conjunction with LBA in Abaqus/CEA to include the model geometric imperfection from LBA, is summarised in figure 3.**4**.

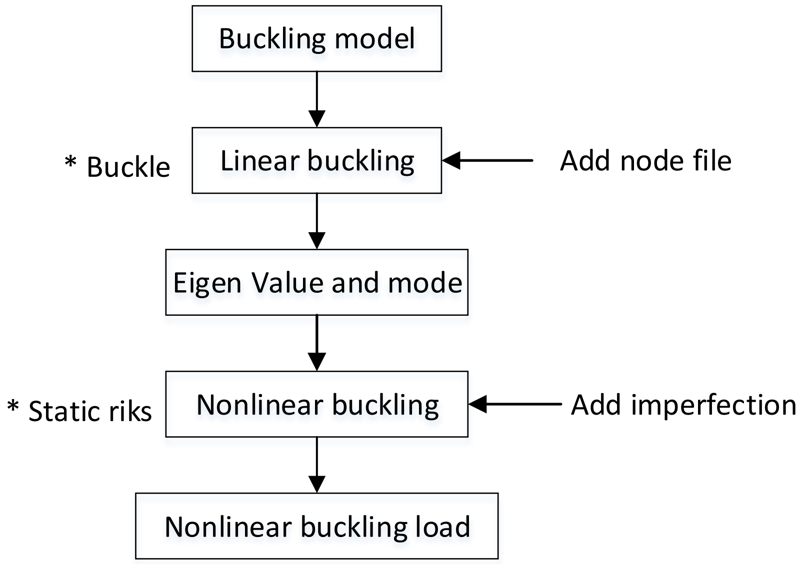

Figure 3.4: Nonlinear buckling modelling in Abaqus standard

As shown in figure 3.**4**, the first step is to build a model. This part is essential to all other FEA. Once a model has been built, linear eigenvalue buckling analysis is performed. The consequent buckling mode shape from the LBA is used to add the geometric imperfections, while the obtained bifurcation load from the LBA is used as the applied load for the collapse analyses MNA and GMNIA. For example, in this study, a unit load is used for linear analysis and the obtained bifurcation load is then used to evaluate the collapse analysis.

Lastly, it should be noted that this study used the same element type, mesh and support conditions for both linear and non-linear analyses. Detail description on the element type and mesh are discussed in Section 3.**4.2**.

3.4.2.1 Part module

In Abaqus/CAE, part creation can be developed within the software or imported from external programs like SolidWorks. The available Abaqus/CAE built-in modelling options were used to create all the different models investigated in this study. The part creation in Abaqus/CAE used for this study is summarised in figure 3. **5**, with the used options highlighted/selected as shown on the "create part" dialogue box; that is, the 3D space, deformable type, with the base feature of shell shape and sweep type, were utilised among other essential functions to create the part shown in figure 3. **5**.

Since Abaqus has no built-in system of units, a consistent SI unit was used throughout the analyses. Due to the model sizes, all geometric parameters used to define the cross-sections and sizes of the arches were input in millimetres (mm). To maintain consistency in the units, the grams, mm and sec were used as input data throughout the analyses.

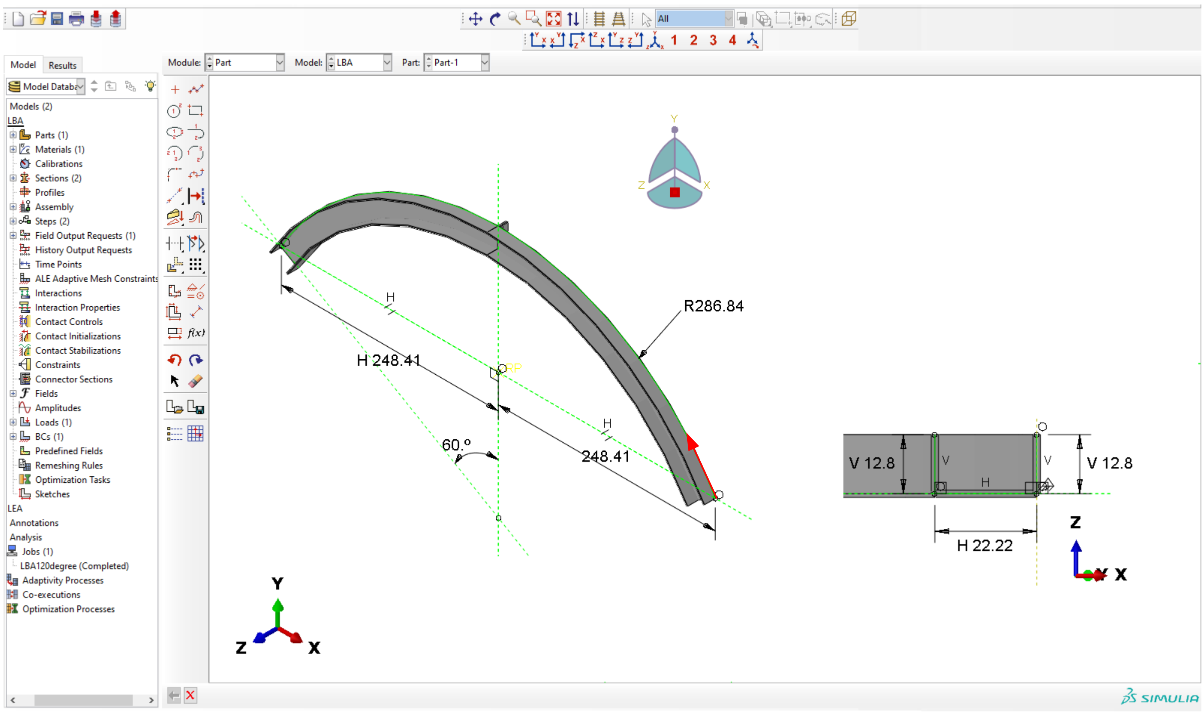

Figure 3.5 Model creation in Abaqus/ CAE

As shown in figure 3.**5**, the direction of the arrows X, Y, Z represents the positive coordinates and the opposite directions of the arrows represent the negative coordinates.

3.4.2.2 Material property module

To assign material property in Abaqus, one can use the property option in the module toolbar. The yield strength of the 6061-T6 Al alloy used in the parametric study is 276 MPa (Aerospace Specification Metals Inc, 2015). The mechanical properties of the Al alloy considered include elasticity and plasticity. For the collapse analysis, a bilinear material law was assumed for the models, whereas a linear law for the LEA and LBA models. The section of material modelling provides more details on the bilinear material law. The elastic material property used a 68.9 GPa Youngs' modulus and a

Poisson's ratio of 0.33. Figure 3.**6** shows the material input data used in the parametric study.

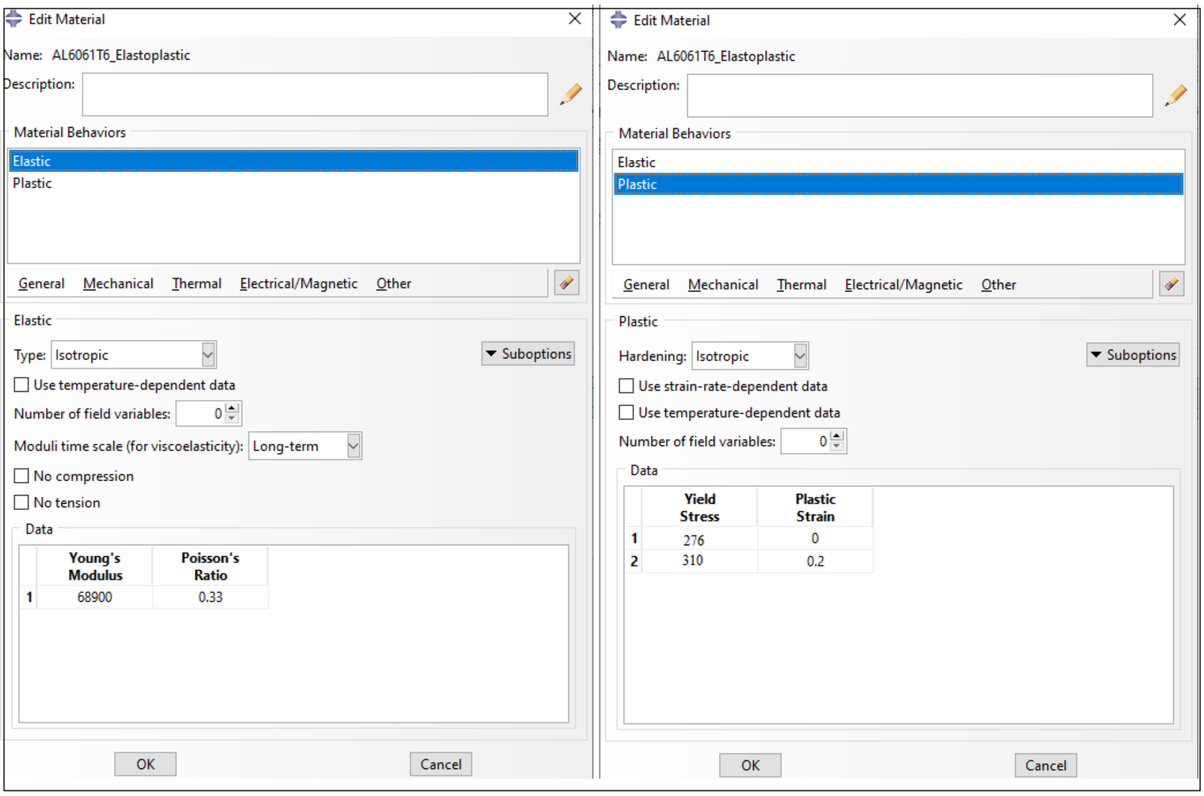

Figure 3.6 Assigning of elastic and plastic material properties

3.4.2.3 Assembly module

Since no part assembly is required for the model, the arch with the welded plate was selected as a single part instance; that is, the entire model shared the same global coordinate and works as a single part.

3.4.2.4 Step module

The Abaqus/CAE Step menu allows one to create a step, select and define an analysis procedure used during the step and to manage existing steps. Abaqus/CAE creates an initial step that cannot be modified. The step allows the definition of boundary conditions, predefined fields and interactions that are applicable at the very start of the analysis. The initial step is followed by the analysis steps that allow one or more analysis steps to be taken. These steps are associated with a specific procedure, which determines the form of analysis to be carried out.

This study made use of the Static General procedure to perform the LEA and MNA and Buckle from the Linear Perturbation procedure for LBA and Static Riks procedure for GMNIA analysis. An example of the step manager for GMNIA is illustrated in figure 3.**7**.

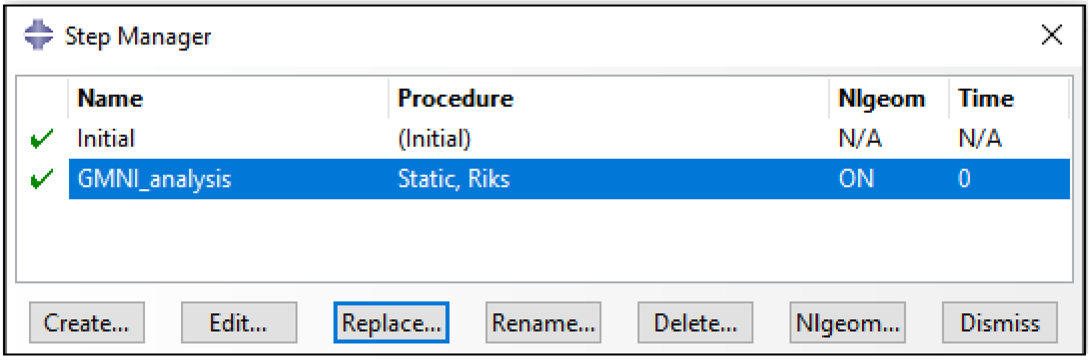

Figure 3.7 The Step-manager

3.4.2.5 Boundary conditions module

The “Load” from the module toolbar in Abaqus/CAE allows the application of boundary conditions. To set the fixed supports condition, the boundary condition “Encastre” was applied to the cross-section ends elements shown in figure 3.**8**. This boundary condition was selected as it ensures no displacement and rotation in the global X, Y and Z-directions, making the supports fully fixed.

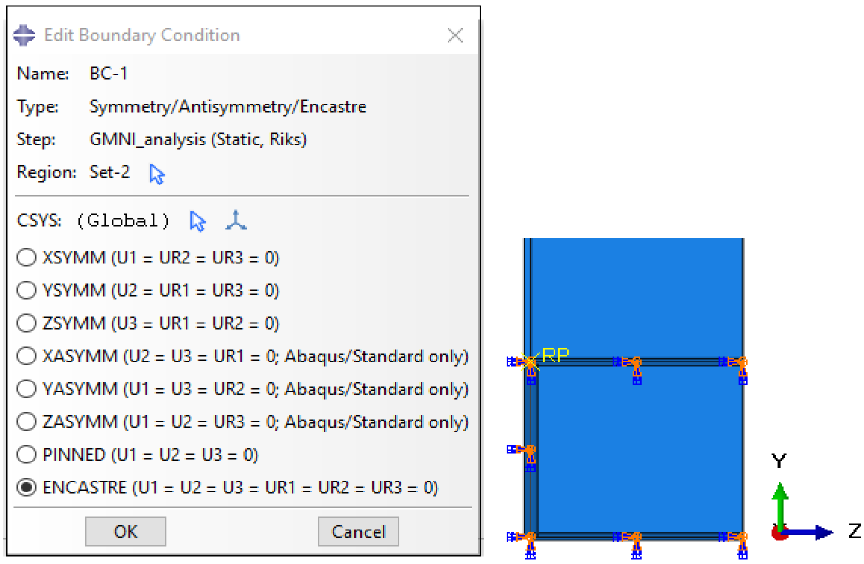

Figure 3.8 Fixed support

3.4.2.6 Loading module

Unlike symmetric sections, in practice, channel section usually experience eccentric loading (Dahmani & Drizi 2015). As a result, the capacity of the section is influenced by both imperfection mode and eccentricity (De Louw 2007). In order to avoid the eccentricity effect, the load was applied at the shear centre using an extra plate of equal length to the depth of the section for the different cross-sections. Based on the model orientation, the applied point load lies in the negative y-direction, as shown in figure 3.**9**. Due to no restriction applied to the point load, the load was free to move in the X and Z-directions based on the deformation taking place. In practice, such point load may be applied as a tie-down transverse load using masses.

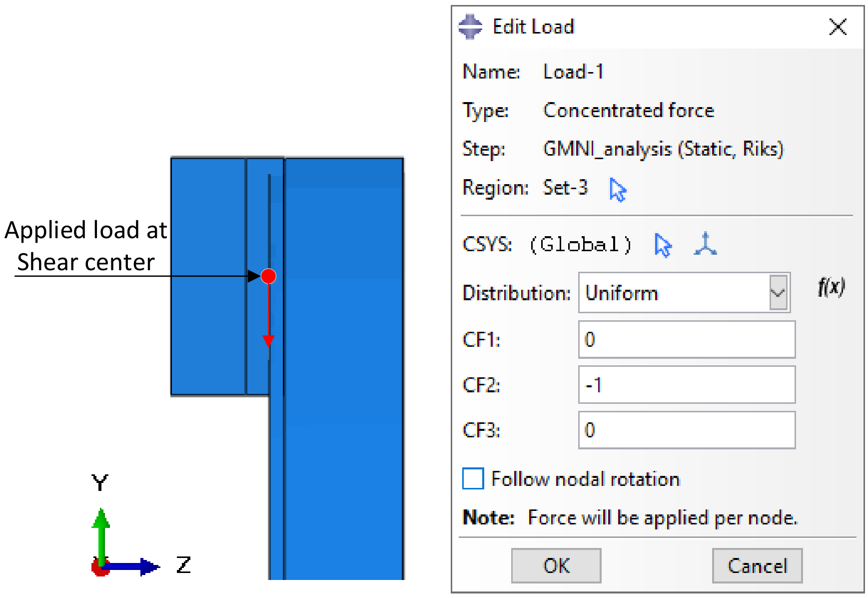

Figure 3.9: Applied point load at the shear centre

3.4.2.7 Element type module

For this study, the standard shell element S4R with a linear geometric order was assigned for the models. This 3D, four-node, quadrilateral, stress, and displacement doubly curved, general-purpose shell element has six degrees of freedom at all nodes; that is, three translations in the x, y and z directions and three rotations about the x, y and z-axes. As such, the element type is known to provide accurate analysis results for thin-walled members and is suitable for analysis that involves finite membrane strains and large rotations (Valeš & Stan 2017).

3.4.2.8 Mesh module

In this study, the arch's finite element mesh was characterised by the elements along the width of the section, depth of the section and along the arch’s developed length. Also, for the finite element mesh control, the quad-dominated elements shape of the sweep technique was selected to enable uniform mesh for residual stress application. However, a convergence study was carried out to select the correct mesh size that provides accurate results with less computational time.

The convergence study performed used a 0.5 mm fine mesh as a reference of the mesh refinement study to select the mesh size. This refinement study was required as the 0.5 mm mesh size was too small for the arch’s sizes, resulting in long computation time and program error during the GMNIA. For the refinement study, an arch with 180° included angle and a span length of 500 mm from profile 16825 having fixed end and subjected to a point load at the shear centre was used. The percentage difference between eigenvalues obtained at different mesh sizes is shown in table 3.**4**.

Table 3.4 Mesh convergence for linear buckling analysis

Mesh Number	Mesh size (mm)	Total Element	Eigenvalue	Percentage difference (percent)	Run time (sec)
1	0.5	63534	8859.2	-	350.29
2	1	17462	8862.4	0.0361	98
3	2	5032	8830.1	0.3285	23.4
4	3	2544	8767.4	1.0416	12
5	4	1666	8661.7	2.25445	9
6	5	1354	8677	2.07799	8

From table 3.**4**, it is evident that the percentage increase of the eigenvalue is influenced by the mesh size. Based on the percentage difference, mesh number 2 of mesh size 1 mm and mesh number 3 of mesh size 2 mm have a small percentage difference of approximately 0.036 percent and 0.329 percent, respectively. However, due to the lead time to run the analysis, mesh number 3 with the global mesh size of 2 mm was adopted throughout the study. For profile 16825, the selected mesh size had six elements on the flange and eight elements on the web. Whereas for profile 16831, the flange had six elements and the web 13 elements, as shown in figure 3.**10**.

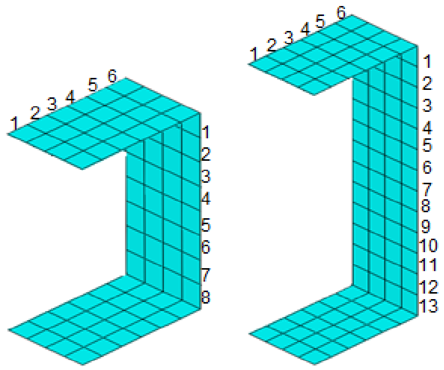

Figure 3.10: Mesh sizes

3.4.2.9 Imperfections

The imperfections are applicable in the GMNIA. These include the material nonlinearity, initial geometric imperfections and residual stresses.

3.4.2.9.1 Modelling of material nonlinearity

The bi-linear elastic-plastic stress-strain curve was used to apply the material nonlinearity. For the bi-linear material curve, the tensile yield strength f_y, ultimate tensile strength f_{ult} and 0.2 percent proof stress were used to define the plasticity of the material presented in figure 3.**6**. By so doing, the effect of the rolling bending process that may affect the material properties was ignored.

Table 3.5 Engineering mechanical properties of the materials

Profile number	Aluminium Alloy	Tensile yield strength f_y $[MPa]$	Ultimate tensile strength f_{ult}	Modulus of Elasticity *E* in $[GPa]$	Poisson's ratio
16045	6061-T6	276	310	68.9	0.33
16825	6061-T6	276	310	68.9	0.33
16831	6061-T6	276	310	68.9	0.33

Table 3.**5** presents the material properties for Al alloys as specified in Aerospace Specification Metals Inc, (2012; 2015) material datasheet.

3.4.2.9.2 Modelling of geometrical imperfection

Initial geometric imperfections are characterised as a deviation from the ideal geometry, as shown in figure 3.**11** (Spoorenberg 2011). This imperfection is classified into two main categories, namely local and overall (bow, global, or out-of-straightness) imperfection. When the residual stresses are explicitly taken into account, a general maximum imperfection $e = S/1000$ for out-of-plane buckling of arches has been recommended in several studies such as Spoorenberg (2011) and Pi and Bradford (2005). Based on the European design code EN BS (2011) for steel, an imperfection bow of amplitude $e_0 = L/150$ that incorporates the residual stresses is recommended for out-of-plane buckling of class d cross-section arches. The Eurocode 9 BSI (2007) design code for Al alloys proposed an initial bow imperfection ke_0 for second-order analysis of LTB. The recommended value for coefficient $k = 0.5$.

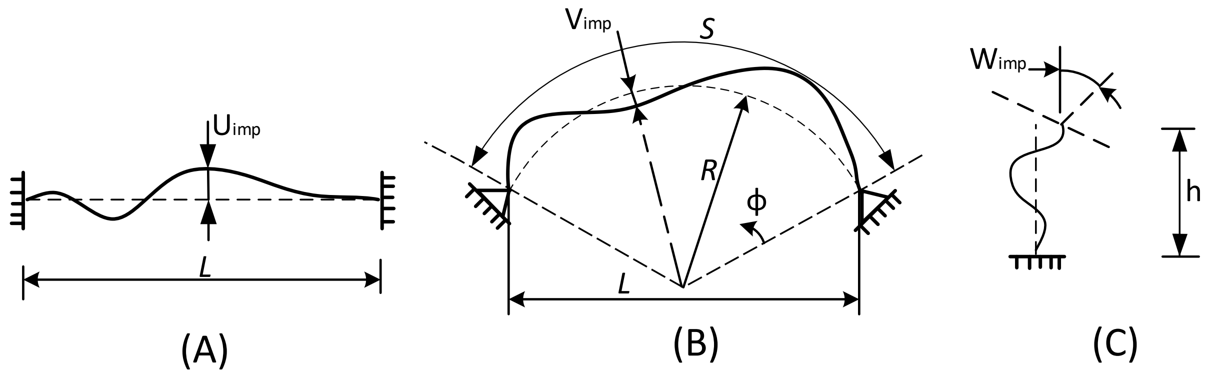

Figure 3.11 Geometric imperfections (A) lateral imperfections, (B) Radial imperfection elevation and (C) Twist imperfections

where *h* is the height of the arch at the twist, u_{imp}, v_{imp} and w_{imp} represents the lateral, radial and twist imperfections, respectively. For this study, the geometric imperfection, $e = S/1000$ was assumed since the residual stresses were considered explicitly. However, few analyses were also conducted to observe the behaviour of the arch due to imperfection bow recommended for design by the EN BS (2011) in association with Eurocode 9 BSI (2007).

To apply geometric imperfections in Abaqus, a unique keyword "*FILE NODE, U" needs to be applied in the LBA. This keyword enables the geometric imperfection from LBA to be called through in a nonlinear analysis using a unique keyword "*IMPERFECTION, FILE = file name, STEP = step number." The called through deformation from LBA is multiplied by the geometric imperfection calculated value to represent the geometric imperfection of the model due to the roller bending.

3.4.2.9.3 Residual stress

Residual stresses are stresses left in the solid material after the original cause of the stresses has been removed. Despite the regular table values of residual stress for I-sections, those of channel sections are not common as stated by Wesley's (2017) research study. As a result, there exists insufficient information that represents the initial stress on a channel roller bent arch. Therefore, the residual stress model presented by Snijder *et al.* (2008) as shown in figure 3.**12** that assumed a fully plastic original stress state, was implemented to represent the initial stress state of the arch models. The positive signs represent tension, while the negative signs represent compression.

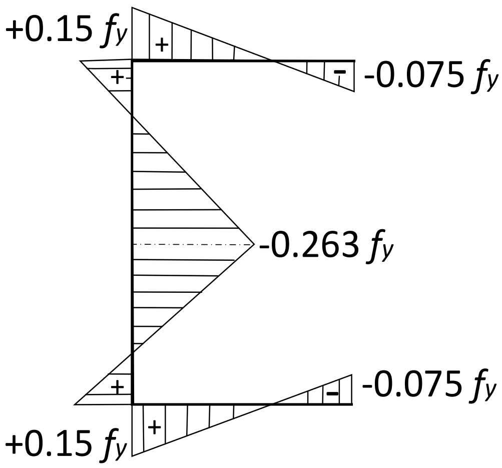

Figure 3.12 Residual stresses on channel section in equilibrium

where f_y is the yield strength of the Al alloy. In Abaqus, the residual stresses were applied at Gauss integrated points that corresponded with the centroid elements. The integrated stair pattern used to apply the residual stresses over the elements is shown in figure 3.**13**.

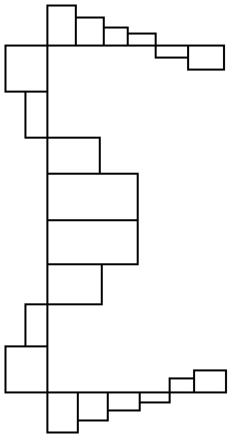

Figure 3.13 Integrated points for residual stress application

After the application of the residual stress into the element, a solution step using static general procedure was carried out to check the force equilibrium in the cross-section using the normal stress S11. It can be seen in figure 3.**14** that trivial differences existed between the stresses inserted and internal stresses at points of integration. These coherences indicate the presence of internal equilibrium over the cross-sections and the correct application of residual stresses in the models. The unique keyword "*INITIAL CONDITION, TYPE = STRESS" was used to apply the residual stresses in the models.

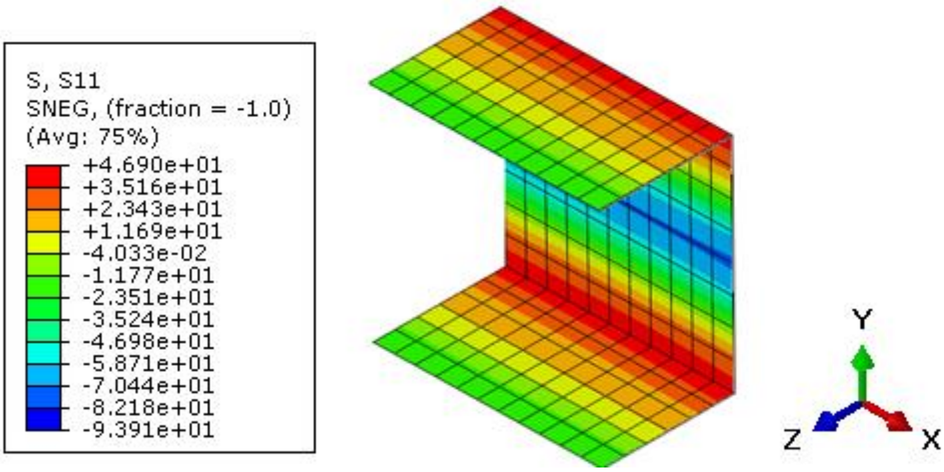

Figure 3.14 Representation of residual stress distribution in the FEA model

3.5 Solving phase

The analyses carried out in this work include the linear and nonlinear analyses. The linear analyses cover the LEA and LBA while the nonlinear analysis covers MNA and GMNIA.

3.5.1 Linear analysis

The LEA was solved with the default static general procedure to determine the axial compressive forces and bending moment prior to buckling. The LBA that is used to extract the eigenvalue and the eigenmode for geometric imperfection application was determined using the buckle eigensolver subspace. The subspace was used because it is faster and ideal for few eigenmodes.

3.5.2 Nonlinear analysis

Unlike linear analysis, the nonlinear analyses performed in this study cover MNA and GMNIA. In solving such an analysis system equation of equilibrium, a stepwise and iterative approach is required. Abaqus provides the Static Riks analysis technique, which was used to run the MNA and GMNIA in this study. This technique is based on the arc length method and it can provide information beyond the ultimate limit point and post-buckling behaviour. Several studies have shown the reliability of the Static Riks method to solve GMNIA and imperfection-sensitive structures, as reported by Sadowski, Fajuyitan and Wang (2017), Ellobody, Feng and Young (2014) and Spoorenberg (2011).

To carry out GMNIA analysis, the load obtained from LBA was used as the point load applied at the shear centre in the negative y-direction, as shown in figure 3.**9**. As shown in figure 3.**15**, an increment of 1000 for load iterations was set to obtain equilibrium. However, the ultimate load was observed before the specified increment. Also, the arc length increment was set at 0.01 minimum and 1E+036 maximum.

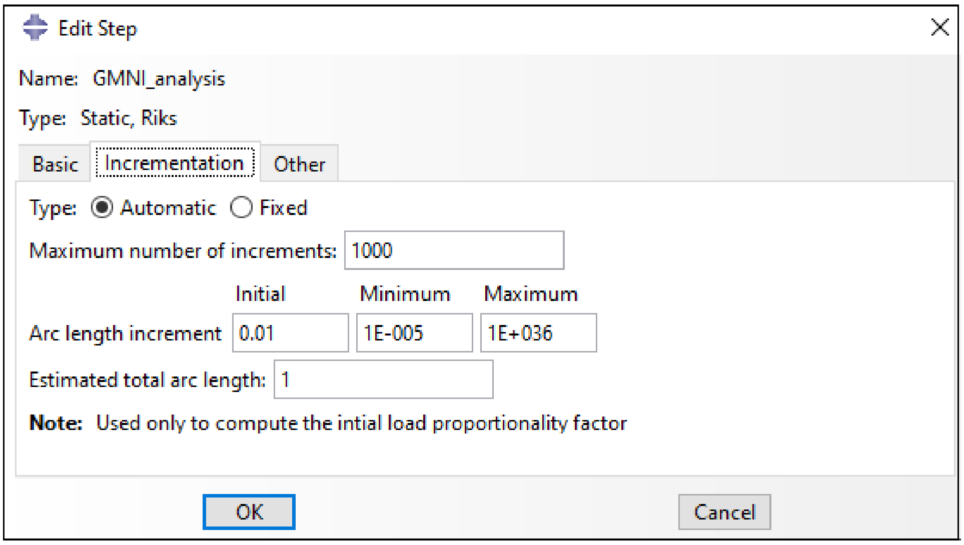

Figure 3.15 Incrementation set-up in Abaqus Riks method

This study used the results obtained from the MNA for the inelastic validation of the FE model; that is, the elastic-plastic prebuckling analysis that obtains the axial compressive force and bending moments. The applied point load used was the ultimate load obtained from the GMNIA.

3.6 Postprocessing

3.6.1 Axial compression and bending actions

The LEA static general method was used to obtain the elastic axial compressive forces and bending moments in the arch models, whereas MNA for elastic-plastic. The points of interest were at the supports and at the crown, where the maximum moments are expected. These outputs are essential in this study since they were used to describe their influence on the model's lateral-torsional stability and used in model validation.

3.6.2 Elastic buckling load and deformation

The LBA in this study was used to determine two critical variables; that is, the elastic critical resistance of buckling (β_{cr}), also known as the load multiplication factor of an ideal arch and the associated buckling mode, also referred to as the eigenvector. Based on β_{cr}, the maximum elastic buckling load (F_{cr}) in this study was obtained by solving Equation 3.**1** reported by (Spoorenberg, 2011).

$$F_{cr} = \beta_{cr}.F \tag{3.1}$$

Where F is the unit load in Newton (N) applied at the shear centre shown in figure 3.**9**. An example of the respective buckling mode (deformation) used to define the shape of geometric imperfection in the GMNIA is shown in figure 3.**16**.

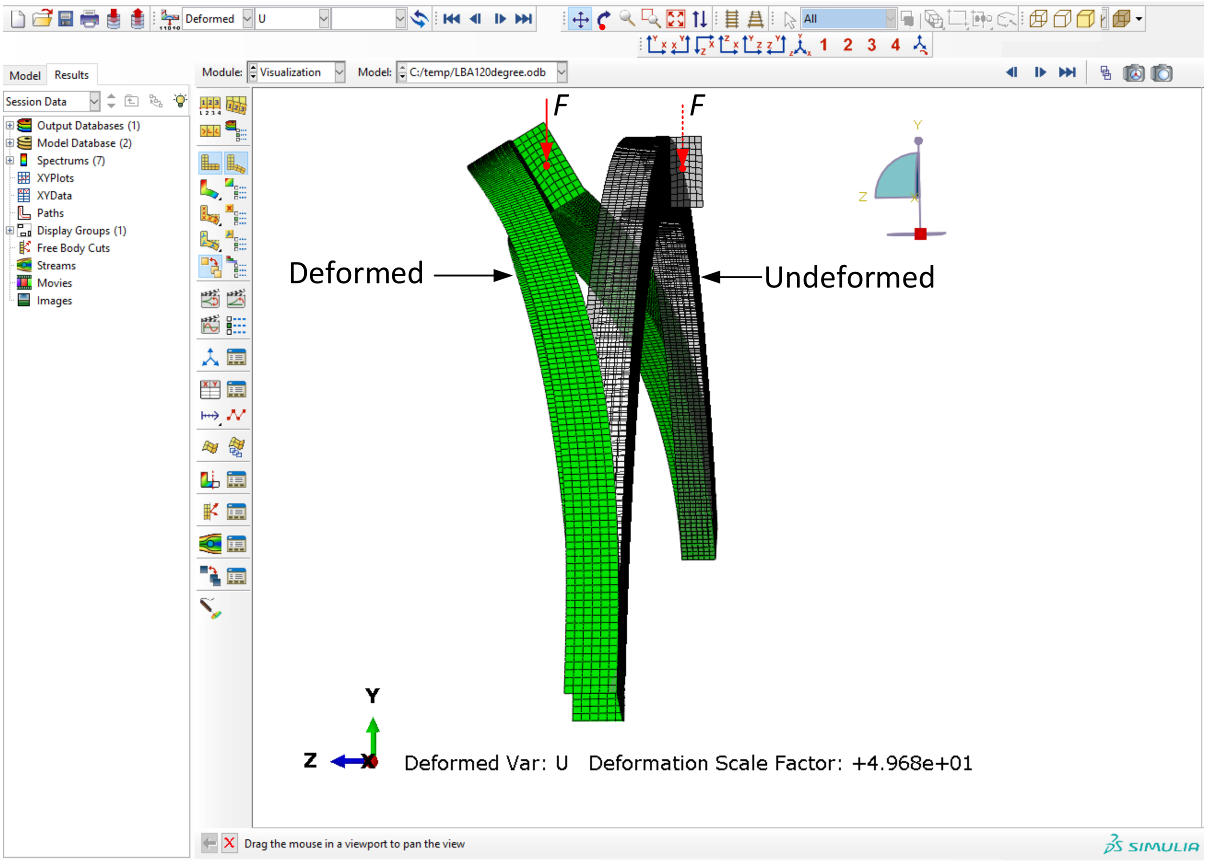

Figure 3. 16 First eigenvector deformation of a 120° included angle arch from profile 16825

3.6.3 Attributes of load-deflection

The GMNIA gives load-deflection characteristics. In plotting a load-deflection graph, the load proportionality factor, also known as the load multiplier (β), is plotted on the ordinate and the output deflection (v) is plotted at the abscissa. These values were obtained from the top centre node at the crown that experiences the most deflection. From Equation 3.**1**, a load multiplier is a load divided by the applied load and the same applies to GMNIA given in Equation 3.**2**.

$$F_{ult} = \beta_{ult}.F \tag{3.2}$$

The ultimate buckling loads (F_{ult}) in this study were obtained as the peak value from the GMNIA load-deflection graph, as illustrated in figure 3.**17**.

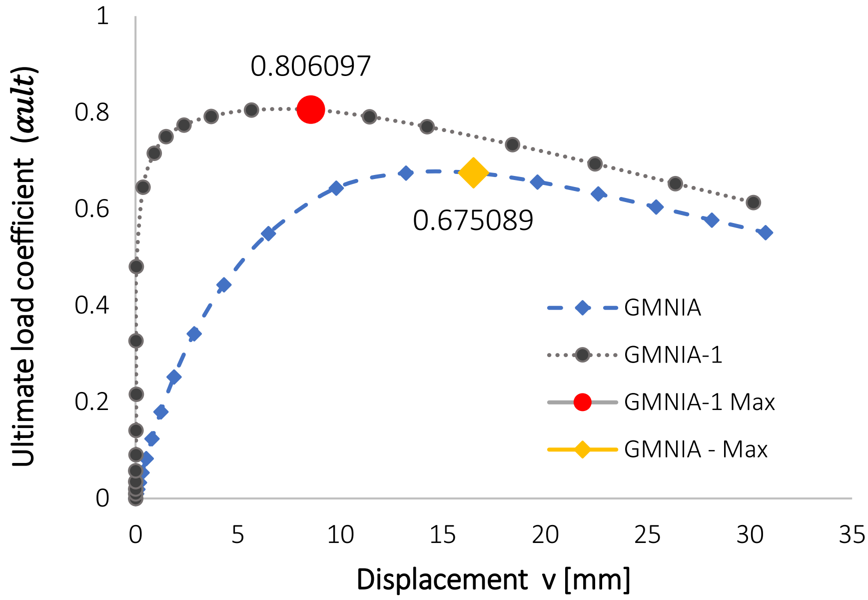

Figure 3.17 Example of a 120º arch load-deflection graph from profile 16825

From figure 3.**17**, GMNIA-1 and GMNIA are the geometric imperfections represented by e_0 and e, given in Section 3.**4.2.9.2**, GMNIA-1 Max and GMNIA-Max represent their respective peak values. The peak points are the areas where the arch models carry the highest load before they collapse. Thus, the load at that point is known as the ultimate load. Since the e_0 imperfections, that is, $L/k * 150$ overestimates the ultimate buckling load and incorporate residual stresses in the formula, the geometric imperfection $e = S/1000$ was used in this study.

3.7 Affirmation of the finite element model

The affirmation of the finite element model, also known as the validation process, can be done analytically or experimentally. Due to the challenges in experimental studies such are prototype, equipment and labour cost, some researchers have used the analytical methods to validate their finite element models, as reported in the reviewed literature. Although it is good practice to use the experimental method for validation, some experimental methods are cumbersome. Hence alternative analytical or different numerical methods are used. This study, however, made used of the analytical methods to validate the FE model.

3.7.1 Standard analytical method

Most standard analytical solutions that exist today for open thin-walled cross-sections were derived from standard double symmetric I-section. The double symmetric I-section has been most favourable by researchers in analytical studies as their shear centre and centre of gravity coincide, making the analytical processing less complicated. Several studies, as reported in the reviewed literature, have investigated the LTB of fixed arches of double symmetric I-section subjected to point load at the crown. The different studies made use of the analytical axial compressive and bending actions invalidating their models. This study made use of similar analytical methods to evaluate the validity of the FE model. Each arch was fixed supported at both ends and symmetrically loaded with a vertical point load *F* at the crown, as shown in figure 3.**8**.

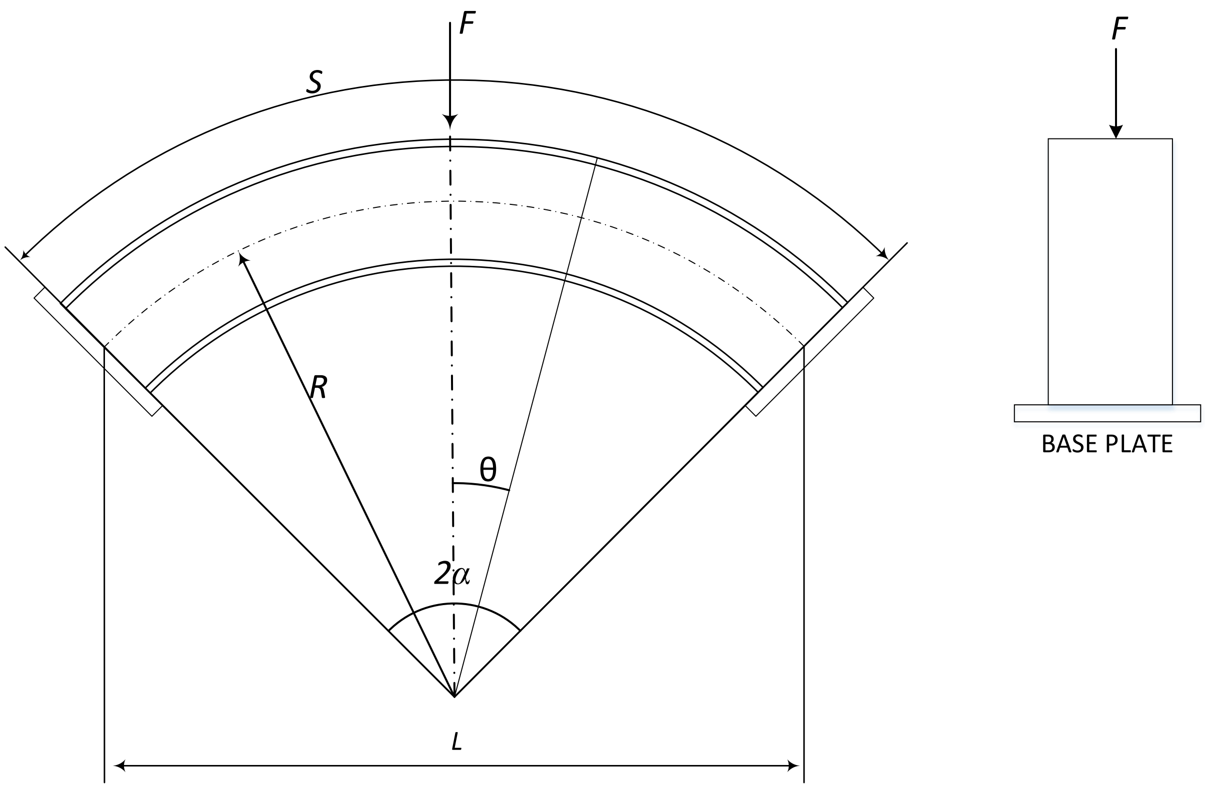

Figure 3. 18 Fixed arch subjected to point load at the crown

where θ is the angular coordinate, 2α is the included angle, *R* is the mean radius of the arch, *L* is the span length and *S* is the arc length. The dimensional properties of the double-symmetric Al I-section arches used for the finite element model verification were as follows; web depth $d = 15.82$ mm, width of the section $b = 7.04$ mm, flange thickness $t_f = 1.42$ mm, web thickness $t_w = 1.38$ mm, shear modulus of elasticity *G* =

28.63 GPa, Young's modulus of elasticity E = 68.9 GPa, mean radius of the arch $R = 500$ mm, point of the applied load from shear centre $y_p = -7.91$ mm and the elastic load applied $F = 1N$. A total of eleven arches were evaluated at the different included angles. The different included angles are 5, 10, 15, 20, 30, 50, 70, 90, 120, 150 and 180 degrees.

From figure 3.**8**, the axial compressive force and bending moment at each support are the same due to the symmetric loading. Also, maximum axial compressive and bending actions are expected to be at the crown as reported by Pi and Bradford (2003). Pi and Bradford (2003), Pi, Bradford and Tong (2010) and Liu *et al*. (2017b) presented similar analytical solutions for fixed arches subjected to point load at the crown, using different analytical methods. This study adopted the analytical solution presented by Liu *et al*. (2017b) and Pi and Bradford (2003) given in Equation 2.**1**, 2.**11**, and 2.**13** for the verification of the FE model. The parameter of interest where the maximum axial compressive force and bending moment, squash or crash load of the cross-section N_Y, and the plastic moment of the cross-section Mp. The elastic maximum axial compressive force and bending moment denoted as N_C and M_C whilst the inelastic where denoted as N_m and M_m, respectively. As shown in Equation 2.**11**, and 2.**13**, the solutions where presented in the dimensionless form as follows:

For elastic analysis, the dimensionless axial compressive force and bending moment at the crown where given as (N_C/F) and ($4M_C/FL$), respectively. While the inelastic dimensionless axial compressive force and bending moment at the crown (N_m/N_Y) and (M_m/M_P),respectively. For further verification of the model, the elastic bending moment at the supports (M_d) and inelastic bending moment at the support (M_D) obtained from Equation 2.**12** were used. Detail equations used to obtain the mentioned parameters for the prebuckling analyses are given in Appendix A.

3.7.2 Finite element model

The methods used to develop the standard finite element model for channel profiles 16045, 16825 and 16831 were applied exactly to develop the models used for the validation; that is, inclusive of the element type, mesh sizes and material properties that were identical to those for channel arches investigated in this study. Also, similar loading and boundary conditions that match those of the analytical solution were used.

These loading and boundary conditions were like those of channel sections. The variables used to validate the FE model included the axial compressive force at the crown and the bending moment at the crown and end support.

Chapter 4: Results and discussions

4.1 Outline

This chapter presents both the analytical and FEA results obtained from the methodology outlined in Chapter 3. First, the elastic and inelastic FE models were validated against existing analytical solutions. The chapter further presented the elastic and inelastic prebuckling behaviours of the different arches modelled from the channel profiles 16045, 16825 and 16831. The arches were developed at a constant span length (L) and slender ratio (S/r_x). The effects of critical parameters (cross-sections, slender ratios, imperfections and included angles) on the elastic and inelastic Lateral-Torsional Buckling (LTB) stability in terms of the load-carrying capacity were investigated. It is important to note that the cross-section effects investigated were the change in web-flange thickness and depth of the section; that is, profile 16045 represented the change in web-flange thickness from profile 16825, while profile 16831 represented the change in section depth from profile 16825. Assuming that these are the only differences from one section to the other.

In this section, most comparisons made between obtained results were presented using graphs. A discussion section followed each graph, as it was noticed that it would be comprehensive to refer to the results graph other than where it appeared. The most critical findings from these sections were discussed at the end of this chapter. All the presented finite element analyses results discussed in this chapter were read at the 75 percent averaging results recommended in Abaqus/CAE standard as the set default value.

4.2 Validation of preliminary finite element analyses results

As mentioned in Section 3.**7** of Chapter 3, both the elastic and inelastic prebuckling analytical solutions were used to validate the elastic and inelastic FE models, respectively. That is; the linear elastic analysis (LEA) was used to validate the elastic FE models, while the material nonlinear analysis (MNA) was used to validate the inelastic FE models.

Various elastic and inelastic solutions computed using analytical and FEA methods are presented in this section. The prebuckling results obtained, that is; the axial compressive force and bending moments are then compared to see how well the FE models agree with the existing proposed analytical solutions. It is important to note that an I-section profile was used to validate the FE models, as mentioned in Section 3.**7** of Chapter 3 since no analytical solution on freestanding circular fixed end channel arches subjected to central concentrated load was reported in the reviewed literature.

4.2.1 Validation of the elastic finite element model

The LEA results obtained from analytical solutions and the FEA based on the elastic properties of the material are presented in this section. The point of interest was at the crown, where the maximum prebuckling behaviour occurred. Also, the bending moment at the support was used to validate the FE models, as the supports have a significant influence on the prebuckling behaviour (Pi, Bradford & Tong 2010).

4.2.1.1 Comparison of the finite element and analytical analyses elastic result

The elastic FEA results obtained from the LEA as were as the theoretical results obtained from formulas proposed by Liu *et al.* (2017b) and Pi and Bradford (2003) given in Appendix A are presented in Appendix B. These include the bending moment at the support (M_d), the dimensionless axial compressive force (N_C/F) and that of the bending moment at the crown ($4M_C/FL$). It is important to note that the bending moment at each support was equal and the axial compressive force at the crown was equal to those at each support as the applied point load was symmetric. The graphs used to compare the FEA and theoretical results are plotted for the different parameters. That is; the N_C/FL, $4M_C/FL$ and M_d values are plotted on separate graphs as the ordinates, with the included angles (2α) as the abscissa. Figure 4.**1** - 4.**3** show the elastic comparison plots for the different variables.

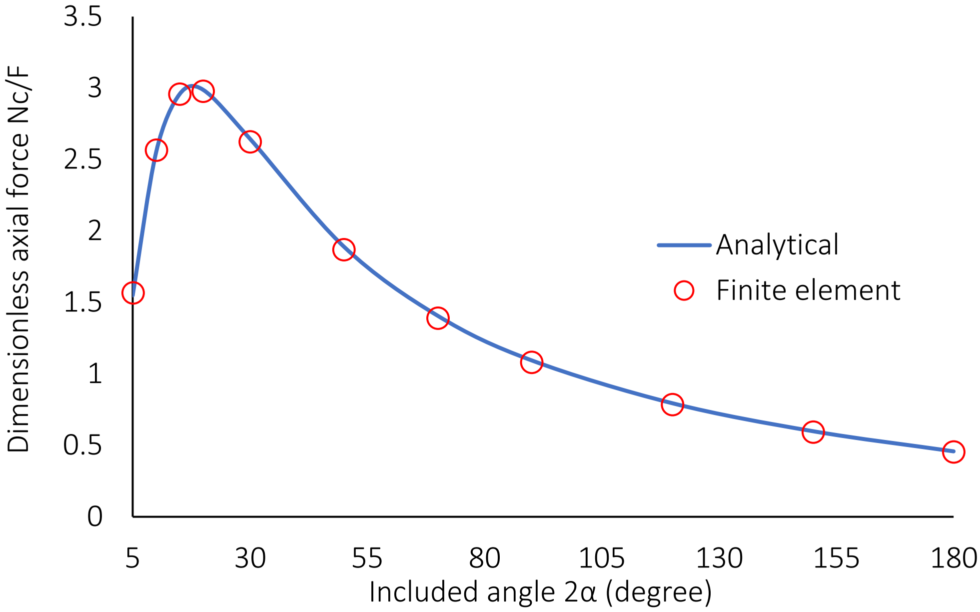

Figure 4.1 Comparison of the finite element and the theoretical elastic solution of the dimensionless axial compressive force at the crown at various included angles

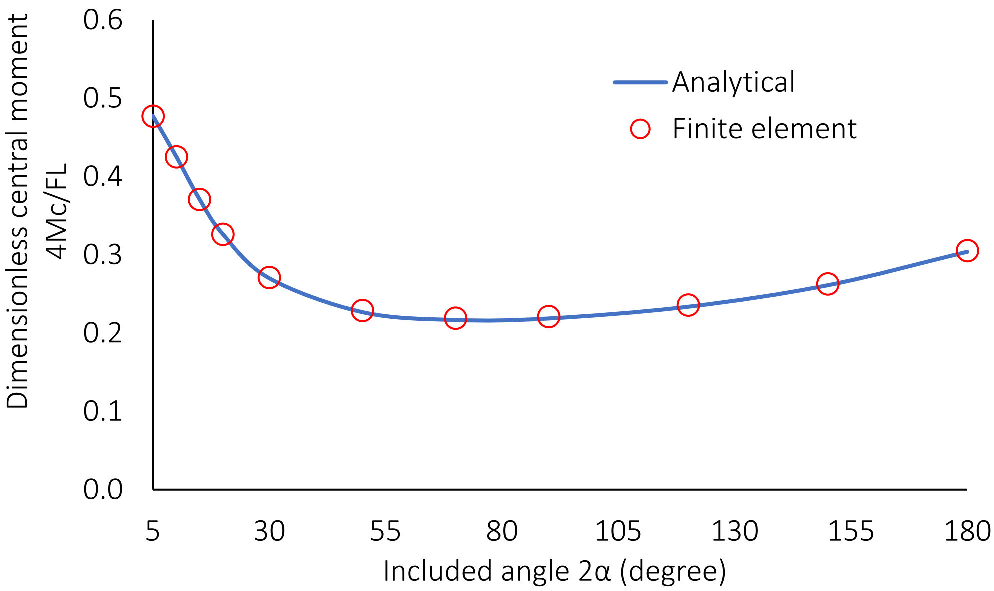

Figure 4.2 Comparison of the finite element and the theoretical elastic solution of the dimensionless bending moment at the crown at various included angles

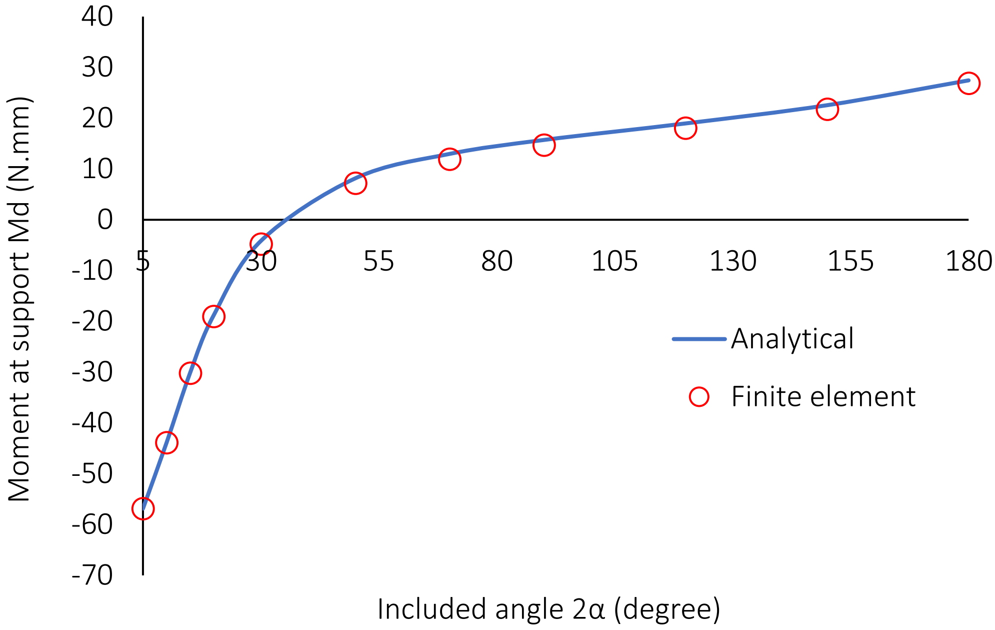

Figure 4.3 Comparison of the finite element and the theoretical solution of the end moments at various included angles

It can be seen from figure 4.**1** - 4.**3** that the deviation between the analytical and FE results are insignificant with close agreements at every included angle.

4.2.2 Validation of the inelastic finite element model

Similar to the elastic FE model validations, the inelastic analytical results obtained from solutions proposed by Pi and Bradford (2003) and FEA results obtained from MNA are presented in this section. Due to the computational time involved, the number of included angles to be evaluated were limited. To compensate for shallow, moderated and deep arches included angles 30, 50, 70, 90 and 120 degrees were used for the validation.

4.2.2.1 Comparison of the finite element and analytical analyses inelastic results

The inelastic FEA results obtained from MNA and the theoretical results based on formulas proposed by Pi and Bradford (2003), as given in Appendix A are presented in Appendix B. These include the bending moment at the support (M_D), the dimensionless axial compressive force (N_m/N_Y) and that of the bending moment at the crown (M_m/M_P). Since the applied load was symmetric, the bending moments at the supports were equal. Like the elastic analyses, the same graphs were used to compare the inelastic analytical and FE results in Appendix B. That is; the N_m/N_Y, M_m/M_P and M_D values are plotted as the ordinates, with the included angles (2α) as the abscissa.

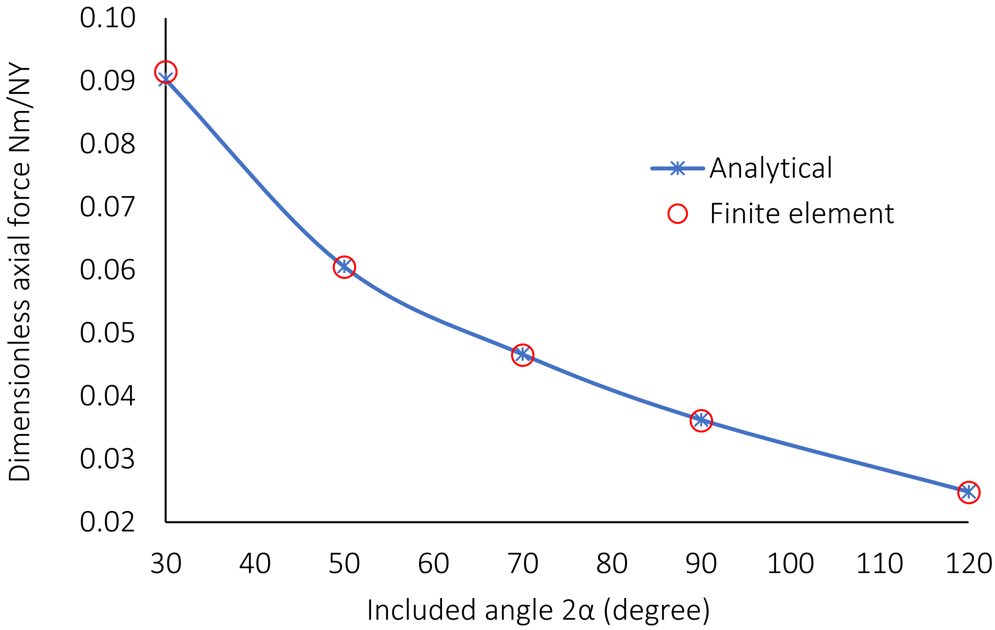

Figure 4.4 Comparison of the finite element and the theoretical inelastic solution of the dimensionless axial compressive force at the crown at various included angles

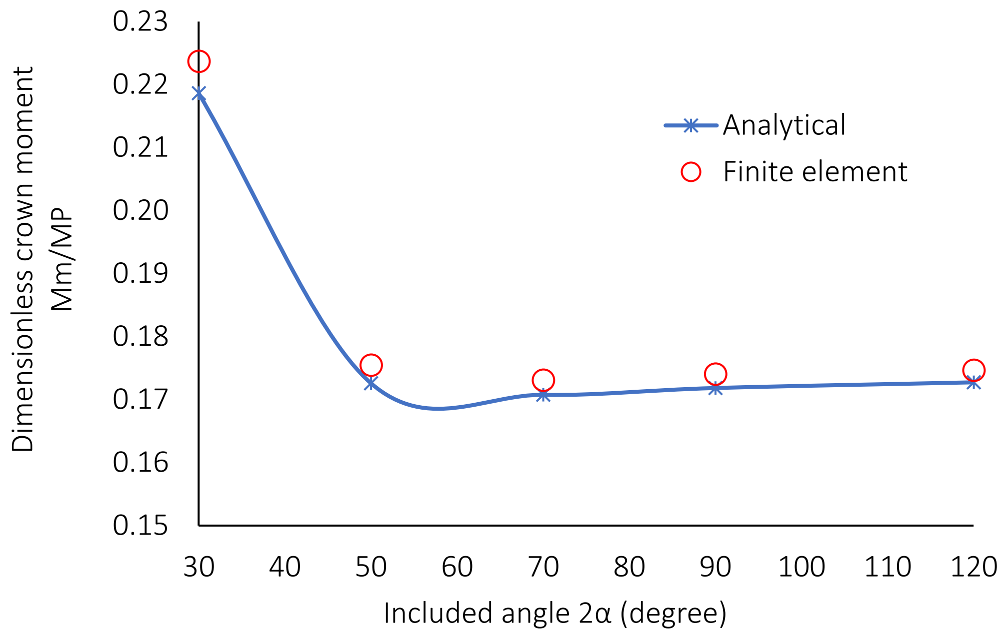

Figure 4.5 Comparison of the finite element and the theoretical elastic solution of the dimensionless bending moment at the crown at various included angles

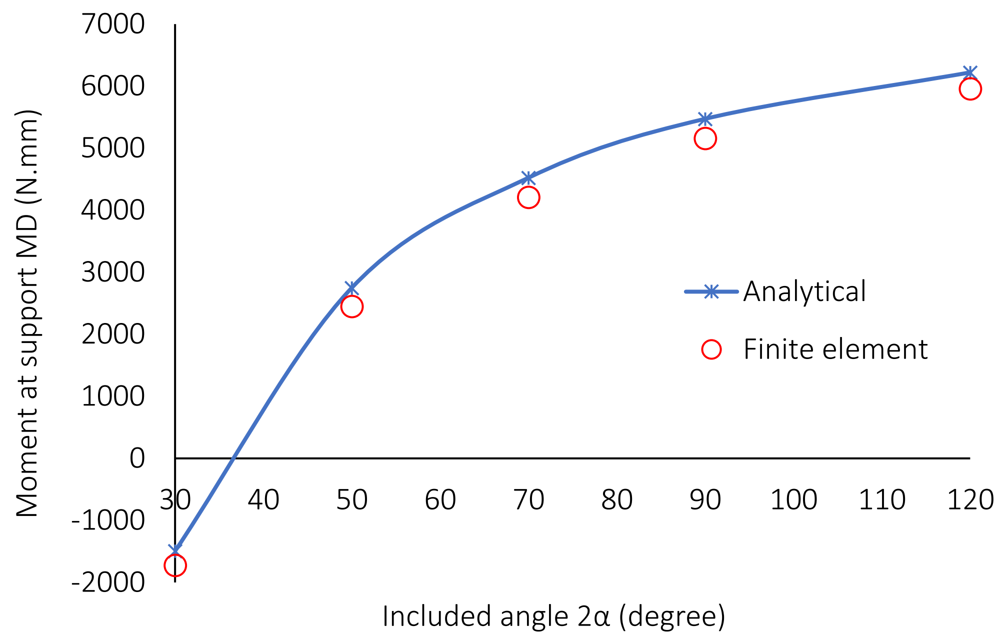

Figure 4.6 Comparison of the finite element and the theoretical solution of the end moments at various included angles

The negative moment at 30° included angle implied that the horizontal thrust force at the support that tends to develop counteracting moments is high, thus high bending stresses.

From figure 4.**4** – 4.**6**, it was observed that despite the insignificant variances between the results, slightly noticeable differences are observed in figure 4.**5** and 4.**6**. Nevertheless, the maximum percentage error obtained was 13 percent, with the majority below 5 percent. From the different observations, it was concluded that the inelastic FE model was accurate and can be used to investigate circular fixed end arches under transverse point load.

In summary, the theoretical and finite element results were compared in this section. Both methods' results showed good agreements for elastic and inelastic analyses. Therefore, it was concluded that the methods used to develop the FE models were accurate, efficient and could represent the expected behaviour of channel profile arches. Thus, the procedure used to develop the Al channel FE models, which were discussed in the sections that follow, was deemed correct.

4.3 Presentation and discussion of prebuckling results

After the validation of the FE models, the channel profiles 16045, 16825 and 16831 were used to investigate the elastic and inelastic prebuckling behaviours of circular fixed end channel arches subjected to point load at the shear centre. The FE model arches were developed at a constant span length (L) of 500 mm and slender ratios (S/r_x) of 60 and 90. The point of interest was at the crown where the maximum axial compressive force and bending are expected to occur (Pi, Bradford & Tong 2010).

The results obtained, that is; the dimensionless axial compressive force (N_C/F) and dimensionless bending moment at the crown ($4M_C/FL$) were presented using graphs. In the preceding subsections, the (N_C/F) and ($4M_C/FL$) were plotted on separated graphs as the ordinates and the respective included angles (2α) as the abscissa. The respective prebuckling plots were then used to describe the rate of increase or decrease of the LTB loads since the LTB loads and behaviours of the investigated arch type are related to the axial compressive force and bending moment developed in the arch prior to buckling (Pi & Trahair 1996; Pi & Bradford 2003; Pi, Bradford & Tong 2010). Nonetheless, the discussions were not limited to the prebuckling effects but also the impact of the slenderness ratios, cross-sections and imperfections.

Since the investigated arches were developed at a constant span length and slender ratios, so are the presented results; that is, the prebuckling results for arches developed at $L = 500$ mm were presented separately from those obtained from arches developed at $S/r_x = 60$ and 90. Arches developed at $L = 500$ mm were used to investigate the effects of change in web-flange thickness and section depth on prebuckling using profile 16045, 16825 and 16831. It is important to note that for such arches developed at constant span length, the slender ratio varies for all three profiles due to the differences in their radius of gyration. Meanwhile, archers developed at $S/r_x = 60$ and 90 were used to investigate the slender ratio effects on prebuckling. Profile 16825 was used to investigate the slender ratio effects since the profile was identified to have an approximate mean cross-section dimensional property among the three profiles.

4.3.1 Elastic prebuckling analyses

The elastic prebuckling results obtained from arches developed at constant span length $L = 500$ mm and those at constant slender ratios $S/r_x = 60$ and 90 are presented in this section. These include the elastic axial compressive forces and central bending moments prior to buckling at respective included angles.

4.3.1.1 The elastic axial compressive force

For all the arches developed, both at $L = 500$ mm and at $S/r_x = 60$ and 90, the axial compressive forces for every arch was obtained at the crown where the peak values occurred. Thus, this section discusses the axial compressive forces obtained at the crown for arches developed at the constant span length and slender ratios.

4.3.1.1.1 Axial compressive forces of arches developed at constant span length

The detailed cross-section profiles 16045, 16825 and 16831, as described in table 3.**1**, were used to evaluate the impact of change in web-flange thickness and section depth on the axial compressive force behaviour of arches developed at constant span length. The results obtained from arches developed at $L = 500$ mm, using the three profiles, are presented in figure 4.**7** as a variation of the dimensionless axial compressive force at the crown (N_C/F) at included angles (2α).

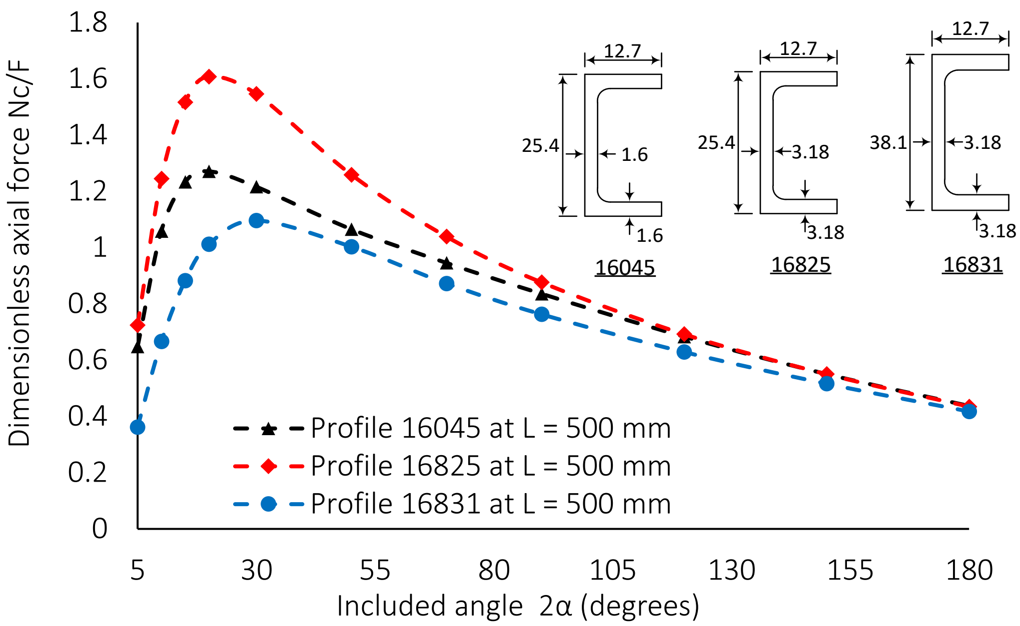

Figure 4.7 Variations in the axial compressive force due to changes in channel sections

It was observed in figure 4.**7** that the N_C/F values for all the cross-sections rapidly increased to a maximum at $2\alpha < 30°$ (shallow arches) and then decreased continuously at included angle 2α > 30°. Also, it was noticed that profile 16825 has an overall high magnitude. The overall high magnitude of profile 16825 was due to the large distance between the profile centroid position and shear centre, compared to the distance between the centroid position and shear centre for profile 16045 and 16832, respectively, as outlined in Hulamin Extrusions (2015) catalogue.

Based on reported studies, an arch developed at a constant slender ratio with a high elastic axial compressive force should have the least LTB load (Pi & Bradford 2003). However, the same remark cannot be made for arches developed at constant span length due to other factors such as torsion constant and bending moment that may have significant influence on the LTB load. That said, the different maximum and minimum N_C/F values in figure 4.**7** along their corresponding included angles are summarised in table 4.**1**. It should be noted that profile 16825 was used as the point of reference for comparison due to its mean dimensional property, as earlier mentioned in Section 4.**3**.

Table 4.1 Maximum and minimum N_C/F values at their respective included angles and percentage differences for arches developed at constant span length

Profile description with dimensions in (mm)			Maximum $\frac{N_C}{F}$ and corresponding included angle		Minimum $\frac{N_C}{F}$ and corresponding included angle		Maximum $\frac{N_C}{F}$ percentage difference at corresponding included angle 2α in (%) *Ref. 16825*
Profile	Web & flange thickness	Section depth	$\frac{N_C}{F}$	2α (°)	$\frac{N_C}{F}$	2α (°)	
16825	3.18	25.4	1.608	20	0.435	180	-
16045	1.6	25.4	1.271	20	0.437	180	23.4
16831	3.18	38.1	1.096	30	0.362	5	38.9

From table 4.**1**, it can be seen that profiles 16045 and 16825 attained their maximum N_C/F values at $2\alpha = 20°$ and minimum at $2\alpha = 180°$, while the maximum and minimum N_C/F values for profile 16831 were attained at $2\alpha = 30°$ and $2\alpha = 5°$, respectively. This revealed that for channel profiles, dimension factors such as the change in section depth have an influence on the included angle at which the maximum and minimum axial compressive forces occur. Also, if the cross-sectional thickness is reduced by half, from profile 16825 to 16045, the maximum axial compressive force may reduce by up to 23.4 percent. In the case whereby the web depth is increased by approximately 50 percent from profile 16825 to 16831, the maximum axial compressive may reduce by up to 38.9 percent. The significant differences between the N_C/F values noticed at included angle $2\alpha = 20°\ and\ 30°$ can be associated with the uniformly distributed axial compressive forces along the arch length as reported by Liu *et al.*'s (2017b) study.

In summary, the effects of change in web-flange thickness and section depth influence the magnitude of the axial compressive forces, but not the overall behaviour. Based on studies reported by Pi and Trahair (1996) and Liu *et al.* (2017b), one should expect a decrease on the LTB loads at $5° \leq 2\alpha \leq 50°$ due to the high axial compressive forces.

4.3.1.1.2 Axial compressive forces of arches developed at constant slender ratios

The impact of the slender ratios $S/r_x = 60$ and 90 on the axial compressive forces are investigated in this section. The results obtained are presented in figure 4.**8** as a variation of the dimensionless axial compressive force (N_C/F), at included angles (2α). As mentioned in Section 4.**3**, profile 16825 was selected to evaluate the slender ratio effects due to its mean cross-section properties when compared to those of profile 16045 and 16831.

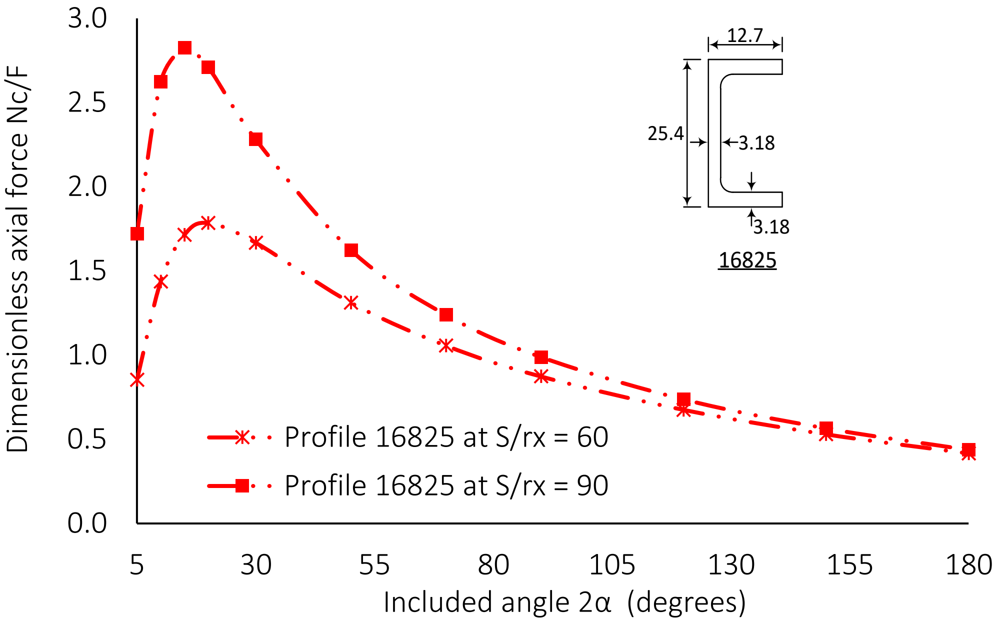

Figure 4.8 Variations in the axial compressive force due to changes in slender ratios

As illustrated in figure 4.**8**, the N_C/F values for both arches first increased to their peak values and then decreased, gradually, to their minimum values with the continued increase of the included angles. Also, it can be seen that the overall N_C/F magnitudes for arches developed at $S/r_x = 90$ are higher, compared to those developed at $S/r_x = 60$. The high N_C/F values were due to the long developed arc length, compared to the short arc length developed in arches modelled at $S/r_x = 60$ (Pi & Bradford 2003). The close variance observed at 2α > 120° was due to the profound differences in the span lengths between both slender ratios. That said, one should, generally, expect arches with an overall high elastic axial compressive forces influenced by their high slender ratios to have an overall low resistance to LTB as reported by Liu *et al.* (2017b) study. The maximum and minimum N_C/F values shown in figure 4.**8** are summarised in table 4.**2**. It should be noted that the $S/r_x = 90$ curve in this case was used as the point of reference due to its overall high N_C/F values.

Table 4.2 Maximum and minimum N_C/F values at their respective included angles and percentage difference for arches developed at constant slender ratios 60 and 90

Slender ratio S/r_x	Maximum $\frac{N_C}{F}$ and corresponding included angle 2α		Minimum $\frac{N_C}{F}$ and corresponding included angle 2α		Maximum $\frac{N_C}{F}$ percentage difference at corresponding included angle 2α in (%), *Ref:* $S/r_x = 90$
	$\frac{N_C}{F}$	2α (°)	$\frac{N_C}{F}$	2α (°)	
90	2.823	15	0.438	180	45.1
60	1.784	20	0.416	180	

From table 4.**2** it can be seen that the maximum N_C/F values for slender ratio 90 and 60 were attained at $2\alpha = 15° \text{ and } 20°$, respectively, with a percentage difference of 45.1 percent. This reveals two things. First, the slender ratio influences the included angle at which the maximum axial compressive force occurs but has an insignificant influence on the included angle of the minimum axial compressive force. Secondly, by decreasing the slender ratio by 50 percent, which was from 90 to 60, it may decrease the peak axial compressive force by up 45.1 percent for the same included angle. Again, this significant difference was associated with the long arc length, coupled with the effects of the included angles as observed by Pi, Bradford and Tong (2010).

That said, it was evident that the change in slender ratio does influence the magnitude of the axial compressive force, but not the general behaviour. Also, based on the axial compressive force influence on the LTB load for arches developed constant slender ratio, shallow arches will yield low resistance to LTB. Thus, they are not suitable for application in areas of high LTB. Furthermore, the N_C/F values across the included angles behaved similarly to those reported by Liu *et al.* (2017b).

4.3.1.2 Elastic central bending moments

Similar to the central axial compressive forces, this section presented the elastic bending moment at the crown of arches developed at constant span length (L) of 500 mm and those developed at constant slender ratios (S/r_x) of 60 and 90. Arches developed at $L = 500$ mm were used to examine the effects of the change in web-flange thickness and section depth on the bending moment behaviour and magnitude at different included angles. While arches developed at constant $S/r_x = 60$ and 90 were used to examine the effects of the slender ratio at different included angles on the bending moment. Contrary to an axially compressive force, an arch developed at a constant slender ratio with an overall high elastic bending moment is expected to have high resistance to LTB as observed in Liu *et al.*'s (2017b).

4.3.1.2.1 Bending moments of arches developed at constant span length

Similar to axial compressive forces, profiles 16045, 16825 and 16831, as described in table **3.1**, are used to evaluate the impact of change in web-flange thickness and section depth on the bending moment behaviour and magnitudes. Again, though the length of the arc (S) for all the three profiles were identical and corresponding included angles, their slender ratio varied due to their differences in radius of gyration (r_x). The results obtained from the arches developed from the three profiles at $L = 500$ mm are shown in figure 4.**9**. The results are presented as a variation of the dimensionless bending moment at the crown ($4M_C/FL$) against the included angle (2α).

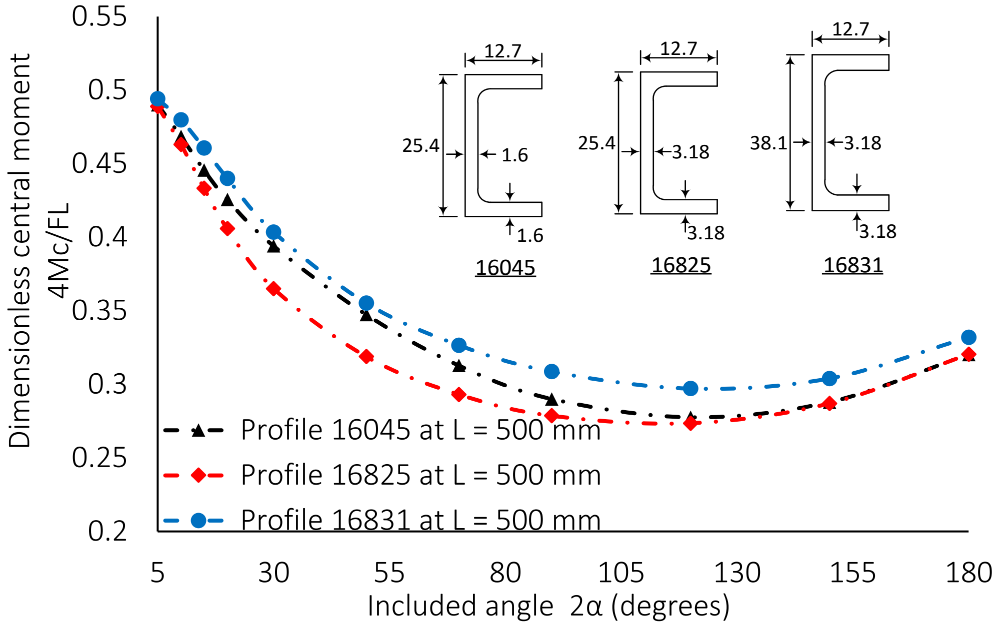

Figure 4.9 Variations in the central bending moment due to changes in channel sections

From figure 4.**9**, it can be seen that for all the profiles, the $4M_C/FL$ values first decreased to their minimum and then increased slightly with a continued increase of the included angles. With an overall high $4M_C/FL$ values for profile 16831, one should expect the profile to have more resistance to LTB, followed by profile 16045 and then 16825. This expectation, however, should be more valid for arches developed at the constant slender ratios as noticed in Liu *et al.* (2017b) research work. That said the overall high $4M_C/FL$ magnitude for profile 16831 was associated with the profile low centroid position from the shear centre, followed by profiles 16045 and 16825, respectively with a large distance between their centroid position and shear centre.

From reported studies, (Liu *et al.* 2017b), a general decrease in the bending moment increases the LTB load. However, the included angle at which the peak or least bending moment occurs cannot be associated with the included angle at which the minimum or maximum LTB loads will occur. Table 4.**3** summarises the different maximum and minimum $4M_C/FL$ values in figure 4.**9** along their respective included angles and percentage difference. Similarly, profile 16825 was used as the reference to determine the impact of the web-flange thickness and section depth on the bending moment.

Table 4.3 Maximum and minimum $4M_C/FL$ values at their respective included angles and percentage difference for arches developed at constant span length

<table>
<tr><th colspan="3">Profile description with dimensions in (mm)</th><th colspan="2">Maximum $4M_C/FL$ and corresponding included angle</th><th colspan="2">Minimum $4M_C/FL$ and corresponding included</th><th rowspan="2">Minimum $4M_C/FL$ percentage difference at corresponding included angle 2α in (%) Ref. 16825</th></tr>
<tr><th>Profile</th><th>Web & flange thickness</th><th>Section depth</th><th>$4M_C/FL$</th><th>2α (°)</th><th>$4M_C$ $/FL$</th><th>2α (°)</th></tr>
<tr><td>16825</td><td>3.18</td><td>25.4</td><td>0.489</td><td>5</td><td>0.274</td><td>120</td><td>-</td></tr>
<tr><td>16045</td><td>1.6</td><td>25.4</td><td>0.49</td><td>5</td><td>0.278</td><td>120</td><td>6.8</td></tr>
<tr><td>16831</td><td>3.18</td><td>38.1</td><td>0.494</td><td>5</td><td>0.297</td><td>120</td><td>8.2</td></tr>
</table>

From table 4.**3**, all three profiles attained their maximum and minimum $4M_C/FL$ values at $2\alpha = 5°$ and $120°$, respectively. These similarities implied that the position of the centroid from the shear centre had an insignificant influence on the included angles at which the maximum and minimum $4M_C/FL$ values occurred. Rather, the position of the centroid from the shear centre had a slight significant impact on the profiles bending moments magnitudes, as the profile web-flange thickness decreased by half, from profile 16825 to 16045, the maximum bending moment of profile 16825 increased by only 6.8 percent. On the other hand, when the section depth is increased by 50 percent, from profile 16825 to 16831, the maximum bending moment from profile 16825 only increased by 8.2 percent.

Again, it was noticed that the change in web-flange thickness and section depth influences the bending moments' magnitudes and not the general behaviour, since the general $4M_C/FL$ behaviour observed in Liu *et al.* (2017b) study on arches developed at constant slender ratios appeared to be similar to those shown in figure 4.**9**.

4.3.1.2.2 Bending moment of arches developed at constant slender ratios

Similar to axial compressive forces, profile 16825 was used to investigate the effects of slender ratio on the bending moments' behaviour and magnitudes of arches developed at constant slender ratios (S/r_x) of 60 and 90. The typical variation of the dimensionless bending moment at the crown ($4M_C/FL$) for arches developed at slender ratios $S/r_x = 60$ and 90 with included angles 2α are shown in figure 4.**10**.

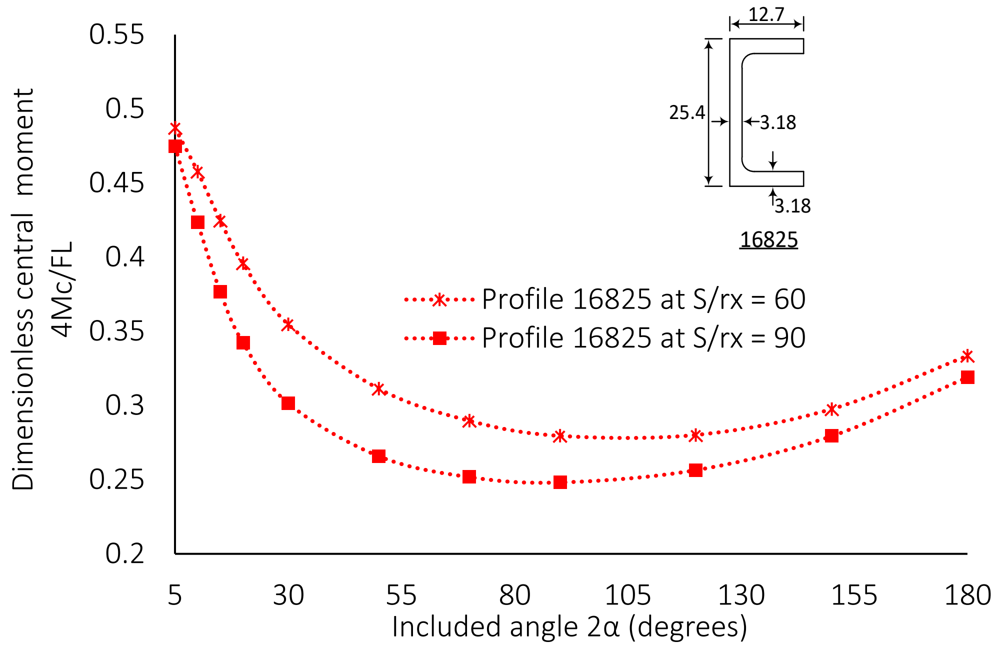

Figure 4.10 Variations in the central bending moment due to changes in slender ratios

It was noted in figure 4.**10** that the $4M_C/FL$ values for both slender ratios first decreased to their minimum values and then increased gradually with the continued increase of the included angle. Also, an overall high $4M_C/FL$ magnitude was observed for arches developed at $S/r_x = 60$. The overall high magnitudes for these arches were due to the short arc length developed that render them less slender; thus, highly resistive to bending, compared to arches with longer developed arc length developed at $S/r_x = 90$. For such arches with low slender ratios, one would expect more resistance to LTB, compared to those of higher slender ratios as observed in Liu *et al.* (2017b).

Like arches of constant span length, the points of maximum and minimum bending moments cannot be related to those of the LTB load. Even though the developed bending moments' are expected to influence the arches resistance against LTB as reported by Pi and Trahair (1996). Table 4.**4** summarised the maximum and minimum M_C/FL values at their respective included angles and percentage differences. The curve for arches developed at $S/r_x = 60$ as shown in figure 4.**10**, was used as the reference to determine the percentage difference due to their overall high M_C/FL values.

Table 4.4 Maximum and minimum $4M_C/FL$ values at their respective included angles and percentage difference for arches developed at constant slender ratios 60 and 90

Slender ratio S/r_x	Maximum $4M_C/FL$ and corresponding included angle 2α		Minimum $4M_C/FL$ and corresponding included angle 2α		Minimum $4M_C/FL$ percentage difference at corresponding included angle 2α in (%),
	$4M_C/FL$	2α (°)	$4M_C/FL$	2α (°)	
60	0.487	5	0.28	90	11.9
90	0.475	5	0.248	90	

It can be seen in table 4.**4** that both slender ratios attained their maximum and minimum $4M_C/FL$ values at $2\alpha = 5°$ and $90°$, respectively. The similar included angles for both maximum and minimum $4M_C/FL$ value, implied that the changed slender ratios did not influence the included angle at which the maximum or minimum $4M_C/FL$ occurred. Rather, by increasing the slender ratio by 50 percent, from 60 to 90 decreased the minimum $4M_C/FL$ value by 11.9 percent at the relative included angle. This occurrence further confirms that the change in slender ratios only influences the bending moment magnitudes and not the general behaviour. This is an indication that the critical buckling load resistance at slender ratio of 60 should be significantly greater than that at slender ratio of 90. This observation was similar to studies of Liu *et al.* (2017b) and Pi and Bradford (2003) on circular fixed arch arches subjected to point load.

4.3.2 Inelastic prebuckling analyses

Similar to elastic prebuckling, this section presented the inelastic prebuckling behaviour of arches developed at constant span length $L = 500$ mm and those at constant slender ratios $S/r_x = 60$ and 90. The main difference between the arches investigated in this section to those reported in Section 4.**3.1** was the added imperfections. In this study, the imperfections referred to the combined effects of the material nonlinearities, initial geometric imperfections and residual stresses as outlined in Section 3.**4.2.9**. Thus, the effects of imperfections on the magnitude and behaviour of prebuckling axial compressive force and bending moment at the crown are discussed henceforth.

4.3.2.1 The inelastic axial compressive force

The inelastic axial compressive forces investigated at the crown happened to be equal to those at the supports due to the symmetric loading. The axially compressive forces for arches developed at the constant span length are reported separately from those developed at constant slender ratios.

4.3.2.1.1 Axial compressive forces of arches developed at constant span length

The detailed cross-section profiles 16045, 16825 and 16831, as described in table 3.**1**, were used in this section to evaluate the impact of change in web-flange thickness and section depth on the inelastic axial compressive force behaviour and magnitudes. The arches were developed at $L = 500$ mm. The graph in figure 4.**11** presented a typical variation of the inelastic dimensionless axial compressive force at the crown (N_m/N_Y) at included angles (2α).

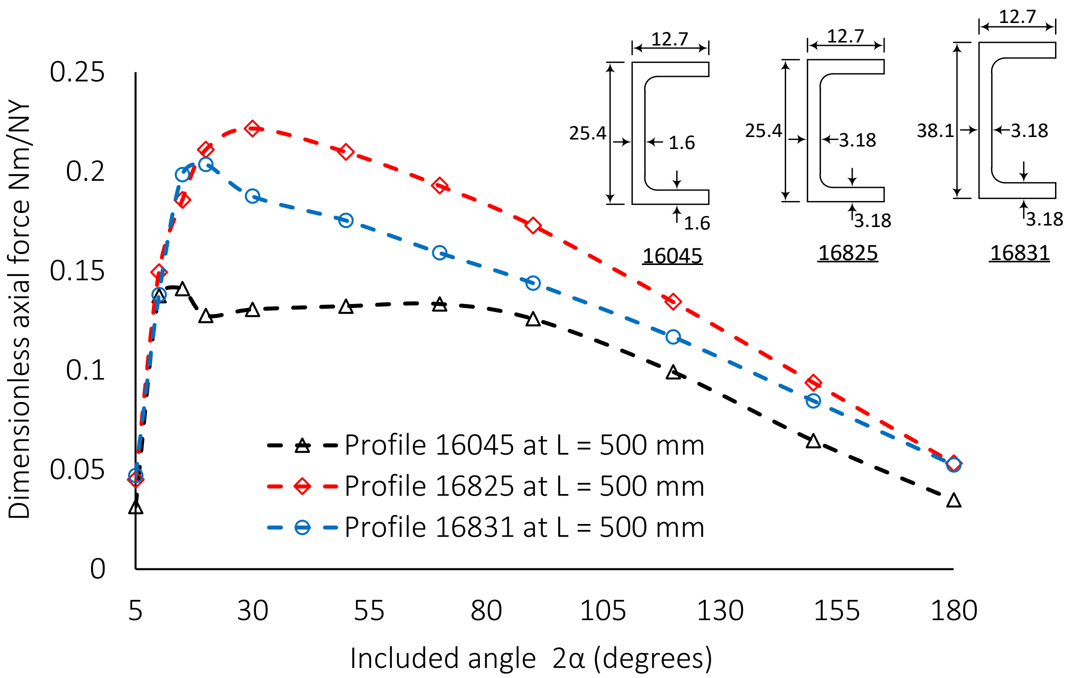

Figure 4.11 Variations in the axial compressive force due to changes in channel sections

As demonstrated in figure 4.**11**, all the cross-sections, the N_m/N_Y values increased drastically to some maximum values before decreasing with the continued increase in the included angle. In reference to profile 16825, the observed behaviour change of profile 16045 after its peak value was associated with the effect of the imperfection's sensitivity that developed high bending stresses at included angles $20° \leq 2\alpha \leq 30°$. From figure 4.**11**, it was realised that no cross-section dimensional property could be linked to the overall difference in N_m/N_Y magnitudes as was the case for the elastic analysis. Thus, their magnitudes where assumed to be related to the applied imperfections, coupled with the included angles effects.

Also, based on the inelastic axial compressive forces impacts on the LTB load, one would expect profile 16825 to have the most LTB load due to its overall high N_m/N_Y values (Pi & Bradford, 2003). However, this may not be the case for such arches, as their slender ratio is not constant. Thus, the torsion constant turns to have highly significant effects on the LTB load resistance. It should be noted that a decrease in the LTB load would still be expected at included angles $10° \leq 2\alpha \leq 30°$ for all three profiles due to the high inelastic axial compressive forces as reported in similar study by Pi and Trahair (1996). Nonetheless, the maximum and minimum N_m/N_Y values at corresponding included angles shown in figure 4.**11** are summarised in table 4.**5**. Profile 16825 curve was used as the reference curve due to its mean dimension properties as discussed in Section 4.**3**.

Table 4.5 Maximum and minimum N_m/N_Y values at their respective included angles and percentage difference for arches developed at constant span length

Profile description with dimensions in (mm)			Maximum N_m/N_Y and corresponding included angle		Minimum N_m/N_Y and corresponding included angle		Maximum N_m/N_Y percentage difference at corresponding included angle 2α in (%) *Ref. 16825*
Profile	Web & flange thickness	Section depth	N_m/N_Y	2α (°)	N_m/N_Y	2α (°)	
16825	3.18	25.4	0.221	30	0.045	5	-
16045	1.6	25.4	0.141	15	0.031	5	44.4
16831	3.18	38.1	0.203	20	0.047	5	8.8

It can be seen from table 4.**5** that all three profiles attained their maximum N_m/N_Y values at different included angles but the minimum N_m/N_Y values at $2\alpha = 5°$. Also, it was revealed that by decreasing the web-flange thickness by half, from profile 16825 to 16045 reduces the inelastic axial compressive force by 44.4 percent at a corresponding included angle. Meanwhile, an increase of the section depth by 50 percent, which is from profile 16825 to 16831, decreases the axial compressive force by only 8.8 percent at the corresponding included angle. Again, the axial compressive forces behaviours happened to be insignificantly influenced by the web-flange thickness and section depth, but rather the magnitudes. Thus, the N_m/N_Y overall behaviours happened to be similar to those reported for arches developed at constant slender ratio reported in Pi and Bradford (2003).

4.3.2.1.2 Axial compressive forces of arches developed at constant slender ratios

Like elastic axial compressive forces, profile 16825 was used to investigate the effects of the slender ratios on the inelastic axial compressive forces' behaviour and magnitudes. The investigated slender ratios (S/r_x) were 60 and 90. Typical variation of the inelastic dimensionless axial compressive forces at the crown (N_m/N_Y) at included angles (2α) are presented in figure 4.**12**.

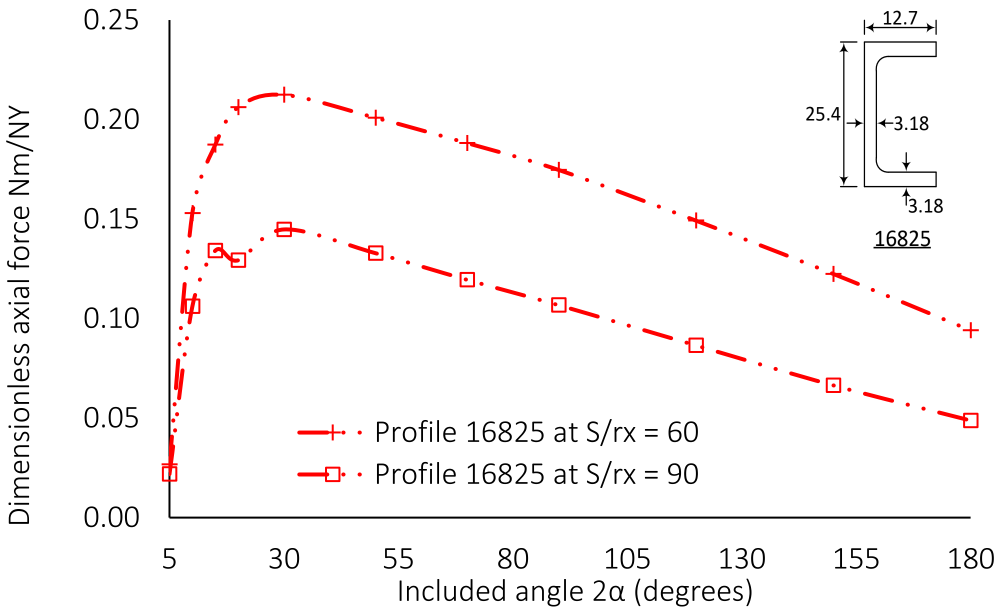

Figure 4.12 Variations in the axial compressive force due to changes in slender ratios

From figure 4.**12** it can be seen that with a continuous increase of the included angles, the N_m/N_Y values for arches developed at $S/r_x = 60$ increased to some peak values and then decreased continuously. While arches developed at $S/r_x = 90$, showed a similar behaviour with a small variance between $10° \leq 2\alpha \leq 30°$. The small variance of slight decrease and increase was associated with early yielding that occurred on a shallow slenderer arch coupled with the effect of the included angles. Unlike, the elastic prebuckling where an arch with an overall axial compressive force is expected to have the most resistance to LTB, the opposite is true for inelastic prebuckling, as reported by Pi and Bradford (2003). That said, one would expect a higher LTB load-carrying capacity for arches developed at $S/r_x = 60$ due to their overal high inelastic axial compressive force. Furthermore, at $2\alpha = 30°$, where the inelastic axial compressive forces are maximum, a decrease in the LTB load should be expected.

Table 4.**6** summarises the maximum and minimum N_m/N_Y values at their respective included angles as illustrated in figure 4.**12**. Also, the curve for arches developed at $S/r_x = 60$ was used as the reference curve to determine the percentage deviation due to its overall high N_m/N_Y values.

Table 4.6 Maximum and minimum N_m/N_Y values at their respective included angles and percentage difference for arches developed at the constant slender ratio of 60 and 90

Slender ratio S/r_x	Maximum N_m/N_Y and corresponding included angle 2α		Minimum N_m/N_Y and corresponding included angle 2α		Maximum N_m/N_Y percentage difference at corresponding included angle 2α in (%), *Ref:*
	N_m/N_Y	2α (°)	N_m/N_Y	2α (°)	
60	0.212	30	0.0267	5	37.5
90	0.145	30	0.0218	5	

From table 4.**6**, the maximum and minimum N_C/F values for both slender ratios occurred at $2\alpha = 30°\ and\ 5°$, respectively. These similarities implied that the included angle at which the maximum and minimum N_m/N_Y occurred was not influenced by the slender ratios. Moreover, the 37.5 percent difference between the maximum N_C/F value for arches developed at S/r_x = 60 and the corresponding value of slender ratio

90 indicated how much the inelastic axial compressive force magnitudes can be influenced by increase the slender ratio by 50 percent.

4.3.2.2 Inelastic bending moments

The inelastic bending moments at the crown M_m at included angles are reported in the same fashion to those of the elastic bending moments; that is, for arches developed at constant span length (L) of 500 mm and those developed at constant slender ratios (S/r_x) of 60 and 90. The obtained results were plotted with the dimensionless bending moment at the crown (M_m/M_P) as the ordinates and included angles (2α) as the abscissa.

4.3.2.3 Bending moments of arches developed at constant span length

Like the axial compressive force, profiles 16045, 16825, and 16831 are used in this section to evaluate the impact of change in web-flange thickness and web height on the inelastic bending moment behaviour and magnitudes. The arches were developed at constant span length of $L = 500$ mm. The graph in figure 4.**13** presented a typical variation of the inelastic dimensionless bending moment at the crown against the included angles (2α).

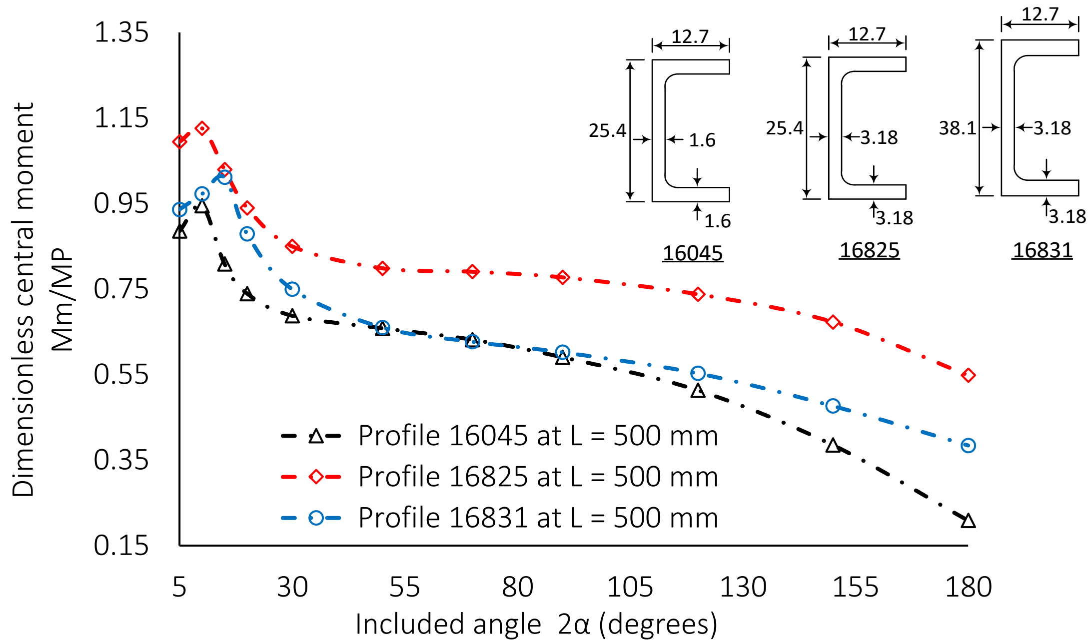

Figure 4.13 Variations in the central bending moment due to changes in channel sections

From figure 4.**13**, it can be seen that for all the profiles, as the included angles increased continuously, the M_m/M_P values first increased to their maxima and then decreased to their minimum values. The differences in M_m/M_P magnitudes noticed among the three profiles could not be directly linked to any of their cross-sections properties outlined in Hulamin Extrusions (2015) other than due to the influence of the imperfections coupled with the included angles. With an overall high M_m/M_P values for profile 16825, one would expect the profile to have more resistance to LTB, followed by profiles 16831 and 16045, in that order. This expectation, however, may vary for these arches developed at constant span length as other factors such as torsion constant differ for all three profiles. Nonetheless, an increase in the LTB load should be expected at $10° \leq 2\alpha \leq 15°$, where the inelastic bending moments increased to a maximum.

That said, the maximum and minimum M_m/M_P values at their respective included angles, as shown in figure 4.**13**, are presented in table 4.**7**. Profile 16825 curve was used as the point of reference to determine the percentage differences due to the profile mean dimensional properties, as discussed in Section 4.3.

Table 4.7 Maximum and minimum M_m/M_P values at their respective included angles and percentage difference for arches developed at constant span length

Profile description with dimensions in (mm)			Maximum M_m/M_P and corresponding included angle		Minimum M_m/M_P and corresponding included angle		Maximum M_m/M_P percentage difference at corresponding included angle 2α in (%) Ref.
Profile	Web & flange thickness	Section depth	M_m/M_P	2α (°)	M_m/M_P	2α (°)	
16825	3.18	25.4	1.125	10	0.548	180	-
16831	3.18	38.1	1.01	15	0.383	180	10.8
16045	1.6	25.4	0.945	10	0.208	180	17.5

From table 4.**7**, it can be seen that profile 16825 and 16045 attained their maximum M_m/M_P values at $2\alpha = 10°$, while profile 16831 maximum M_m/M_P value was attained at $2\alpha = 15°$. The difference in included angle for profile 16831 was associate with the low bending stress developed due to the profiles' large surface area. However, all three profiles minimum M_m/M_P values were attained at $2\alpha = 180°$. This occurrence was due to the high slender ratios for all three profiles, resulting in low bending stresses at the $180°$ included angles. Also, by decreasing the web-flange thickness by half, from profile 16825 to 16045 may decrease the maximum M_m/M_P value by 10.8 percent. On the other hand, increase of the section depth by 50 percent, from profile 16825 to 16831 may result in a 17.5 percent decrease of the maximum M_m/M_P value at the same included angles. In summary, the similarity in behaviour of the M_m/M_P values are shown figure 4.**13** indicates that the web-flange thickness and section depth have significant impacts on the bending moment magnitudes rather than the general behaviour.

4.3.2.3.1 Bending moments of arches developed at constant slender ratios

Similar to the axial compressive forces, profile 16825 was used to evaluate the effects of the slender ratios on the bending moment at the crown. The impact of slender ratios $S/r_x = 60$ and 90 on the inelastic bending moment at the crown (M_m) are presented in figure 4.**14**. The graph in figure 4.**14** was plotted as a variation of the dimensionless bending moment at the crown (M_m/M_P) at included angles (2α).

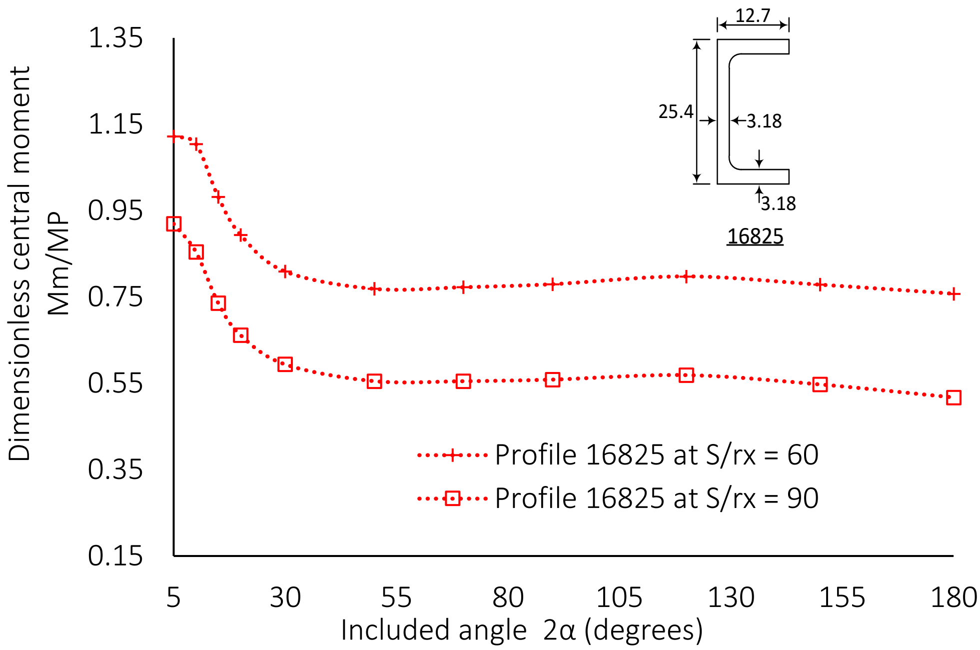

Figure 4.14 Variations in the central bending due to changes in slender ratios

It was observed in figure 4.**14** that for both slender ratios, the maximum M_m/M_P values first decreased significantly at $2\alpha = 5°$ to some values when $2\alpha = 30°$. From included angle $2\alpha > 30°$, the M_m/M_P values showed very insignificant decrease and increase change in magnitudes as the included angle increased. It was also observed that arches developed at $S/r_x =$ 60 had an overall high magnitude M_m/M_P values, compared to its counterparts modelled at $S/r_x = 90$. The high magnitudes for arches developed at $S/r_x =$ 60 was due to the developed short arc length that made the arches less slender that turns to have high resistance to bending. For such arches, the expected LTB load should be higher, as reported by Pi and Bradford, (2003) study.

Also, the maximum and minimum M_m/M_P values for both slender ratios were attained at $2\alpha = 5°$ and 180°. A maximum of 37.8 percent difference was noticed between the minimum M_m/M_P value for $S/r_x =$ 60 and the corresponding value for $S/r_x =$ 90 at 2α = 90°. This occurrence revealed that by increasing the slender ratio by 50 percent, the minimum inelastic bending moment at the crown would drop by 37.8 percent for the same included angle. Again, the change in slender ratio was noticed to have significant influence on the bending moment magnitude, compared to the general behaviour.

4.3.3 Comparison of the elastic and inelastic prebuckling results

The elastic and inelastic axial compressive forces and bending moments at the crown discussed in Section 4.3.1 and 4.3.2 for the channel profiles are compared in this section. The comparisons were designed such that elastic and inelastic axial compressive forces were reported separately from the elastic and inelastic bending moments. In each section, the arches were further grouped into those developed at the constant span length and those developed at the constant slender ratios. The main purpose of these comparisons was to evaluate the differences in behaviour and magnitudes of prebuckling caused by the applied imperfections.

4.3.3.1 Comparison of the elastic and inelastic axial compressive forces

The comparison of the elastic and inelastic axial compressive forces behaviours was examined for arches developed at the constant span length and those developed at constant slender ratios separately as follows:

Typical variation of the elastic and inelastic dimensionless axial compressive forces at respective included angles for arches developed at constant span length $L = 500$ mm are presented in figure 4.**15**.

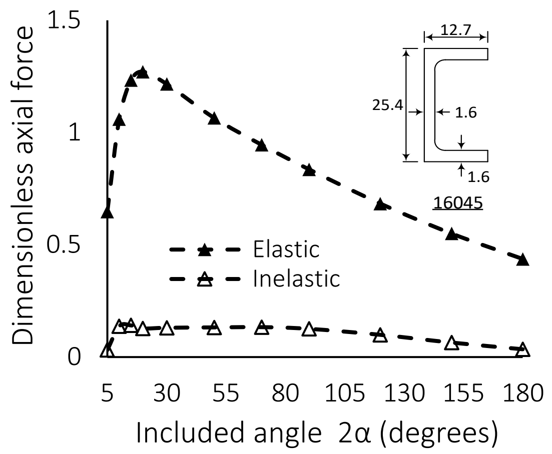

(a) Profile 16045 at $L = 500$ mm

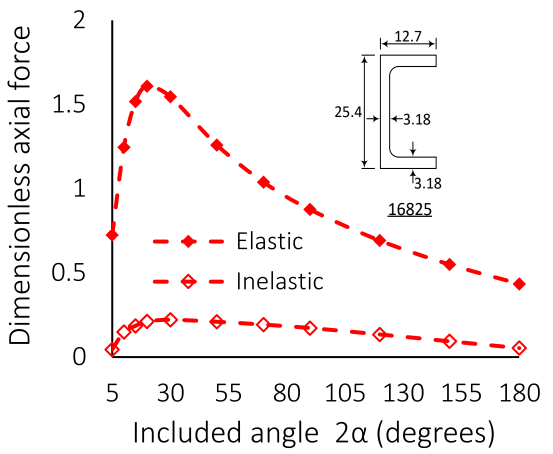

(b) Profile 16825 at $L = 500$ mm

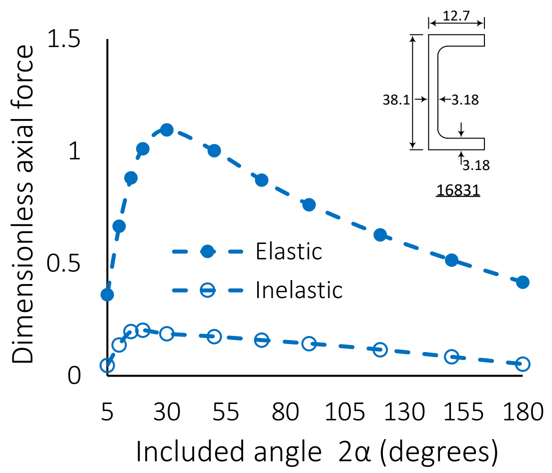

(c) Profile 16831 at $L = 500$ mm

Figure 4.15 Comparison between the elastic and inelastic variation in axial compressive force for constant span length arches.

From figure 4.**15**, it was noted that all the arches axial compressive forces first increased to peaks and then decreased with a continued increase of the included angles. However, the variation of the axial compressive forces with included angles for elastic analyses were more significant, compared to those of inelastic analyses. These differences in magnitudes were due to the imperfections. Based on the axial compressive force's influence on the LTB loads as reported by Pi and Bradford (2003), one would expect the inelastic LTB loads to be lower than the elastic LTB load due to their overall low axial compressive forces. In summary, the imperfections only influenced the magnitudes of the axial compressive forces and not their behaviours. Typical variation of the elastic and inelastic dimensionless axial compressive forces at respective included angles for arches developed at the constant slender ratios of 60 and 90, respectively, are shown in figure 4.**16**.

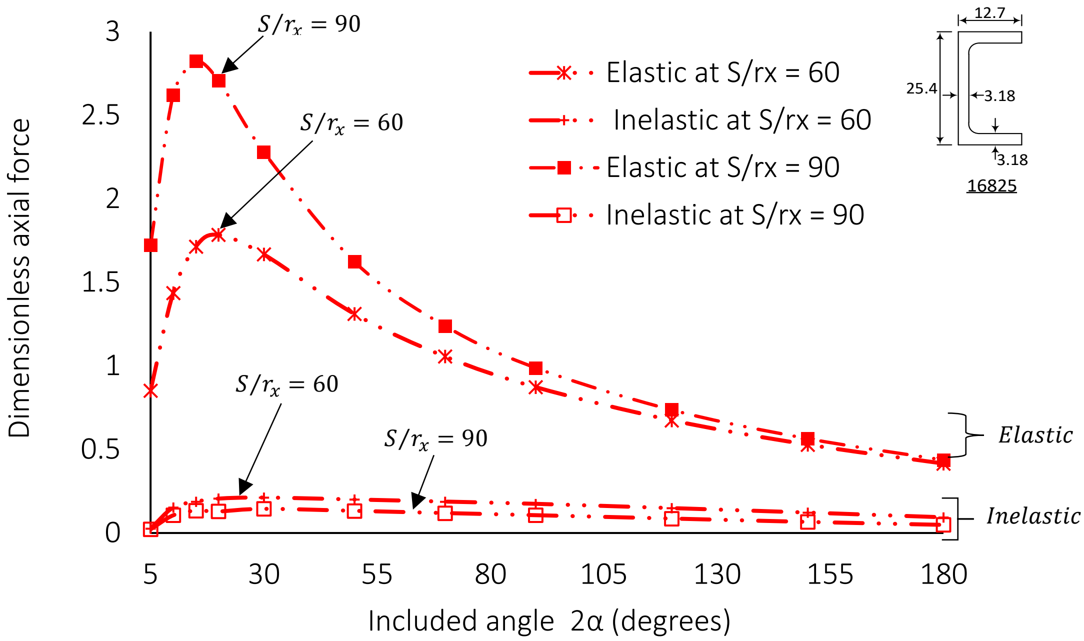

Figure 4.16 Comparison between the elastic and inelastic variation in axial compressive force for constant slender ratio arches

As illustrated in figure 4.**16**, all the arches axial compressive forces first increased to peak values and then decreased with the continued increase of the included angles. Both inelastic axial compressive forces showed slight changes in magnitudes, compared to those of elastic axial compressive forces. Also, it was noticed that the overall elastic axial compressive forces for arches developed at $S/r_x = 90$ were higher, while their inelastic axial compressive forces were lower. The exceedingly high magnitudes of the elastic axial compressive forces showed the influence of the applied imperfections in prebuckling that resulted in the overall low inelastic axial compressive forces for both slender ratios. Again, the imperfections influenced the magnitudes significantly, as compared to the behaviours since the inelastic and elastic patterns in axial compressive force patterns are alike.

4.3.3.2 Comparison of the elastic and inelastic bending moments

Similar to the axial compressive forces, this section presented a comparison of the elastic and inelastic bending moments for arches developed at constant span length and those developed at constant slender ratios as follows:

The variation of the elastic and inelastic dimensionless bending moments at the crown for arches developed at constant span length $L = 500$ mm at respective included angles are presented in figure 4.**17**.

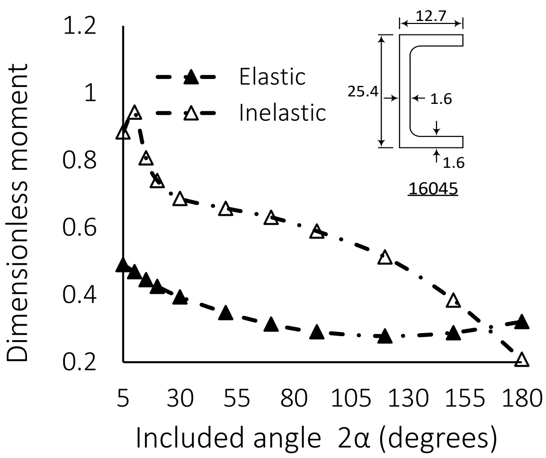

(a) Profile 16045 at L = 500mm

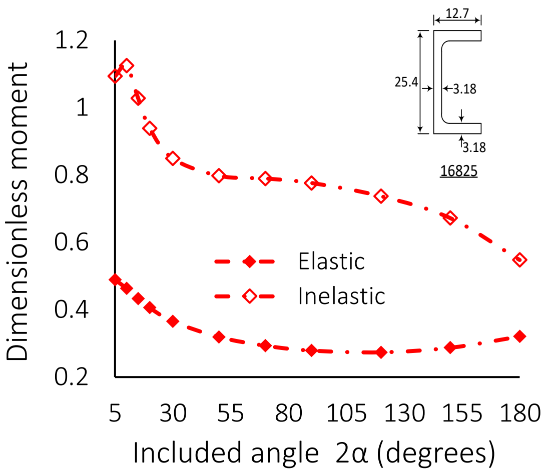

(b) Profile 16825 at L = 500mm

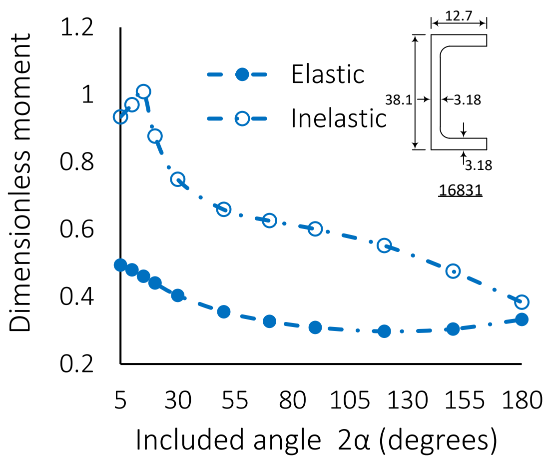

(c) Profile 16831 at L = 500mm

Figure 4.17 Comparison between the elastic and inelastic variation in bending moment for constant span length arches

It can be seen in figure 4.**17** that the elastic and inelastic general behaviour differs for most of the plots, as the elastic bending moments increased, the inelastic bending moments' decreases and vice versa. More significant differences were observed for very shallow arches, where the inelastic bending moment gradually increased while the elastic bending moment continued to decrease. Also, it was noticed that the overall elastic bending moments were lower, compared to their inelastic counterparts. The high magnitudes noticed for the inelastic bending moments indicated that the influence of imperfections due to the increase in the bending stresses along the flange edge caused by the applied imperfections. However, as the included angles increased, the increase of the bending stress by applied imperfections (in this case the residual stresses) started to reduce. As the bending stress decreased with increase in the included angle, a redistribution of the bending moment occurs and contributes insignificantly to the arch stiffness as seen at $2\alpha > 150°$ shown in figure 4.**17** (a). In summary, the imperfections were observed to have significant influence on the magnitudes and behaviour of the bending moments.

Typical variation of the elastic and inelastic dimensionless bending moments at the crown of arches developed at S/r_x = 60 and 90 at respective included angles presented in figure 4.**18**.

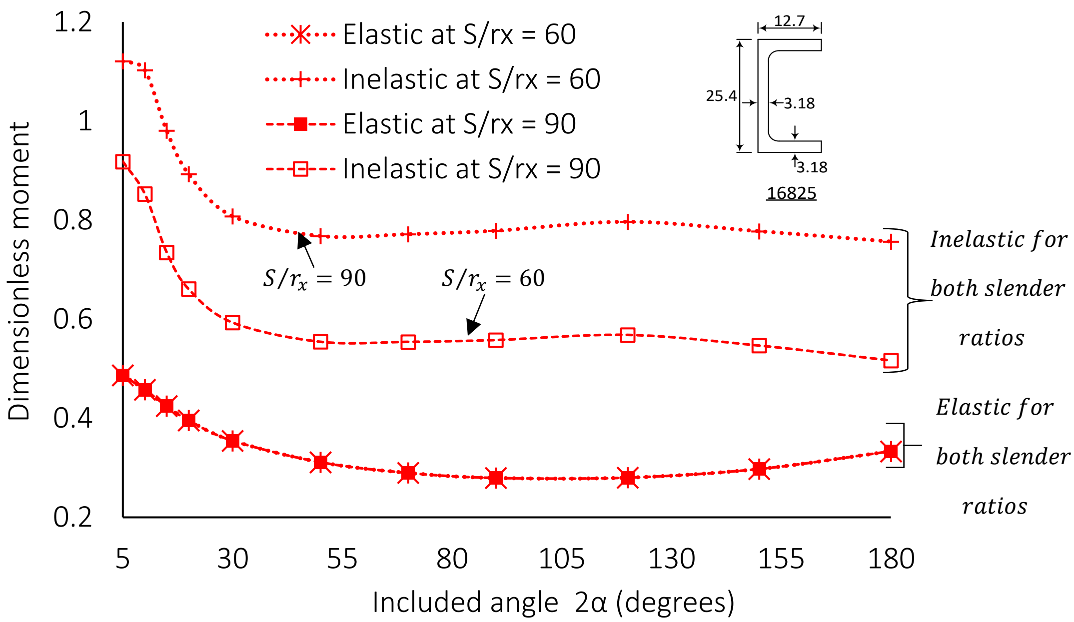

Figure 4. 18 Comparison between the elastic and inelastic variation in bending moment for constant slender ratio arches

It was observed from figure 4.**18** that for most of the included angles, both the elastic and inelastic bending moments behaved alike with a very slight variance between the elastic bending moments. The observed high inelastic bending moments for both slender ratios, compared to their elastic counterparts were due to the influence of the imperfections, because of the high bending stresses induced in the arch members. In addition, from the difference in magnitudes, the inelastic LTB loads for arches developed at $S/r_x = 60$ should be greater than those developed at $S/r_x = 90$ as observed in Pi and Bradford (2003). In summary, the change in slender ratios appeared to have significant impact on the bending moments' magnitude and slight influence on the general behaviour.

4.3.4 General discussion of elastic and inelastic prebuckling results

This section has presented the axial compressive forces and bending moments at the crown for freestanding circular fixed end's Al channel arches subjected to a transverse point load at the shear centre. The effects of the cross-sections change in web-flange thickness and section depth, slender ratios and imperfections on the axial compressive and bending actions at respective included angles were investigated. Further, comparisons between the elastic and inelastic axial compressive forces and bending moments, respectively, were made to examine the impact of the imperfections.

4.3.4.1 General discussion of elastic and inelastic axial compressive forces

The axial compressive forces obtained from the arches investigated revealed that for both elastic and inelastic analyses, the included angles had significant effects on the axial compressive force magnitudes. Also, it was observed that the effects were more significant on shallow arches between $15° \leq 2\alpha \leq 30°$ where the maximum axial compressive forces were attained. At these included angles, one would typically expect a decrease in the LTB resistance due to the high axial compressive forces that are expected to decrease the LTB load. Furthermore, it appeared that the centroid position from the shear centres was associated with the overall magnitudes of the elastic axial compressive forces for arches developed at constant span length. However, from the same three profiles, no dimensional properties could be related to the overall differences noticed for the inelastic axial compressive forces. Moreover, the overall low inelastic axial compressive forces, compared to their elastic counterparts, as shown in Section 4.3.3.1, clearly showed the effects of the imperfections on the axial compressive force magnitude.

For arches developed at constant slender ratios, it was revealed that the slender ratios, coupled with the included angles, significantly influenced the overall magnitudes for both the elastic and inelastic axial compressive forces. Arches developed at $S/r_x = 90$ happened to have an overall high elastic axial compressive force. Meanwhile, those developed at $S/r_x = 60$ happened to have an overall high inelastic axial compressive force. To the LTB loads, one should expect the arches developed at $S/r_x = 60$ to have more resistance to LTB due to their overall high inelastic axial compressive forces and vice versa. Also, the overall high elastic axial compressive forces imply that one should expect high elastic LTB loads compared to the inelastic LTB loads as observed by Pi and Bradford (2003).

4.3.4.2 General discussion of elastic and inelastic bending moments

The bending moments obtained from the arches investigated revealed that for both elastic and inelastic analyses, the included angles had significant effects on the bending moment's magnitudes. These effects were more significant for shallow arches at $2\alpha \leq 30°$ were the maximum bending moments were attained. For arches developed at constant span lengths, it was realised that the dimensional properties of the three profiles could not be related to individual profile overall elastic and inelastic bending moment magnitudes. Nonetheless, the overall high inelastic bending moments, as shown in Section 4.4.3.2.1 indicates the influence of the imperfections. These overall high magnitudes implied that one should expect a lower LTB resistance for such inelastic arches.

For arches developed at contact slender ratios, the elastic and inelastic behaviour were similar but different in magnitudes. The significant differences in magnitudes were due to the difference in slender ratios coupled with the effects of the included angles. For both elastic and inelastic bending moments, arches developed at $S/r_x = 60$ were noticed to have overall high bending moments magnitudes, compared to those developed at $S/r_x = 90$. These overall high magnitudes indicated that one should expect such arches to have high resistance to LTB buckling. However, by comparison of the elastic and inelastic bending moments, the overall high inelastic bending moments for both slender ratios, as discussed in Section 4.3.3.1, indicates low LTB resistance for inelastic analyses.

4.4 Elastic and Inelastic effects on factors that influence the LTB load

As mentioned in the reviewed literature, several factors influence the LTB load-carrying capacity on freestanding circular arches in general. The effects of the change in web-flange thickness and section depth, slender ratios and imperfections on the out-of-plane LTB stability in terms of load-carrying capacity are investigated in this section. The studied loads are the elastic critical buckling load F_{cr} and ultimate buckling load F_{ult}.

The arches developed at constant span length (L) were used to investigate the effects of the change in web-flange thickness and section depth on the LTB loads at respective included angles. On the other hand, archers developed at constant slender ratio (S/r_x) were used to investigate the effects of the slender ratios on the LTB loads at respective included angles. In addition, the imperfections were used to investigate by how much the elastic LTB loads over or underestimate the inelastic LTB loads at respective included angles. It is important to note that, in this study, the critical elastic buckling load (F_{cr}) was also referred to as the elastic LTB load or the ideal LTB load, while the ultimate buckling load (F_{ult}) was also referred to as the inelastic LTB load or the real LTB load.

4.4.1 Elastic effects on the lateral-torsional buckling load-carrying capacity

For elastic analyses on the out-of-plane LTB load, only the effects of the cross-sections (in web-flange thickness and section depth) and slender ratios at respective included angles were investigated with respect to the included angles. Hence, the elastic critical buckling loads obtained from arches developed at constant span length $L = 500$ mm and those obtained from arches developed at constant slender ratios $S/r_x = 60$ and 90 are presented in this section.

4.4.1.1 Effects of change in cross-sections on elastic lateral-torsional buckling loads of arches developed at constant span length

Previous studies in the reviewed literature indicated that the change in cross-sectional area for the same profiles such as an I-section might have significant effects on the elastic buckling load on freestanding circular fixed end arches subjected to central concentrated load. For this reason, similar effects were expected for the channel profiles investigated in this study with a change in web-flange thickness and section depth.

The effects of change in web-flange thickness and section depth on the elastic LTB loads (F_{cr}) are plotted against the respective included angles (2α) as shown in figure 4.**19**. The change in web-flange thickness was represented by profile 16825 and 16045, while profile 16825 and 16831 represented the change in section depth. The investigated arches were developed at $L = 500$ mm.

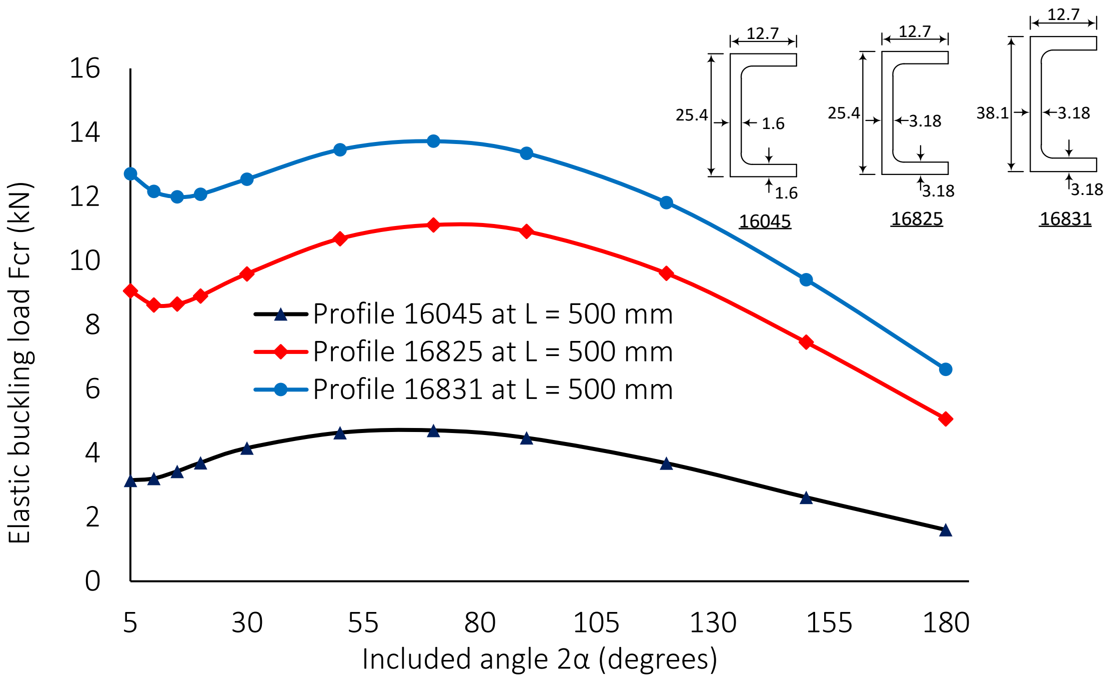

Figure 4.19 Effects of change in channel profile web-flange thickness and section depth on the elastic lateral-torsional buckling load for fixed arches

It can be observed in figure 4.**19** that as the included angles increased continuously, profile 16825 and 16831 F_{cr} values first decreased slightly to some values and then increased to a maximum value before decreased to their minimum at $2\alpha = 180°$. For profile 16045, the magnitudes F_{cr} first increased before decreasing gradually with the continued increase of the included angles. These behaviours can be related to the combined actions of the axial compressive forces and bending moments. Where an increase in axial compressive forces causes a decrease in the elastic LTB loads, while a decrease in the bending moments causes an increase in the elastic LTB loads.

Also, it was revealed from figure 4.**19** that profile 16831 has an overall high LTB load-carrying capacity followed by profile 16825 and 16045, respectively. These overall magnitudes are associated with the profiles torsion constant with profile 16831 having the highest value as outlined in Hulamin Extrusions (2015). Looking at the effects of the change in web-flange thickness and section depth, Table 4.8 summarised the maximum and minimum F_{cr} values at their respective included angles and the percentage differences. That said, it is worthy to note that the curve of profile 16825 shown in figure 4.**19** was used as the point of reference to determine the difference in percentages.

Table 4.8 Maximum and minimum F_{cr} values at their respective included angles and percentage difference for arches developed at constant span length

Profile description with dimension in (mm)			Maximum F_{cr} and relative included angle 2α		Minimum F_{cr} and relative included angle 2α		Maximum F_{cr} percentage difference at relative included angle 2α in (%) *Ref. 16825*	Maximum percentage difference and relative included angle 2α	
Profile	Web & flange thickness	Section depth	F_{cr} in kN	2α in (°)	F_{cr} in kN	2α in (°)		2α in (°)	(%)
16825	3.18	25.4	11.116	70	5.069	180	-	-	-
16045	1.6	25.4	4.709	70	1.605	180	81	180	103.8
16831	3.18	38.1	13.728	70	6.615	180	21	10	34.1

From table 4.**8**, if the section depth is increased by 50 percent, from profile 16825 to 16831 the maximum LTB load would rise by 21 percent for the same included angle. For the same profiles (16825 and 16831), the maximum increase in LTB load at corresponding included angle would be 34.1 percent. On the other hand, if the web-flange thickness is decreased by half, from profile 16825 to 16045, the LTB load would drop by 81 percent. Nevertheless, the maximum drop in the LTB loads would be up to 103.8 percent for the same angle. Additionally, it was revealed that channel arches developed at constant span length would have their most resistance to LTB at $2\alpha = 70°$. While the least resistance to LTB would be produced by arches developed at $2\alpha = 180°$. In summary, the change in cross-section dimension property significantly influenced the magnitudes of the LTB loads and not the overall behaviour across the included angles.

4.4.1.2 Effects of change in slender ratios on elastic lateral-torsional buckling loads of arches developed at the constant slender ratios

By used of profiles 16825, the effects of the slender ratios $S/r_x = 60$ and 90 on the elastic critical buckling load (F_{cr}) at included angles (2α) are presented in figure 4.**20**.

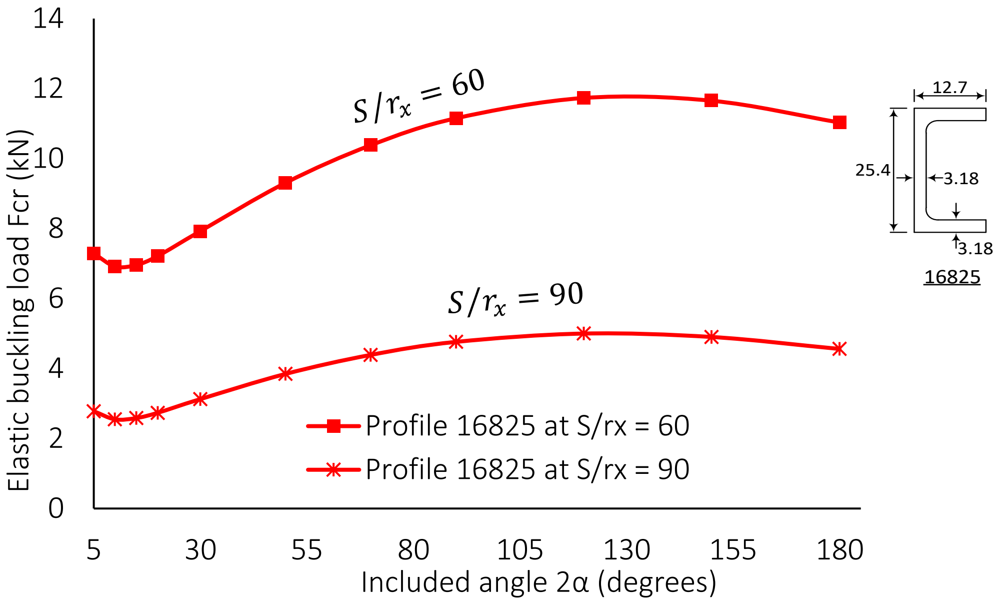

Figure 4.20 Slender ratios effects on the elastic lateral-torsional buckling load for fixed arches

It can be noted in figure 4.**20** that as the included angles increased continuously, the elastic LTB loads (F_{cr}) for both slender ratios first decreased slightly to their minimum, then increased to their maximum values before slightly decreased again. The F_{cr} magnitudes and behaviours were related to those of the axial compressive forces and bending moments discussed in Section 4.3.1. As expected, the arches developed at $S/r_x = 60$ with overall low elastic axial compressive forces and the most overall bending moment turned to have the highest LTB loads. The maximum and minimum F_{cr} values at corresponding included angles are summarised in table 4.**9**. It is important to note that the curve developed at $S/r_x = 60$ was used as the point of reference to determine the difference in percentage due to their overall high F_{cr} magnitudes.

Table 4.9 Maximum and minimum F_{cr} values at their respective included angles and percentage difference of arches developed at constant span length

Slender ratios (S/r_x)	Maximum F_{cr} and relative included angle 2α		Minimum F_{cr} and relative included angle 2α		Maximum F_{cr} percentage difference at relative included angle 2α in (%) *Ref.* $S/r_x = 60$	Maximum percentage difference and relative included angle 2α *Ref.* $S/r_x = 60$	
	F_{cr} in kN	2α in (°)	F_{cr} in kN	2α in (°)		2α in (°)	(%)
60	11.731	120	6.915	10	-	-	-
90	4.999	120	2.548	10	80.5	10	92.3

As illustrated in table 4.**9**, if the slender ratio is increased by 50 percent, from 60 to 90 the maximum LTB load would drop by 80.5 percent for the same included angle. However, for the same increase of the slender ratio, one should expect up to 92.3 percent drop of the LTB load at included angle $2\alpha = 10°$. These occurrences are is due to the high bending stresses on the compressive flange edge on shallow arches. Furthermore, it was revealed that for arches developed at constant slender ratios, the $120°$ included angle would be more suitable for application in the area of high LTB due to the maximum LTB load noticed at the included angle. On the other hand, the $10°$ included angle would provide the least resistance to LTB.

In summary, the change in the slender ratio significantly influences the LTB magnitudes and not the overall behaviour across the included angles. This occurrence conforms to a similar study reported in Liu *et al.* (2017b).

4.4.2 Inelastic effects on the lateral-torsional buckling load-carrying capacity

The reporting of the results and discussion in this section is identical to that of elastic analyses. The effects of the change in web-flange thickness and section depth and slender ratios on the ultimate buckling load (F_{ult}) are investigated in this section. The imperfections parameters used in the GMNIA were as follows:

i. Material nonlinearity that assumed the bilinear law
ii. The initial geometric imperfection of S/1000 as recommended in Spoorenberg, (2011) PhD research work.
iii. Residual stress patterns recommended by Wesley (2017) with provided force equilibrium in the arches

Likewise, the first section presented the effects of the change in web-flange thickness and section depth on the inelastic LTB loads for arches developed at constant span length at respective included angles 2α. Analogously, the next section presented the effects of slender ratios at respective included angles on the inelastic LTB load for arches developed at constant slender ratios.

4.4.2.1 Effects of cross-section dimensions on inelastic lateral-torsional buckling loads of arches developed at constant span length

Similar to the elastic analyses, arches developed at the constant span length $L = 500$ mm were used to investigate the behaviour and effects of the change in web-flange thickness and section depth on the ultimate buckling load F_{ult}. A typical variation of the F_{ult} values at included angles 2α are presented in figure 4.**21**. It is important to remember that profiles 16045, 16825 and 16831, as described in table 3.**1** of Chapter 3 were used.

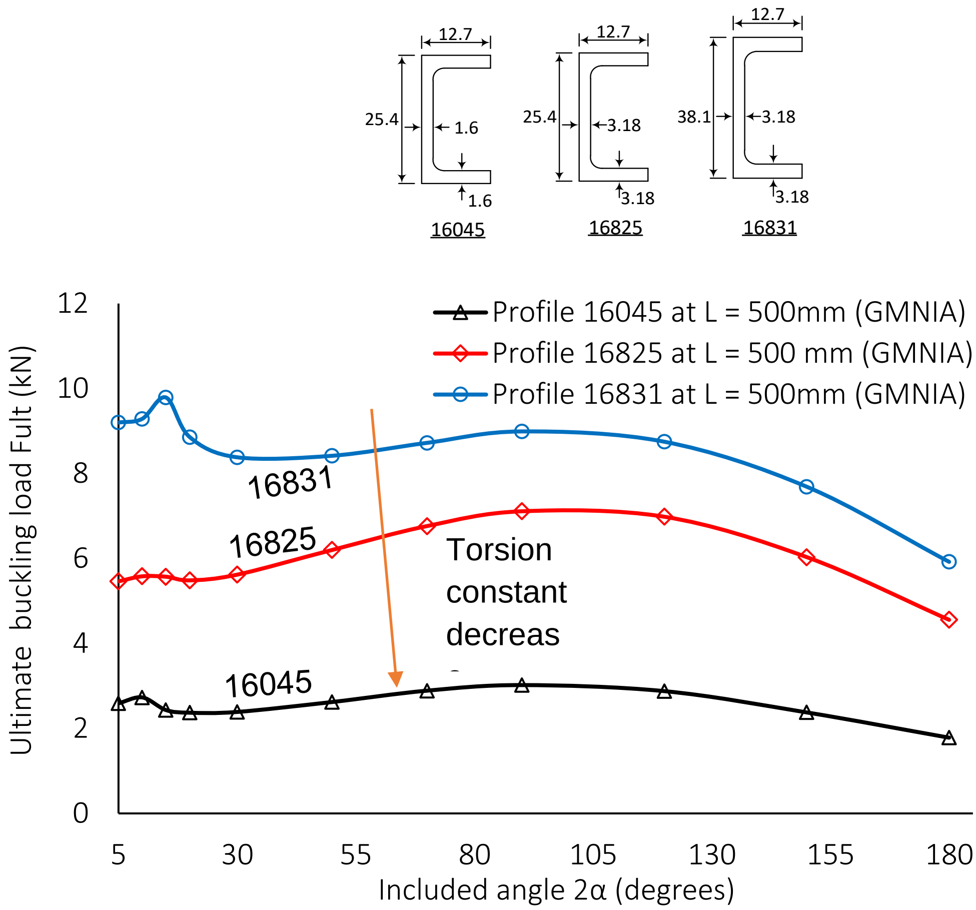

Figure 4.21 Cross-sectional effects on the inelastic lateral-torsional buckling load for fixed arches

As illustrated in figure 4.**21**, all the F_{ult} values first increased, then slightly decreased, before increased again and finally decreased gradually with the continued increased of the included angles. These behaviours were associated with the effects of the axial compressive forces and bending moments discussed in section 4.3.2. On the other hand, the F_{ult} overall differences in magnitudes were as a result of the torsion constant outlined in Hulamin Extrusions (2015); that is, profile 16831 high torsion constant, provided its arches with the most resistance to LTB, making it more suitable for designs against LTB, followed by profile 16825 and 16045, respectively.

The maximum and minimum F_{ult} values at their respective included angles and maximum percentage differences of the three profiles are summarised in table 4.**10**. Also, it is worthy to note that the curve of profile 16825, as shown in figure 4.**21** was used as the reference, due to the profile mean dimensional properties, as discussed in Section 4.3.

Table 4.10 Maximum and minimum F_{ult} values at their respective included angles and percentage difference for arches developed at constant span length

Profile description with dimensions in (mm)			Maximum F_{ult} and relative included angle 2α		Minimum F_{ult} and relative included angle 2α		Maximum F_{ult} percentage difference at relative included angle 2α in (%) *Ref. 16825*	Maximum percentage difference and relative included angle 2α *Ref. 16825*	
Profile	Web & flange thickness	Section depth	F_{ult} in kN	2α in (°)	F_{ult} in kN	2α in (°)		2α in (°)	(%)
16825	3.18	25.4	7.111	90	4.556	180	-	-	-
16045	1.6	25.4	3.02	90	1.783	180	80.8	180	87.5
16831	3.18	38.1	9.788	15	5.921	180	31.7	15	54.9

As observed in table 4.**10**, for profiles of the same cross-section width, as the section depth is increased by 50 percent, from profile 16825 to 16831, the maximum LTB load would rise by 31.7 percent for the same included angle. For the same profiles, the maximum increase in LTB load at a corresponding included angle would be up to 54.9 percent. In the case where the web-flange thickness is decreased by half, from profile 16825 to 16045, the LTB load would drop by up to 80.8 percent. For the same decrease in thickness, the LTB load would be up to 87.5 percent at $180°$ included angle. Nonetheless, it was revealed that for arches with section depth to width ratio of 2, profile 16825 and 16045, the $90°$ included angle would be ideal for designing against LTB for such arches. However, when the section depth to width ratio is 3, profile 16831, the $15°$ included angle becomes more suitable. Nevertheless, the $180°$ included angles stayed the least suitable for LTB designs for arches of constant span length due to their general low F_{ult} values for all three profiles. Again, the change in cross-section dimensions appeared to significantly influence the LTB load magnitudes, compared to the general behaviour across the included angles.

4.4.2.2 Effects of slender ratios on inelastic lateral-torsional buckling loads of arches developed at the constant slender ratios

Identical to the elastic analysis, profile 16825 was used in this section to investigate the effects of the slender ratios on the ultimate buckling loads (F_{ult}) at respective included angles for arches developed at constant slender ratios. That said, a typical variation of the F_{ult} obtained for arches developed at slender ratios S/r_x = 60 and 90 at respective included angles 2α are presented in figure 4.**22**.

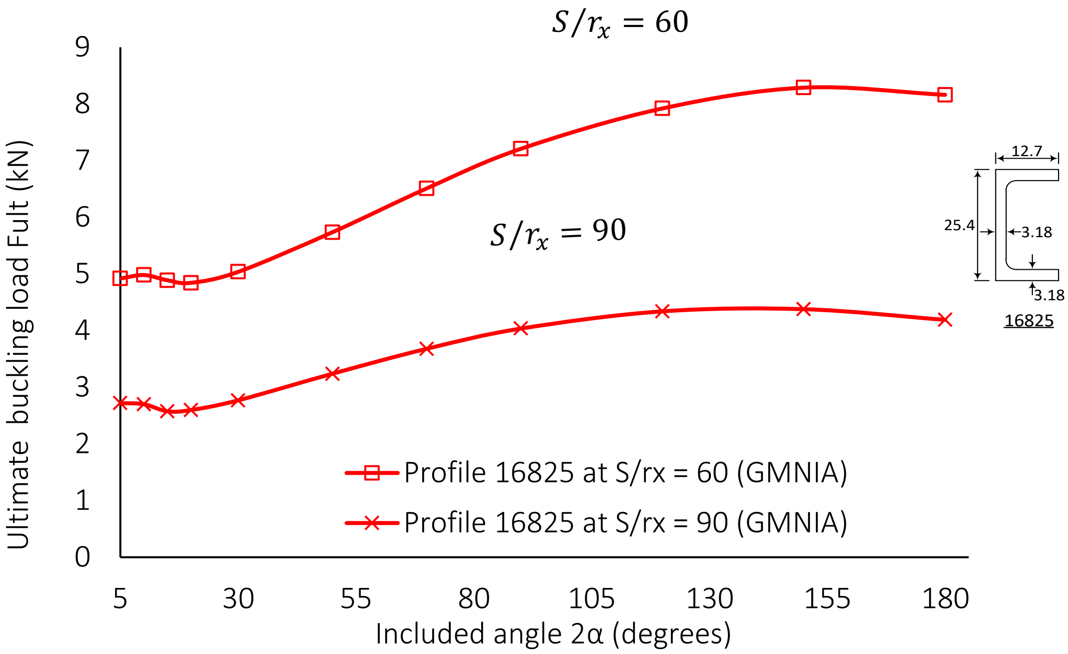

Figure 4.22 Slender ratios effects on the inelastic lateral-torsional buckling load for fixed arches

As demonstrated in figure 4.**22**, as the included angles increased continually, a general decreased of the F_{ult} values occurred before increased to the peak values with a very slight decrease after that. The observed behaviours and overall magnitudes were as anticipated from the effects the axial compressive forces and bending moments on the LTB loads discussed in 4.3.2. The overall high F_{ult} values for arches developed at $S/r_x = 60$ indicates that arches of lower slender ratios are more suitable in designs that require high LTB stability. That having been said, the maximum and minimum F_{ult} values at corresponding included angle together with their maximum percentage differences are summarised in table 4.**11**. Like the elastic analyses, the F_{ult} curve developed from arches modelled at $S/r_x = 60$ was used as the reference for measurement.

Table 4.11 Maximum and minimum values at their respective included angles and percentage difference for arches developed at constant slender ratios

Slender ratios (S/r_x)	Maximum F_{ult} and relative included angle 2α		Minimum F_{ult} and relative included angle 2α		Maximum F_{ult} percentage difference at relative included angle 2α in (%) *Ref.* $S/r_x = 60$	Maximum percentage difference and relative included angle 2α *Ref.* $S/r_x = 60$	
	F_{ult} in kN	2α in (°)	F_{ult} in kN	2α in (°)		2α in (°)	(%)
60	8.287	150	4.843	20	-	-	-
90	2.377	150	2.575	15	61.7	180	64.3

From table 4.**11**, if the slender ratio is increased by 50 percent, from 60 to 90 the maximum LTB load would drop by 61.7 percent for the same included angle. However, for the same increase of the slender ratio, one should expect a 64.3 percent drop of the LTB load at $180°$ included angle. Also, it was revealed that for arches developed at constant slender ratios, the $150°$ included angle would be more suitable for application in areas were high LTB are expected due to the included angle high resistance to LTB. On the other hand, the shallow arches at included angles $15° \leq 2\alpha \leq 20°$ are least favourable, due to their low resistance to LTB as seen with their low LTB loads. Again, the change in slender ratios is found to influence the LTB load magnitudes significantly, compared to the general behaviour across the included angles.

4.4.3 Comparison of elastic and inelastic lateral-torsional buckling loads

The elastic critical buckling loads (F_{cr}) and inelastic buckling loads (F_{ult}) discussed in section 4.4.1 and 4.4.2 are compared in this section. These comparisons are to better assimilate the impact of the imperfections on the LTB loads. For arches developed at constant span length, the elastic and inelastic LTB loads were compared for the distinctive profiles. The elastic and inelastic LTB loads obtained from profile 16045 were compared together to understand better the effects of applied imperfections on the profile LTB loads at respectively included angles. The same comparisons were made for arches developed at constant span length from profile 16825 and 16831. For arches developed at constant slender ratios, comparisons were also made between the elastic and inelastic LTB loads. Those obtained from the slender ratio of 60, were compared separately from those obtained at ratio 90. The above comparisons were used to indicate by how much the ideal analyses do, the elastic analyses under or overestimated to expected inelastic or real LTB loads.

It is important to note that the points of interest from the comparisons were the maximum and minimum LTB loads as typical in designs of the strength of a material. The curves used for measurements as references were those with an overall high LTB load-carrying capacity. The comparisons of the elastic and inelastic LTB loads of the arches developed at constant span length $L = 500$ mm is first presented, followed by those developed at the constant slender ratios of 60 and 90, respectively.

4.4.3.1 Comparison of the elastic and inelastic lateral-torsional buckling loads of arches developed at constant span length

The elastic and inelastic LTB loads compared in this section are for arches developed at the constant span length $L = 500$ mm. These include all three profiles 16045, 16825 and 16831. These comparisons are to provide detailed information on the effects of imperfections on the LTB loads of such arches.

4.4.3.1.1 Assessments on the effects of imperfections on the lateral-torsional buckling loads of arches developed from profile 16045 at constant span length

A typical comparison between the critical elastic buckling loads F_{cr} and ultimate buckling loads F_{ult} at included angles 2α for arches developed $L = 500$ mm from profile 16045 are presented in figure 4.**23**.

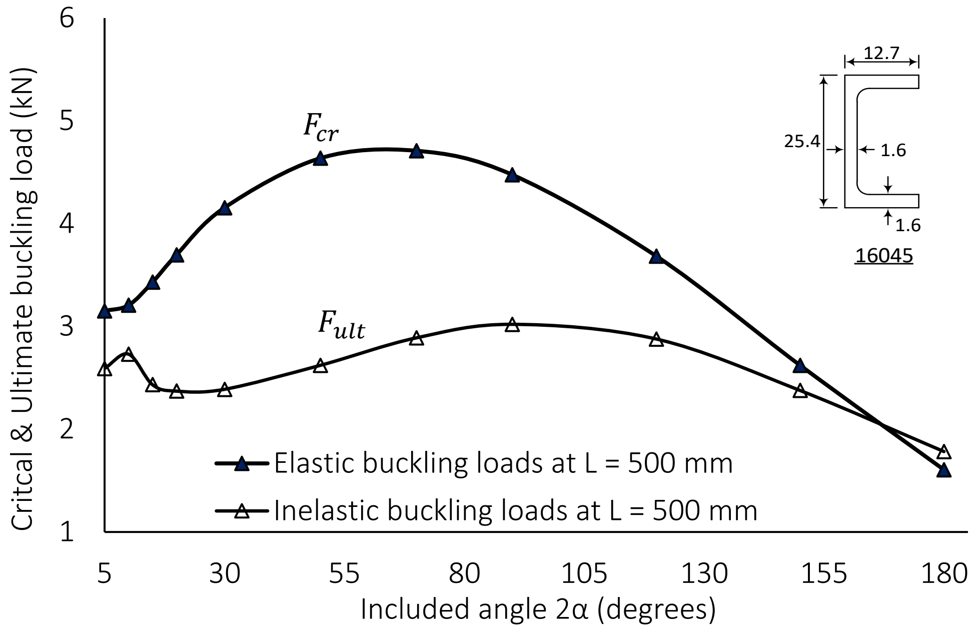

Figure 4.23 Comparison of the critical and ultimate lateral-torsional buckling loads for profile 16045

It can be seen in figure 4.**23** that at included angles $2\alpha > 30$, both the elastic and inelastic buckling loads increased to their maximums before they decreased. While at $5° < 2\alpha < 30°$ included angle, as the elastic buckling load increased continuously, its inelastic counterpart increased and decreased. The observed behaviours of the elastic and inelastic LTB loads were associated with the axial compressive forces and bending moments discussed in section 4.3.3; that is, the overall magnitudes of the elastic LTB loads can be attributed to the overall high magnitude of the elastic axial compressive forces in section 4.3.3.1 and the low elastic bending moments in Section 4.3.3.2 and vice versa. Besides, the point at which the $F_{cr} \leq F_{ult}$ was also associated with bending moments in Sections 4.3.3.2. Figure 4.**17** (a). Further, the overall high elastic LTB loads indicated the overestimation of the expected real LTB loads. The maximum and minimum LTB loads and their respective percentage differences are summarised in table 4.**12**. The curve of the elastic LTB loads was used as a reference for measurements due to its overall high elastic LTB loads.

Table 4.12 The maximum and minimum elastic and inelastic LTB loads differences in percentages for arches developed at constant span length from profile 16045

The percentage difference between the maximum elastic LTB load and the corresponding inelastic LTB load		The percentage difference between the minimum elastic LTB load and the corresponding inelastic LTB load		The maximum difference in percentage	
Included angle 2α in degree (°)	Percent (%)	Included angle 2α in degree (°)	Percent (%)	Included angle 2α in degree (°)	Percent (%)
70	47.9	180	-10.5	50	55.5

From table 4.**12**, by application of the imperfections, the maximum elastic LTB load overestimated the expected real LTB load by up to 47.9 percent at the relative included angle. However, it so happened that the highest by which the elastic LTB loads overestimated the real LTB load was up to 55.5 percent at $50°$ included angle. The negative percentage (-10.5 percent) indicated that at the $180°$ included angle where the lowest LTB loads occurred, the elastic buckling load underestimated the inelastic by 10.5 percent; that is, the negative sign represents an increase of the F_{ult} above the F_{cr}. In general, the elastic LTB were found to have overestimated the inelastic LTB buckling loads for all shallow and moderate arches, indicating the influence of imperfections on the LTB loads are less significant for deep arches.

4.4.3.1.2 Assessments on the effects of imperfections on the lateral-torsional buckling loads of arches developed from profile 16825 at constant span length

Similar to profile 16045, a typical comparison between the critical elastic buckling loads F_{cr} and ultimate buckling loads F_{ult} at the included angles 2α for arches developed from profile 16825 at the constant span length, $L = 500$ mm are presented in figure 4.**24**.

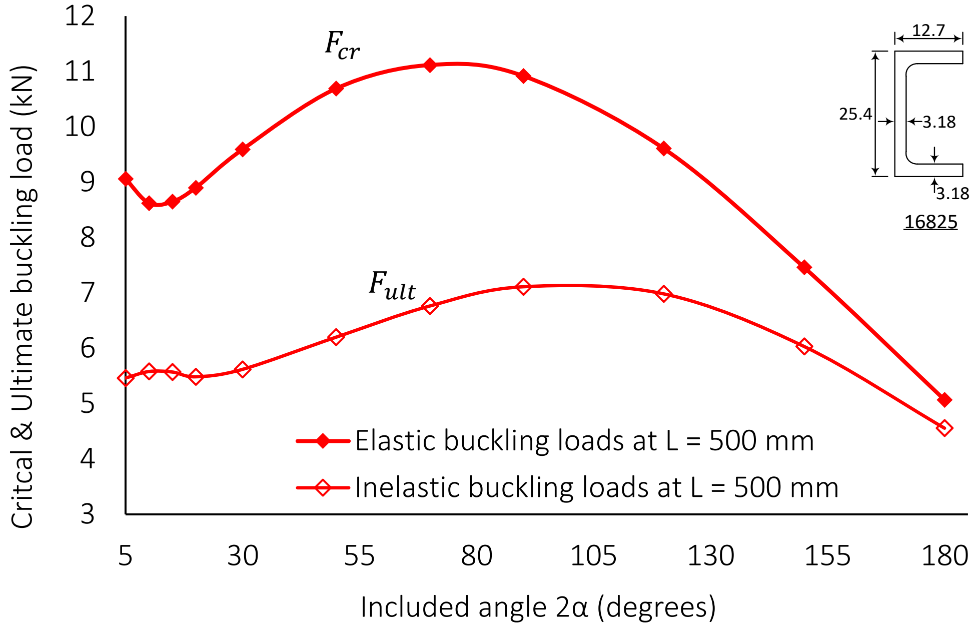

Figure 4.24 Comparison of the critical and ultimate lateral-torsional buckling loads for profile 16825

It can be seen in figure 4.**24** that for included angles $2\alpha < 20°$, the behaviours of the elastic and inelastic LTB loads are opposing each other similar to those reported for profile 16045. However, for included angles $2\alpha > 20°$, both elastic and inelastic LTB loads increased to their peak values they before decreased to their respective minimum values with the elastic LTB loads showing a more significant rate of decrease. These differences in behaviours were attributed to the combined axial compressive and bending actions on the LTB load discussed in sections 4.**4.1** and 4.**4.2**. Furthermore, the overall high elastic LTB loads revealed the overestimation of the expected real LTB loads. Therefore, the percentage difference between the maximum and minimum elastic and inelastic LTB loads are presented in table 4.**13**. Again, the elastic LTB loads plots, as shown in figure 4.**24**, was used as the reference for measurements.

Table 4.13 The maximum and minimum elastic and inelastic LTB loads differences in percentages for arches developed at constant span length from profile 16825

The percentage difference between the maximum elastic LTB load and the corresponding inelastic LTB load		The percentage difference between the minimum elastic LTB load and the corresponding inelastic LTB load		The maximum difference in percentage	
Included angle 2α in degree (°)	Percent (%)	Included angle 2α in degree (°)	Percent (%)	Included angle 2α in degree (°)	Percent (%)
70	48.7	180	10.6	50	53.1

From table 4.**13**, it was noted that by the introduction of imperfections, the maximum elastic LTB load overestimated the expected real buckling load by up to 48.7 percent at the corresponding included angle. Further, it happened that the maximum percentage by which the elastic LTB load overestimated the real buckling was up to 53.1 percent at 50° included angle. Furthermore, at the lowest LTB loads at 180° included angles, the elastic LTB load only overestimated the real LTB load by only 10.6 percent. These results indicated that the effects of imperfections on the LTB loads are more significant at included angles were high resistance to LTB are expected. Generally, on average the elastic LTB loads overestimated the inelastic LTB loads by up 40 percent. These differences indicated the effects of the applied imperfections on the LTB load-carrying capacity.

4.4.3.1.3 Assessments on the effects of imperfections on the lateral-torsional buckling loads of arches developed from profile 16831 at constant span length

A typical comparison between the critical elastic buckling loads F_{cr} and ultimate buckling loads F_{ult}at included angles 2α for arches developed from profile 16831 at the constant span length $L = 500$ mm are presented in figure 4.**25**.

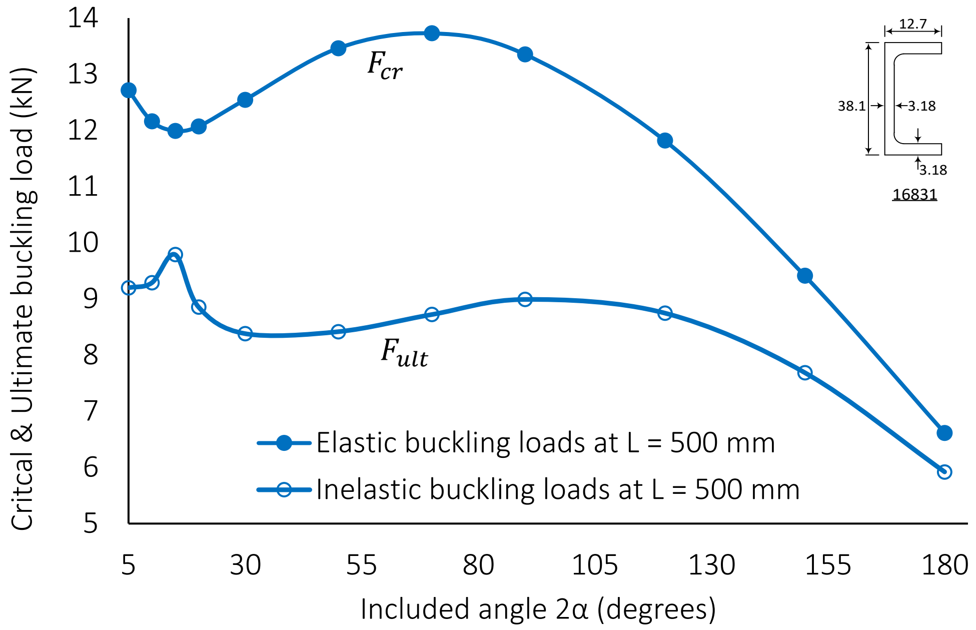

Figure 4.25 Comparison of the critical and ultimate lateral-torsional buckling loads for profile 16831

It can be seen in figure 4.**25** that at included angle $2\alpha < 30°$, the elastic and inelastic LTB loads behaved in an opposite manner, such as those reported for profiles 16825 and 16045; as the elastic LTB loads decreased, the inelastic LTB loads increased and vice versa. Furthermore, at $2\alpha > 30°$, both LTB loads increased to some maximum values before decreasing to their minimum values with significant decreasing rate noticed for the elastic LTB loads. These behaviours resulted from the combined axial compressive and bending actions on the LTB loads, as discussed in Sections 4.**4.1** and 4.**4.2**. For the high elastic LTB loads, it is evident that the applied imperfections had significant effects on the LTB loads at all included angles. Table 4.**14** summarises the percentage difference between the maximum and minimum elastic and inelastic LTB loads, respectively. Due to the overall high elastic LTB load, its curve as shown in figure 4.**25** was used as the reference for measurement.

Table 4.14 The maximum and minimum elastic and inelastic LTB loads differences in percentages for arches developed at constant span length from profile 16831

The percentage difference between the maximum elastic LTB load and the corresponding inelastic LTB load		The percentage difference between the minimum elastic LTB load and the corresponding inelastic LTB load		The maximum difference in percentage	
Included angle 2α in degree (°)	Percent (%)	Included angle 2α in degree (°)	Percent (%)	Included angle 2α in degree (°)	Percent (%)
70	44.6	180	10.6	70	44.6

From table 4.**14**, it was observed that having applied the imperfections, the maximum elastic LTB load overestimated real LTB load by up to 44.6 percent at the relative included angle. The 44.6 percent at 70° included angle happens to be the maximum percentage difference across the included angles. This occurrence indicated that the maximum impact of the applied imperfections occurred at 70° included angle. Also, at the lowest LTB loads, the least percentage difference of 11.1 percent was observed between the elastic and inelastic LTB loads. Again, this occurrence indicated that the lowest impact of the applied imperfections on the LTB loads occurred at 180° included angle. On average, the elastic LTB loads were noticed to have overestimated the supposed real LTB load by up to 40 percent.

4.4.3.2 Comparison of the elastic and inelastic lateral-torsional buckling loads of arches developed at the constant slender ratios of 60 and 90

The elastic and inelastic LTB loads compared in this section are those discussed in Sections 4.4.1.2 and 4.4.2.2, respectively. These arches were developed at constant slender ratios $S/r_x = 60\ and$ 90 from profile 16825.

4.4.3.2.1 Assessments on the effects of imperfections on the lateral-torsional buckling loads of arches developed from profile 16825 at constant slender ratio 60

A typical comparison between the critical elastic buckling loads F_{cr} and ultimate buckling loads F_{ult} at included angles 2α of arches developed at $S/r_x = 60$ from profile 16825, are presented in figure 4.**26**.

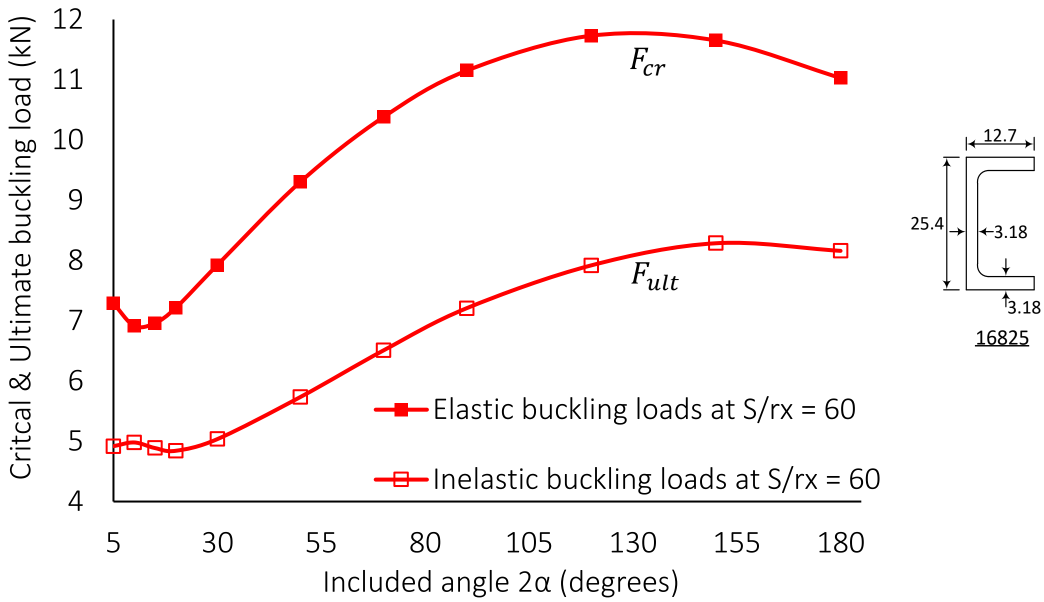

Figure 4.26 Comparison of the critical and ultimate lateral-torsional buckling loads for profile 16825 developed at slender ratio 60

It can be seen in figure 4.**26** that at included angles $2\alpha \leq 20°$, as the elastic LTB loads decreased, its inelastic counterpart increased and vice versa. However, at $2\alpha > 20°$ both the elastic and inelastic LTB loads increased to their peaks and decreased slightly after that. These differences in behaviour were associated with the combined axial compressive and bending actions on the LTB loads discussed in Sections 4.**4.1** and 4.**4.2**. The overall low magnitude noticed for the inelastic LTB loads were reflections of the effects by the applied imperfections on the LTB loads. These imperfections, such as the geometric imperfection and residual stresses, cause initial low and high bending stress, respectively.

Further, the results revealed that the elastic LTB loads overestimated the expected real LTB loads. The percentage difference between the maximum and minimum elastic and inelastic LTB loads, respectively, are summarised in table 4.**15**. It is important to note that the curve of the elastic LTB loads shown in figure 4.**26** were used as the reference for measurements due to its overall high LTB loads.

Table 4.15 The maximum and minimum elastic and inelastic LTB loads differences in percentages for arches developed at constant slender ratio 60 from profile 16825

The percentage difference between the maximum elastic LTB load and the corresponding inelastic LTB load		The percentage difference between the minimum elastic LTB load and the corresponding inelastic LTB load		The maximum difference in percentage	
Included angle 2α in degree (°)	Percent (%)	Included angle 2α in degree (°)	Percent (%)	Included angle 2α in degree (°)	Percent (%)
120	38.8	180	29.9	50	47.5

As observed in table 4.**15**, by application of the imperfections, the maximum elastic LTB load overestimated real LTB load by up to 38.8 percent for the included angle of 120°. Meanwhile, the lowest elastic LTB load again overestimated the corresponding inelastic LTB load by up to 29.9 percent at $2\alpha = 180°$. The aforementioned percentage differences represented the impacts of the applied imperfections on the LTB loads. Also, it was noticed that the imperfections appeared to have their maximum impact at $2\alpha = 50°$, where the elastic LTB load overestimated the expected real LTB load by up to 47.5 percent. Overall, the elastic LTB loads overestimated the expected real LTB loads by close to 40 percent on average, indicating the influence of the applied imperfections on the LTB loads.

4.4.3.2.2 Assessments on the effects of imperfections on the lateral-torsional buckling loads of arches developed from profile 16825 at constant slender ratio 90

A typical comparison between the critical elastic buckling loads F_{cr} and ultimate buckling loads F_{ult} at included angles 2α for arches developed at $S/r_x = 90$ from profile 16825 is presented in figure 4.**27**.

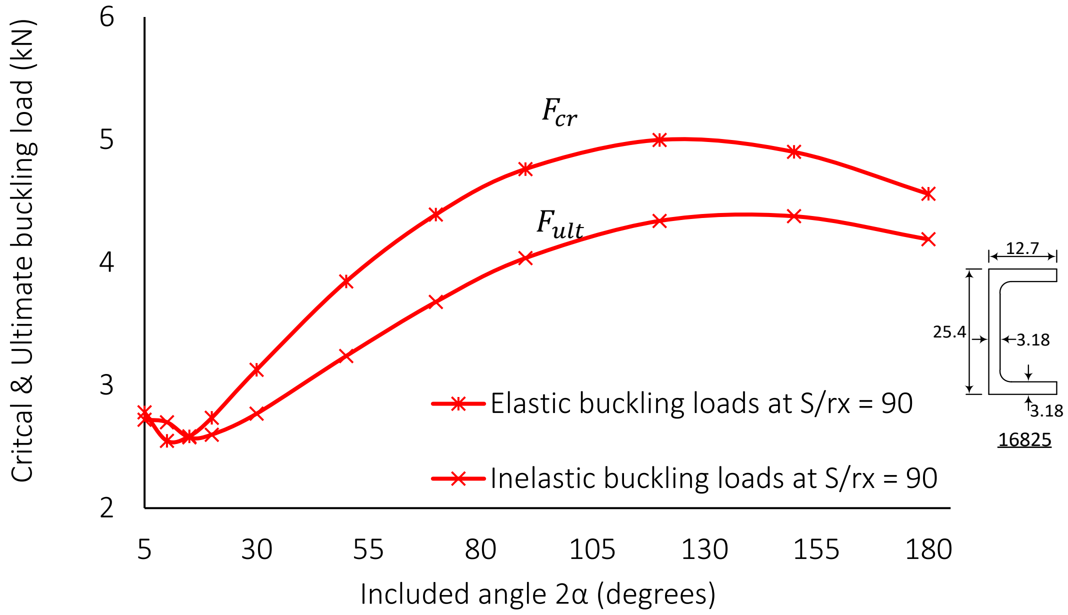

Figure 4.27 Comparison of the critical and ultimate lateral-torsional buckling loads for profile 16825 developed at slender ratio 90

It can be seen in figure 4.**27** that both the elastic and inelastic LTB loads first decreased to their minimum values and then increased to their maximum values before slightly decreasing again with the continued increase of included angles. At $2\alpha < 20°$, an insignificant difference was observed between the elastic and inelastic LTB loads. At that range, the inelastic LTB loads were noticed to be higher than their elastic counterparts. Nevertheless, at $2\alpha > 20°$, the elastic LTB loads were higher than their inelastic counterparts and significant differences were also noticed between the loads. These behaviours were associated with the combined axial compressive and bending actions on the LTB loads, as discussed in Sections 4.**4.1** and 4.**4.2**.

Regarding the LTB loads magnitudes, the overall low inelastic LTB loads at $2\alpha > 20°$ showed the impact of the applied imperfections on the LTB loads to be more significant. Hence, an ideal analysis would overestimate the expected real LTB loads at those included angles and vice versa. The percentage difference between the maximum and minimum elastic and inelastic LTB loads, respectively, are summarised in table 4.**16**. Again, the elastic LTB loads curve was used as the reference for measurement due to its overall high magnitude.

Table 4.16 The maximum and minimum elastic and inelastic LTB load differences in percentages for arches developed at constant slender ratio 90 from profile 16825

The percentage difference between the maximum elastic LTB load and the corresponding inelastic LTB load		The percentage difference between the minimum elastic LTB load and the corresponding inelastic LTB load		The maximum difference in percentage	
Included angle 2α in degree (°)	Percent (%)	Included angle 2α in degree (°)	Percent (%)	Included angle 2α in degree (°)	Percent (%)
120	14.1	10	-5.8	70	17.6

From table 4.**16**, it is noted that by the introduction of the imperfections, the maximum elastic LTB load overestimated the corresponding inelastic LTB load by just 14.1 percent. Meanwhile, the maximum impact of the imperfections on the LTB loads across the included angles was noticed to be up to 17.6 percent at included angle $2\alpha = 70°$. In addition, the elastic LTB load was realised to have underestimated the expected real LTB load by 5.8 percent only. The underestimation of the inelastic LTB load explained the negative difference in percentage shown in table 4.**16**. On average, the elastic LTB loads were found to have overestimated the inelastic LTB loads by just 9 percent. This percentage indicated that the effects of the imperfections on the LTB loads become less significant as the slender ratios increases.

4.4.4 General discussion on the elastic and inelastic effects on factors that influence LTB

The overall results reported in this section were obtained from the validated FEA methods. The results presented in this study revealed that the investigated factors influenced the prebuckling, which in turn impacted the LTB behaviour and loads. These include cross-sections (change of web-flange thickness and section depth), slender ratios and imperfections. Also, the effects of these factors were observed to vary with included angles for both arches developed at constant span length and slender ratios. That said, the general discussion of the effects these factors have on LTB loads of the two principal arches; that is, those developed constant span length and constant slender ratios, are then presented.

4.4.4.1 General discussion on the factors that impacted the lateral-torsional buckling loads of arches developed at constant span length

The combined elastic and inelastic axial compressive forces and bending moments were observed to have relative impacts on the LTB loads behaviour rather than the magnitudes since the respective overall axial compressive forces and the bending moments' magnitudes were not comparable to that of the LTB loads' magnitudes. As a result, the LTB loads magnitudes for the different channel profiles depended most on the torsion constant, of which profile 16831 had the most LTB load-carrying capacity due to its high torsion constant, followed by profiles 16825 and 16045, respectively, which indicated the influence of the change in web-flange thickness and section depth on the LTB loads.

For the elastic LTB loads, all the profiles were observed to attain their maximum LTB loads at $2\alpha = 70°$ and their minimum at $2\alpha = 180°$. These high and low LTB loads clearly indicated that the $70°$ included angle would be the most suitable in an ideal design against LTB, while the $180°$ would be the least favourable. Based on the nature of the curves shown in Section 4.4.1.1, the included angles closed to $70°$ and $180°$ should expect similar resistance to LTB. On the other hand, the inelastic minimum LTB loads were observed at similar included angles of $180°$ making the $180°$ least favourable for the designs against LTB for such arches. However, arches with section depth to width ratio of 2, the $90°$ included angle was found to be the most favourable in inelastic designs against LTB. Nonetheless, as the section depth to width ratio increased to 3, the shallow included angle of $15°$ offered the most resistance to LTB, which may imply, as the section depth to width ratio increases, the shallow arches become more suitable in the design against LTB for these arches.

For the individual profiles, significant differences were observed between the elastic and inelastic LTB loads, with the most magnitude noticed for elastic LTB loads. The inelastic analyses' low LTB loads resulted from the applied imperfections. These low magnitudes of the inelastic LTB loads indicated that for such arches, an ideal analysis would overestimate the expected LTB load-carrying capacity of the arch. That means, for arches with similar dimension ratios characteristics as those investigated in this study, the inelastic analysis would be more suitable in designs against LTB due to the strong negative influence of the applied imperfection on the LTB loads. However, at $2\alpha > 150°$, for profile 16045, as shown in figure 4.**23**, the effects of the imperfections turn to have a positive impact on the LTB loads. Also, for all the channel profiles, the maximum difference between the elastic and inelastic buckling loads at equivalent included angles occurred at $2\alpha = 50°$. This incident implied that one should expect a more significant drop in the LTB load between the elastic and inelastic LTB loads about that included angle.

In summary, the magnitudes of the axial compressive forces and central bending moments were observed to be unrelated to the LTB loads magnitude but related to the torsion constants. In addition, the imperfections were observed to have significant impacts on the LTB loads for all profiles. The differences between the elastic and inelastic buckling loads were more significant on moderation arches, followed by shallow arches and then deep arches. This alteration indicates that although the cross-sections significantly influence the LTB loads' magnitude, the imperfections, as well as the included angles, have significant impacts.

4.4.4.2 General discussion on the factors that impacted the lateral-torsional buckling loads of arches developed at constant slender ratios

For these arches, it was observed that the elastic and inelastic axial compressive force and bending moment actions were relative to the LTB loads behaviours as well as the magnitudes. Subsequently, their respective axial compressive forces and the bending moments' magnitudes were comparative to that of the LTB loads; that is, for arches with an overall high elastic axial compressive force and low elastic bending moments as the case for those developed at $S/r_x = 90$, a lower LTB load should be expected. However, for inelastic LTB loads, arches with the overall high inelastic axial compressive forces and bending moments would provide an overall high inelastic LTB load. These behaviours clearly indicate that for such arches, the slender ratio, which is causally related to the developed arch length, significantly influences both the elastic and inelastic LTB loads.

Furthermore, the maximum elastic LTB loads for arches developed at a constant slender ratio of 60 and 90 were attained at $120°$ included angle with a significant difference of over 80.5 percent, while their minimum LTB loads were attained at $10°$ included angle with a significant difference of approximately 92.3 percent. These occurrences showed by how much can an increase of the slender ratio by just 50 percent influence the LTB load-carrying capacity. Also, it reveals that for more stability against LTB for channel arches developed at constant slender ratios greater than 60, deep arches, in particular, the $120°$ included angle, would offer the most resistance against the LTB instability. Meanwhile, shallow arches, in specific, at $10°$ included angle would offer the least resistance against the LTB. Similarly, for the inelastic LTB loads, the maximum LTB loads were attained at $150°$ included angle with a 61.7 percent difference between both slender ratios, while the minimum LTB loads were attained for shallow arches with a 60 percent difference between arches developed at $S/r_x =$ 60 and 90 for the same included angle. Furthermore, the low inelastic LTB loads revealed that shallow arches at $2\alpha \leq 30$ would offer the least resistance against LTB.

In comparisons of the individual slender ratios' elastic and inelastic LTB loads, for both arches, the elastic LTB loads magnitudes were, in general, higher than those of the inelastic LTB loads. For arches developed at $S/r_x = 90$, the inelastic LTB loads were higher than their elastic counterparts at $2\alpha < 20°$, as shown in figure 4.**27**. Nevertheless, the overall low inelastic LTB loads indicated the negative influence of the applied imperfections on the LTB load-carrying capacity. However, it was realised that the imperfections impact on the LTB loads were more significant for arches developed at $S/r_x = 60$ with a maximum percentage difference of 47.5 at relative included angles. Meanwhile, only a 17.6 percent maximum percentage difference was noticed for arches developed at $S/r_x = 90$. This occurrence clearly indicated that as the slender ratios decreases, the impact of imperfections increases and vice versa.

In summary, the axial compressive forces and bending moments behaviours and magnitudes were relative to that of the LTB loads behaviours and magnitudes. An increase in the slender ratio had a significant impact on the LTB loads. Also, the imperfections (combined effects of the material nonlinearity, geometric imperfection and residual stresses) had significant impacts on the LTB loads and influenced the included angles at which the maximum LTB load occurs, by comparison of the inelastic LTB loads (with imperfections) and the elastic LTB loads (without imperfections) in Section 4.4.3. Additionally, the elastic analysis overestimated the real LTB loads, which, if not taken into consideration in actual designs, might be problematic. Also, for better LTB stability, the deeps arches ($2\alpha > 90°$) offered the most resistance, followed by the moderate arches ($30° < 2\alpha < 90°$) and shallow arches ($2\alpha \leq 30°$), respectively.

Chapter 5: Conclusions and Recommendations

The following conclusions and recommendations were drawn from this study:

5.1 Conclusions

i. The obtained finite element models elastic and elastic-plastic results compared to those of existing analytical solutions demonstrated good agreement. This entails the FE models were effective, efficient and accurate in terms of model nodes and elements used.

ii. The effects of the change in web-flange thickness, section depth and slender ratios are said to have a significant influence on the axial compressive forces and bending moment's magnitudes. However, very insignificant differences are observed in the behaviour change due to the individual parameters.

iii. For arches developed at constant span length, the further the shear centre from the centroid position the higher the elastic axial compressive force magnitudes. For arches developed at constant slender ratios, the higher the slender ratio, the higher the elastic axial compressive force, but the lower the inelastic axial compressive force.

iv. For Arches developed at constant span length having same section width, reducing the web-flange thickness by half lessens the maximum elastic and elastic-plastic axial compressive force by 23.4 and 44.4 percent at $2\alpha = 20°$ and $2\alpha = 30°$, respectively. Whereas, increasing the section depth by 50 percent would yield a maximum decrease of 38.9 and 8.8 percent at $2\alpha = 20°$ and $2\alpha = 30°$ for the elastic and elastic-plastic axial compressive forces, respectively.

v. Having the web-flange thickness reduce by half, increases the elastic bending moment by 6.8 percent at $2\alpha = 120°$ and increases the elastic-plastic counterpart by 17.5 percent at $2\alpha = 10°$. Meanwhile, decreasing the section depth by 50 percent, would result to an 8.2 percent maximum increase of the elastic bending at $2\alpha = 120°$ and maximum decrease of 10.8 percent of the elastic-plastic bending moment at $2\alpha = 10°$.

vi. For arches developed at the constant slender ratios, decreasing the slender ratio by 50 percent, decreases the elastic axial compressive forces by a maximum of 45.1 percent at $2\alpha = 15°$. Also, an increase of the slender ratio by

50 percent, would decrease the elastic-plastic axial compressive force by a maximum of 37.5 percent at $2\alpha = 30°$. Meanwhile increasing the slender ratio by 50 percent, would decrease the elastic and elastic-plastic bending moments by a maximum of 11.9 and 37.8 percent at $2\alpha = 50°$and 150°, respectively.

vii. In terms of behaviours, the elastic and elastic-plastic axial compressive forces behave in a similar manner for corresponding included angles. In addition, a close relationship exists between the axial compressive forces' behaviour and those of the LTB load. That is, as the axial compressive increase or decrease across included angles, similar behaviour is expected for the LTB loads.

viii. For most of the included angles, no relationship in behaviour can be expressed between the bending moments and corresponding LTB loads. However, for shallow arches, elastic-plastic bending moment and their corresponding LTB loads behaved alike, that is, due to the sensitivity of the applied imperfections on shallow arches.

ix. The axial compressive forces and bending moments magnitudes for arches developed at constant span length are found not to be relative to those of LTB loads magnitudes. On the other hand, those obtained from arches developed at constant slender ratios were relative to both the LTB load's magnitudes and behaviours.

x. From all arches investigated, the cross-section, slender ratios, imperfections and included angles were found to play important roles in the elastic and inelastic LTB loads.

xi. The torsion constants happen to have the most significant effects on the overall LTB loads magnitudes for arches developed at constant span length; that is, arches with high torsion constant, as found with profile 16831, have more resistance to LTB, compared to those of lower torsion constant. Thus, such high torsion constant profiles are more suitable for designs against LTB.

xii. At constant slender ratios, arches developed at $S/r_x = 60$ are found to have the most resistance to LTB; that is, the lower the slender ratio, the higher the LTB load and vice versa. Similar behaviour was also observed in arches that were developed at constant span length, as the slender ratios drop, the arch member was more resistive to LTB and vice versa.

xiii. For arches developed at constant span length in elastic analyses, the $70°$ included angle provided the most significant LTB loads for all three profiles; that is, highest resistance against LTB. Meanwhile, for the inelastic analyses, the $90°$ and $10°$ included angles were noted to offer the highest resistance against LTB for arches with section depth to width ratio of 2 and 3, respectively. For both elastic and inelastic analyses, the $180°$ included angle provided the minimum resistance against LTB. In summary, moderate arches provided the highest resistance against LTB, followed by the shallow and deep archers, respectively.

xiv. For arches developed at constant slender ratios in elastic analyses, the $120°$ included angle provided the most significant elastic LTB loads, while for inelastic analyses, it was noted at $150°$ included angles. On the other hand, the shallow arches at $2\alpha < 30°$ included angles, in general, offered the minimum LTB loads. Therefore, the deep arches were stable to LTB, followed by the moderate and shallow arches, respectively.

xv. All the investigated channel arches showed the imperfections to have significant impacts on the LTB loads. The imperfections impact on the LTB loads were different for all the arches.

xvi. For channel arches with section depth to width ratio of 2, profile 16825 and 16045 developed at the constant span length, the maximum elastic LTB load overestimated the expected real LTB load by 48.7 percent and 47.9 percent, respectively, which means, at such section depth to width ratio, the elastic analysis would not be suitable for designs of such arches.

xvii. The maximum elastic LTB load at $S/r_x = 60$ overestimated its inelastic counterpart by 38.8 percent, while the maximum elastic LTB load at $S/r_x = 90$ overestimated its inelastic counterpart by only 14.1 percent. This occurrence revealed that as the slender ratios decrease for such arches, the effect of imperfections decreases and vice versa.

5.2 Recommendations

i. The material nonlinearity, initial geometric imperfections and residual stresses were the main factors investigated in this study, of which all the different values used were based on the general recommendations made by other researchers.

However, while this study has provided valuable insight into the effect of imperfections on the LTB loads of such arches, it would be necessary for the imperfection's variables to be determined on similar real profiles and used to investigate their real impacts.

ii. Furthermore, although the results in this study have shown the elastic LTB loads to overestimate the real LTB loads by up to 55.5 percent, it was also revealed that the over-estimation decreases with an increase in slender ratio as the elastic LTB load becomes closer to the inelastic LTB load. Thus, the level by which the elastic analysis overestimates the expected real buckling load for arches with constant slender ratios below 60 or above 90, is not absolute.

iii. From the reviewed literature, the load position may also impact the real buckling load significantly. Thus, it would provide vital insight to understand the impact of imperfections in general by considering other loading positions, since channel sections are expected to experience eccentric loading in real life, due to the position of their shear centre.

References

Aerospace Specification Metals Inc (2015) 'Aluminum 6063-T6'. ASM material data sheet.

Ahnlen, M. and Westlund, J. (2013) *Lateral Torsional Buckling of I-beams: A Parametric Study of Elastic Critical Moments in Strucutral Design Software*. Chalmers University of Technology.

Bajer, M., Barnat, J. and Pijak, J. (2017) 'Lateral Torsional Buckling of Selected Cross-Section Types', *Procedia Engineering*. Elsevier B.V., 190, pp. 106–110. doi: 10.1016/j.proeng.2017.05.314.

Bernuzzi, C. and Cordova, B. (2016) *Structural Steel Design to Eurocode 3 and AISC Specifications*. John Wiley & Sons.

Bradford, M. A., Trahair, N. S. and Chen, Y. Y. (2005) 'A further study of flexural-torsional buckling of elastic arches', *International Journal of Structural Stability and Dynamics*, 5(2), pp. 163–183.

BSI (2007) 'BS EN 1999-1-1:2007 - Eurocode 9: Design of aluminium structures - Part 1-1: General Structural rules', *Eurocode 9*. European Committee for Standardization.

Chapra, S. C. and Canale, R. P. (2009) *Numerical methods for engineers*, *Mathematics and Computers in Simulation*. doi: 10.1016/0378-4754(91)90127-o.

Dahmani, L. and Drizi, S. (2015) 'Lateral torsional buckling of an eccentrically loaded channel section beam', *Strength of Materials*, 47(6), pp. 912–916. doi: 10.1007/s11223-015-9728-x.

Dokšanović, T., Džeba, I. and Markulak, D. (2017) 'Applications of aluminium alloys in civil engineering', *Tehnicki vjesnik - Technical Gazette*, 24(5). doi: 10.17559/tv-20151213105944.

Dou, C. *et al.* (2014) 'Effects of shape functions on flexural-torsional buckling of fixed circular arches', *Engineering Structures*. Elsevier Ltd, 59, pp. 238–247. doi: 10.1016/j.engstruct.2013.10.028.

Dou, C. *et al.* (2015) ‘Experimental Investigation into Flexural-Torsional Ultimate Resistance of Steel Circular Arches’, *Journal of Structural Engineering*, 141(10), p. 04015006. doi: 10.1061/(asce)st.1943-541x.0001240.

Efthymiou, E., Cöcen, O. N. and Ermolli, S. R. (2010) ‘Sustainable aluminium systems’, *Sustainability*, 2(9), pp. 3100–3109. doi: 10.3390/su2093100.

Ellobody Ehab, Feng Ran and Young Ben (2014) *Finite Element Analysis and Design of Metal Structures*.

EN (2007) *Eurocode 9, design of aluminium structures—Part 1-1: General structural rules*, *Eurocode 9*. European Committee for Standardization.

EN BS (2011) ‘BS EN 1993-2:2006 - Eurocode 3: Design of steel structures - Part 2: Steel bridges’, in *Eurocode 3*, p. 105.

Galambos, T. V. and Surovek, A. E. (2008) ‘Structural Stability of Steel: concepts and applications for structural engineers’, in *Structural Stability of Steel*, pp. 236–289. doi: 10.1002/9780470261316.

Gambhir, M. L. (2013) ‘Stability analysis and design of structures’, in *Stability analysis and design of structures*. Springer Science & Business Media. doi: 10.1201/9780203484418.

Guo, Y. *et al.* (2015) ‘An experimental study on out-of-plane inelastic buckling strength of fixed steel arches’, *Engineering Structures*. Elsevier Ltd, 98(9), pp. 118–127. doi: 10.1016/j.engstruct.2015.04.029.

Höglund, T. (2010) ‘TALAT Lecture 2301: Design of Members’, in, pp. 1–125.

Hu, N. *et al.* (1999) ‘Two kinds of c0-type elements for buckling analysis of thin-walled curved beams’, *Computer Methods in Applied Mechanics and Engineering*. Elsevier Science S.A., 171(1–2), pp. 87–108. doi: 10.1016/S0045-7825(98)00246-1.

Hulamin Extrusions (2015) ‘Standard Profile Catalogue’.

Hulamin Extrusions (2016) *Hulamin Extrusions: Design Manual*.

J.R. Davis (2001) *Alloying Understand The Basic*. doi: 10.1016/S1877-

1823(09)70027-X.

Kang, K. and Bert, C. W. (1997) 'Flexural-torsional buckling analysis of arches with warping using DQM', *Engineering Structures*, 19(3), pp. 247–254. doi: 10.1016/S0141-0296(96)00057-0.

Kang, Y. J. and Yoo, C. H. (1994) 'Thin-walled curved beams. II: analytical solutions for buckling of arches', *Journal of engineering mechanics*, 120(10), pp. 2102–2125.

Kim, M.-Y., Min, B.-C. and Suh, M.-W. (2000a) 'Spatial stability of nonsymmetric thin-walled curved beams. I: Analytical approach', *Journal of engineering mechanics*, 126(5), pp. 497–505.

Kim, M.-Y., Min, B.-C. and Suh, M.-W. (2000b) 'Spatial stability of nonsymmetric thin-walled curved beams. II: Numerical approach', *Journal of engineering mechanics*, 126(5), pp. 506–514.

King, C. and Brown, D. (2001) *Design of Curved Steel*, *The Steel Construction Institute*.

Lam, D., Ang, T.-C. and Chiew, S.-P. (2013) *Structural Steelwork Design to Limit State Theory*. Fouth Edit. CRC Press.

Lim, N. H. and Kang, Y. J. (2004) 'Out of plane stability of circular arches', *International Journal of Mechanical Sciences*, 46(8), pp. 1115–1137. doi: 10.1016/j.ijmecsci.2004.08.008.

Liu, A., Lu, H., Fu, J. and Pi, Y.-L. (2017) 'Lateral-Torsional Buckling of Circular Steel Arches under Arbitrary Radial Concentrated Load', *Journal of Structural Engineering*, 143(9), p. 04017129. doi: 10.1061/(asce)st.1943-541x.0001858.

Liu, A., Lu, H., Fu, J. and Pi, Y. L. (2017) 'Lateral-torsional buckling of fixed circular arches having a thin-walled section under a central concentrated load', *Thin-Walled Structures*. Elsevier Ltd, 118(May), pp. 46–55. doi: 10.1016/j.tws.2017.05.002.

De Louw, C. H. M. (2007) 'Design rule for lateral torsional buckling of channel sections', p. 209.

Lu, H., Liu, A., Bradford, M. A., *et al.* (2019) 'Experimental investigation of out-of-plane buckling of circular arches under a central radial point load', *Thin-Walled Structures*. Elsevier Ltd, (May), p. 106198. doi: 10.1016/j.tws.2019.106198.

Lu, H., Liu, A., Pi, Y. L., *et al.* (2019) 'Lateral-torsional buckling of arches under an arbitrary radial point load in a thermal environment incorporating shear deformations', *Engineering Structures*. Elsevier, 179(October 2018), pp. 189–203. doi: 10.1016/j.engstruct.2018.10.071.

Marwala, T. (2010) *Finite element model updating using computational intelligence techniques: applications to structural dynamics*. Johannesburg: Springer Science & Business Media.

Mary Brettle (2006) 'Lateral torsional buckling and slenderness', *Ncs*, 14(9), pp. 30–34. doi: 10.1109/CDC.2011.6160604.

Mazzolani, F. M. (2004) *Design of Aluminium Structures*. Naples.

Metals, A. A. S. (2012) 'Aluminum 6061-T6 ; 6061-T651', *ASM material data sheet*. Florida, USA, pp. 7–8.

Mudenda, K. and Zingoni, A. (2018) 'Lateral-torsional buckling behavior of hot-rolled steel beams with fl ange upstands (c) Doubly symmetric cross-section and corresponding monosymmetric section', *Journal of Constructional Steel Research*, 144, pp. 53–64.

Nziu, P. K. and Masu, L. M. (2019) 'Cross bore geometry configuration effects on stress concentration in high-pressure vessels: a review', *International Journal of Mechanical and Materials Engineering*. International Journal of Mechanical and Materials Engineering. doi: 10.1186/s40712-019-0101-x.

Ozbasaran, H., Aydin, R. and Dogan, M. (2015) 'An alternative design procedure for lateral-torsional buckling of cantilever I-beams', *Thin-Walled Structures*. Elsevier, 90, pp. 235–242. doi: 10.1016/j.tws.2015.01.021.

Papangelis, John. P and Trahair, N. S. (1986) 'Finite Element Analysis of Arch Lateral Buckling', *Trans Inst Eng Aust Civ Eng*, CE29(1), pp. 34–39.

Papangelis, John P and Trahair, N. S. (1986) ‘Flexural-torsional buckling of arches’, *Journal of Structural Engineering*, 113(4), pp. 889–906. doi: 10.1061/(ASCE)0733-9445(1986)112:11(2494).

Papangelis, J. P. and Trahair, N. S. (1987) ‘Flexueal-Torsional Buckling Tests on Arches’, *Journal of Structural Engineering*, 113(7), pp. 1433–1443. doi: 10.1061/(ASCE)0733-9445(1987)113.

Papangelis, J. P. and Trahair, N. S. (1988) ‘Buckling of monosymmetric arches under point loads’, *Engineering Structures*, 10(4), pp. 257–264. doi: 10.1016/0141-0296(88)90047-8.

Pi, Y.-L., Bradford, M. A. and Liu, A. (2017) ‘High strength steel I-section arches: Inelastic lateral buckling and moment capacity’, *Ce/Papers*, 1(2–3), pp. 3472–3480. doi: 10.1002/cepa.402.

Pi, Y.-L. and Trahair, N. S. (1998) ‘Out-of-Plane Inelastic Buckling and Strength of Steel Arches’, *Journal of Structural Engineering*, 124(2), pp. 174–173. doi: 10.1061/(asce)0733-9445(1999)125:3(352).

Pi, Y. L. and Bradford, M. A. (2003) ‘Elasto-plastic buckling and postbuckling of arches subjected to a central load’, *Computers and Structures*, 81(18–19), pp. 1811–1825. doi: 10.1016/S0045-7949(03)00204-9.

Pi, Y. L. and Bradford, M. A. (2004a) ‘Effects of prebuckling deformations on the elastic flexural-torsional buckling of laterally fixed arches’, *International Journal of Mechanical Sciences*, 46(2), pp. 321–342. doi: 10.1016/j.ijmecsci.2004.02.012.

Pi, Y. L. and Bradford, M. A. (2004b) ‘Elastic flexural-torsional buckling of fixed arches’, *Quarterly Journal of Mechanics and Applied Mathematics*, 57(4), pp. 551–569. doi: 10.1093/qjmam/57.4.551.

Pi, Y. L. and Bradford, M. A. (2004c) ‘In-plane strength and design of fixed steel I-section arches’, *Engineering Structures*, 26(3), pp. 291–301. doi: 10.1016/j.engstruct.2003.09.011.

Pi, Y. L. and Bradford, M. A. (2005) ‘Out-of-plane Strength Design of Fixed Steel I-

Section Arches', *Engineering Structures*, 131(4), pp. 560–568. doi: 10.1016/j.engstruct.2003.09.011.

Pi, Y. L. and Bradford, M. A. (2010) 'Effects of prebuckling analyses on determining buckling loads of pin-ended circular arches', *Mechanics Research Communications*, 37(6), pp. 545–553. doi: 10.1016/j.mechrescom.2010.07.016.

Pi, Y. L. and Bradford, M. A. (2012) 'Non-linear in-plane analysis and buckling of pinned-fixed shallow arches subjected to a central concentrated load', *International Journal of Non-Linear Mechanics*. Elsevier, 47(4), pp. 118–131. doi: 10.1016/j.ijnonlinmec.2012.04.006.

Pi, Y. L. and Bradford, M. A. (2013a) 'Lateral-torsional buckling analysis of arches having in-plane rotational end restraints under uniform radial loading', *Journal of Engineering Mechanics*, 139(11), pp. 1602–1609. doi: 10.1061/(ASCE)EM.1943-7889.0000599.

Pi, Y. L. and Bradford, M. A. (2013b) 'Lateral-torsional elastic buckling of rotationally restrained arches with a thin-walled section under a central concentrated load', *Thin-Walled Structures*. Elsevier, 73, pp. 18–26. doi: 10.1016/j.tws.2013.07.006.

Pi, Y. L., Bradford, M. A. and Tong, G. S. (2010) 'Elastic lateral-torsional buckling of circular arches subjected to a central concentrated load', *International Journal of Mechanical Sciences*. Elsevier, 52(6), pp. 847–862. doi: 10.1016/j.ijmecsci.2010.02.003.

Pi, Y. L. and Trahair, N. S. (1996) 'Three-dimensional nonlinear analysis of elastic arches', *Engineering Structures*, 18(1), pp. 49–63. doi: 10.1016/0141-0296(95)00039-3.

Pi, Y. L. and Trahair, N. S. (2000) 'Inelastic lateral buckling strength and design of steel arches', *Engineering Structures*, 22(8), pp. 993–1005. doi: 10.1016/S0141-0296(99)00032-2.

Piloto, P., Real, P. V. and Franssen, J. (2000) 'A Simple Model for Lateral Torsional Buckling Resistance of Steel I-Beams Under Fire Conditions – Comparison with Experimental Results', in *In Proceedings do Symposium in Experimental Mechanics* *in design in Conjunction with the 3rd international conference in Mechanics and Materials in Design.*

Poinern, G. E. J., Ali, N. and Fawcett, D. (2010) *Progress in Nano-Engineered Anodic Aluminum Oxide Membrane Development*, *Materials*. doi: 10.3390/ma4030487.

La Poutré, D. B. (2005) *Inelastic spatial stability of circular wide flange steel arches*. doi: 10.6100/IR585818.

La Poutré, D. B. *et al.* (2013) 'Out-of-plane stability of roller bent steel arches - An experimental investigation', *Journal of Constructional Steel Research*. Elsevier Ltd, 81(5), pp. 20–34. doi: 10.1016/j.jcsr.2012.11.004.

Rajasekaran, S. and Padmanabhan, S. (1989) 'Equations of curved beams', *Journal of Engineering Mechanics*, 115(5), pp. 1094–1111. doi: 10.1061/(ASCE)0733-9399(1991)117:3(717.2).

Sadowski, A. J., Fajuyitan, O. K. and Wang, J. (2017) 'A computational strategy to establish algebraic parameters for the Reference Resistance Design of metal shell structures', *Advances in Engineering Software*. Elsevier Ltd, 109, pp. 15–30. doi: 10.1016/j.advengsoft.2017.02.012.

Segui, W. T. (2012) *Steel Design*. 4th edn. Cengage Learning.

Snijder, H. H. *et al.* (2008) 'Design rules for lateral torsional buckling of channel sections subject to web loading', *Stahlbau*, 77(4), pp. 247–256. doi: 10.1002/stab.200810036.

Spoorenberg, R. C. (2011) *Structural properties and out-of-plane stability of roller bent steel arches*. doi: 10.6100/IR716581.

Spoorenberg, R. C. *et al.* (2012) 'Design rules for out-of-plane stability of roller bent steel arches with FEM', *Journal of Constructional Steel Research*, 79, pp. 9–21. doi: 10.1016/j.jcsr.2012.07.027.

Steel Construction.org (2010) *SIGNS SN42*.

Trahair, Nicholas S., and J. P. P. (1987) 'Flexural-torsional buckling of monosymmetric arches', *Journal of Structural Engineering*, 113(10), pp. 2271–2288.

Trahair, N. S. (1993) *Flexural-Torsional Buckling of Structures New Directions in Civil Engineering*.

Valeš, J. and Stan, T. (2017) 'FEM Modelling of Lateral-Torsional Buckling using Shell and Solid Elements'. Elsevier B.V., 190, pp. 464–471. doi: 10.1016/j.proeng.2017.05.365.

Vlasov, V. Z. (1961) *Thin-walled Elastic Beams*. Jerusalem: National Technical Information Service.

Wang, Y. Q. *et al.* (2012) 'Lateral-torsional buckling resistance of aluminium I-beams', *Thin-Walled Structures*. Elsevier, 50(1), pp. 24–36. doi: 10.1016/j.tws.2011.07.005.

Wesley, D. (2017) *Lateral-torsional Buckling of Steel Channel Beams A parametric study through FE-analysis*.

Yang, Y.-B. and Kuo, S.-R. (1986) 'Static stability of curved thin-walled beams', *Journal of engineering mechanics*, 112(8), pp. 821–841.

Yang, Y. H., Chen, C. X. and Fang, M. J. (2011) 'Lateral-Torsional Buckling Strength and Design of Steel Arches', *Advanced Materials Research*, 250–253(5), pp. 2645–2649. doi: 10.4028/www.scientific.net/amr.250-253.2645.

Yang, Y. and Kuo, S. (1987) 'Effect of Curvature on Stability of Curved Beams', *Journal of Structural Engineering*, 113(6), pp. 1185–1202. doi: 10.1061/(ASCE)0733-9445(1987)113:6(1185).

Yang, Y., Kuo, S. and Cherng, Y. (1989) 'Curved Beam Elements for Nonlinear Analysis', *Journal of Engineering Mechanics*, 115(4), pp. 840–855. doi: 10.1061/(ASCE)0733-9399(1989)115:4(840).

Yoo, C. H. and Pfeiffer, P. A. (1983) 'Elastic Stability of Curved Members', *Journal of Structural Engineering*, 109(12), pp. 2922–2940. doi: 10.1061/(ASCE)0733-9445(1983)109:12(2922).

Ziemian, R. D. (2010) *Guide To Stability Design Criteria for Metal*. Sixth, *Sixth Edition*.

Sixth. Edited by Ronald D. Ziemian. Hoboken, New Jersey: John Wiley & Sons, Inc.

Appendix A

The channel profile cross-sectional area A is given by

$$A = B \times D - d(B - t_w) \tag{A.1}$$

whereby

$$d = D - 2t_f \tag{A.2}$$

The I-section profile cross-sectional area A is given by

$$A = (D \times B) - 2\left(\left(D - 2t_f\right) \times \left(\frac{B}{2} - \frac{t_w}{2}\right)\right) \tag{A.3}$$

Moment of inertia about the major axis I_x of the channel profile

$$I_x = \frac{B \times D^3 - d^3 \times (B - t_w)}{12} \tag{A.4}$$

Moment of inertia about the major axis I_x of the I-section profile

$$I_x = \left(\frac{t_w \times d^3}{12}\right) + \left(\frac{B}{12}\right) \times (D^3 - d^3) \tag{A.5}$$

Radius of gyration r_x

$$r_x = \sqrt{\frac{I_x}{A}} \tag{A.6}$$

For arches developed at constant slender ratio S/r_x, the span length L is given as

$$L = 2R \times sin\,\Theta \tag{A.7}$$

whereby R is the radius, Θ is half the included angle and are given as follows

$$R = \frac{S}{2\pi} \times \left(\frac{360°}{2\alpha}\right) \tag{A.8}$$

and

$$\Theta = \frac{\alpha}{2} \tag{A.9}$$

For arches developed at constant span length, the radius R and arc length S are given as

$$R = \frac{L}{2 \times sin\,\Theta} \quad \text{(A.10)}$$

$$S = 2\pi \times R\left(\frac{2\alpha}{360°}\right) \quad \text{(A.11)}$$

Prebuckling analyses

From Liu *et al.* (2017b), the following equations were proposed for prebuckling analysis for fixed arches.

Dimensionless axial compressive force, $= \frac{N_N}{F}$ (A.12)

where the axially compressive force N_N is given as

$$N_N = F \times E_1 \times cos\,\theta + \frac{1}{2} \times F \times H(\theta) \times \sin\theta \quad \text{(A.13)}$$

The coefficient E_1 and step function $H_m(\theta)$ are given as

$$H(\theta) = \begin{cases} -1 & \theta \leq 0 \\ 1 & \theta > 0 \end{cases}, \quad \text{(A.14)}$$

and

$$E_1 = -\frac{\Xi}{2\omega} \quad \text{(A.15)}$$

where the constant Ξ and ω are given by

$$\Xi = (R + r_x^2) \times \Theta \times sin^2\theta + 2R^2 \times sin(\Theta) \times (cos\,\theta - 1), \quad \text{(A.16)}$$

and

$$\omega = (R^2 + r_x^2) \times \Theta(\Theta + cos\,\theta \times sin\,\theta) - 2R^2 \times sin^2\theta \quad \text{(A.17)}$$

Dimensionless bending moment, $= \frac{4M_M}{FL}$ (A.18)

The bending moment M_M is given by

$$M_M = F \times E_2 \times R - N_N \times R \quad \text{(A.19)}$$

where coefficient E_2 is given by

$$E_2 = -\frac{B_1}{2\omega} \tag{A.20}$$

and the constant

$$B_1 = (R^2 + r_x^2) \times (cos\,\theta - 1) \times (\sin\theta - 1), \tag{A.21}$$

From Pi and Bradford, (2003) the following equation was proposed for the end moment M_d for fixed arches.

$$M_d = \frac{F \times R \times (1 - \cos\theta)}{2\theta} + H \times y_1 - \frac{F \times R \times \sin\theta}{2} \tag{A.22}$$

where the horizontal reaction H is given by

$$H = A_2 \times K_2 \times F \tag{A.23}$$

and

$$y_1 = R \times \left(\frac{\sin\theta}{\theta} - \cos\theta\right) \tag{A.24}$$

The coefficient A_2 and K_2 are given by

$$A_2 = \frac{\sin\theta \times (1 - \cos\theta) - \left({}^{\theta}/_{2}\right) \times (sin^2\theta)}{\theta \times (\theta + \sin\theta \times \cos\theta) - 2sin^2\theta}, \tag{A.25}$$

and

$$K_2 = \frac{1}{1 + \frac{n_2}{\lambda_x^2}} \tag{A.26}$$

where the constant n_2 is given by

$$n_2 = \frac{Z^4}{\gamma^2} \times \left(1 + \frac{2Z^2}{\varepsilon_2}\right) \times \frac{\theta^2}{(1 - \cos\theta)^2} \tag{A.27}$$

with

$$\varepsilon_2 = \theta \times (\theta \times \gamma^2 + Y \times Z) - 2Z^2, \text{ with } Z = 4\rho,\ \ Y = 1 - 4\rho^2,\ \ = 1 - 4\rho^2\gamma \tag{A.28}$$

the constant ρ, is given by

$$\rho = \frac{f}{L} = \frac{1 - \cos\theta}{2\sin\theta} \tag{A.29}$$

where f = rise of the arch, and the slenderness of the arch λ_x is given by

$$\lambda_x = \frac{S}{r_x} \tag{A.30}$$

For inelastic analysis

The plastic section modulus Z_M for an I-section is given by

$$Z_M = \left(B \times t_f \times \left(D - t_f\right) + \frac{1}{4} \times t_w \times (D - 2t_f)^2\right) \tag{A.31}$$

The plastic moment of a cross-section M_P is given by

$$M_P = \left(\alpha_y - \alpha_R\right) \times Z_M \tag{A.32}$$

The squash/crash load N_Y of the cross-section is given by

$$N_Y = \left(\alpha_y - \alpha_R\right) \times A \tag{A.33}$$

where α_y and α_R are the yield stress and residual stress respectively of the cross-section.

Note: The prebuckling solutions were used for both the elastic and elastic-plastic analyses with the only difference being in the applied load.

Appendix B

Elastic finite elements analysis results

Included angle (degree)	Dimensionless axial compressive force at the crown (N_C/F)	The dimensionless bending moment at the crown ($4M_C/FL$)	Bending moment at support M_d in (N.mm)
5	1.567	0.477	-56.818
10	2.567	0.425	-43.836
15	2.959	0.371	-30.167
20	2.979	0.327	-19.013
30	2.625	0.271	-4.739
50	1.869	0.229	7.221
70	1.39	0.219	11.938
90	1.082	0.221	14.702
120	0.787	0.236	18.056
150	0.594	0.263	21.803
180	0.455	0.305	26.864

Elastic calculated results based on Liu *et al.* (2017b), Pi and Bradford (2003) solutions

Included angle (degree)	Dimensionless axial compressive force at the crown (N_C/F)	The dimensionless bending moment at the crown ($4M_C/FL$)	Bending moment at support (M_d) in (N.mm)
5	1.549	0.478	-56.858
10	2.535	0.427	-43.898
15	2.937	0.372	-30.123
20	2.969	0.328	-18.787
30	2.629	0.272	-4.161
50	1.88	0.229	8.158
70	1.399	0.218	12.968
90	1.089	0.22	15.719
120	0.792	0.235	18.964
150	0.597	0.262	22.553
180	0.457	0.305	27.442

Inelastic finite elements analysis results

Included angle (degree)	Bending moment at support M_D in (N.mm)	The dimensionless axial compressive force at the crown (N_m/N_Y)	The dimensionless bending moment at the crown (M_m/M_P)
30	-1723.00	0.09145823	0.224
50	2452.00	0.060493118	0.175
70	4212.00	0.046487861	0.173
90	5161.00	0.036096827	0.174
120	5959.00	0.024713248	0.175

Inelastic calculated results based on Pi and Bradford (2003) proposed solution

Included angle (degree)	Bending moment at support M_D in (N.mm)	Dimensionless axial compressive force at the crown (N_m/N_Y)	The Dimensionless bending moment at the crown (M_m/M_P)
30	-1494.00	0.090229	0.21862
50	2749.00	0.060552	0.17261
70	4523.00	0.046634	0.17075
90	5473.00	0.036258	0.17183
120	6221.00	0.024831	0.17274